DEVELOPMENT AND APPLICATION OF COMPOSITE MATERIAL LAMINATION THEORY FOR PRINTED CIRCUIT BOARDS

by

Kun-Yen Wang

A thesis submitted to the Graduate Faculty of
Auburn University
in partial fulfillment of the
requirements for the Degree of
Master of Science

Auburn, Alabama
August 4, 2012

Approved by

Jeffrey C. Suhling, Chair, Quina Distinguished Professor of Mechanical Engineering
Polapragada K. Raju, Thomas Walter Professor of Mechanical Engineering
Winfred A. Foster, Professor of Aerospace Engineering

Abstract

Layers incorporating carbon fiber materials have been proposed to enhance the reliability of high performance printed circuit board production configurations. The carbon fiber layers feature high stiffness and high thermal conductivity, as well as near zero thermal expansion coefficients. In this research, theoretical approaches based on lamination theory have been developed for estimating the global/bulk coefficients of thermal expansion and mechanical properties of printed circuit boards incorporating carbon fiber layers based on the layer properties and stack-up configuration. Different types of carbon fiber laminates have been studied and tested. The coefficients of thermal expansion of individual carbon fiber PCB layers (plies) have been measured using strain gages with a temperature controlled chamber. The elastic moduli, Poisson's Ratios, and shear modulus of individual carbon fiber plies have also been evaluated. An indirect method was developed and applied to find the shear modulus and Poisson's ratio. The approach was applied to some example PCB configurations, and compared to the results of finite element analyses.

Table of Contents

List of Figures

List of Tables

I. INTRODUCTION

Literature Review

For modern electronics, such as smart phones or other consumer electronics, improvement goals include much smaller scale, increased power, tougher durability, and more cost effective. IBM corporation invented the C4 (Controlled Collapse Chip Connection) IC attachment method [1]. This breakthrough in electronic packaging technology is also known as the flip-chip packaging. Moreover, flip-chip assembly was taken up by Delco Electronics in the 1970s, and is commonly used in automobile applications. Undoubtedly, flip chip assembly results in smaller products than traditional chip carrier-based systems. Since the chip has been directly mounted on the PCB (Printed Circuit Board) substrate, the area and height used are much smaller. In addition, the close distance between the flip chip and the substrate provides multiple benefits including lower inductance, capability of transferring higher-speed signals, and good heat conduction. However, due to the short distance, the connections are extremely stiff and coefficient of thermal expansion mismatch becomes a major concern.

Figure 1 shows typical flip chip assemblies. Historically, ceramic substrates have ideal for flip chip attachment, since most ceramics have a similar CTE (Coefficient of Thermal Expansion) to the silicon chip. Large CTE mis-matches between the silicon chip and its substrate will cause cyclic stresses to be developed in the solder balls when the assembly is subjected to thermal cycling, and solder joint fatigue becomes the major failure mode. Use of ceramic substrates can eliminate this concern. However, due to the much higher production costs and

increased weight, ceramic packages are mostly limited to military and high performance applications.

FR-4 (Flame Resistant) glass-reinforced epoxy laminate materials have been commonly used for PCBs (Printed Circuit Boards) in nearly all fields of electronic devices. FR-4 is a composite material composed of woven fiberglass with an epoxy resin binder that is flame resistant. FR-4 materials have several benefits when serving as an electronic substrate such as low cost, low density, good strength to weight ratios, insensitive to humidity changes, and good electrical insulation and manufacturing characteristics. All of the above characteristics result in wide usage of FR-4 in many applications.

Due to the high CTE (16~20 ppm/^{o}C) offered by conventional FR-4 glass fiber materials, a large CTE mis-match occurs between the silicon (2.6 ppm/^{o}C) chip and the FR-4 substrate in flip chip on laminate applications [2]. This CTE mis-match leads to development of large stresses in the solder balls located between the flip chip and PCB. As a result, this can cause poor durability and short life-cycle of the device [3-5].

A general formulation referred to as classical lamination theory exists for mechanical analysis of composite materials. It can be used to calculate the deformations, strains, and stresses in a fiber-reinforced laminate such as a PCB that is subjected to mechanical loads and temperature changes. In addition, it can be used for predicting the average mechanical properties and CTEs of the laminate structure. The input properties to the theory include the mechanical properties and CTEs of each layer, as well as details of the stacking configuration including the order, orientations, and thicknesses of the various layers.

(a) Ceramic Substrate

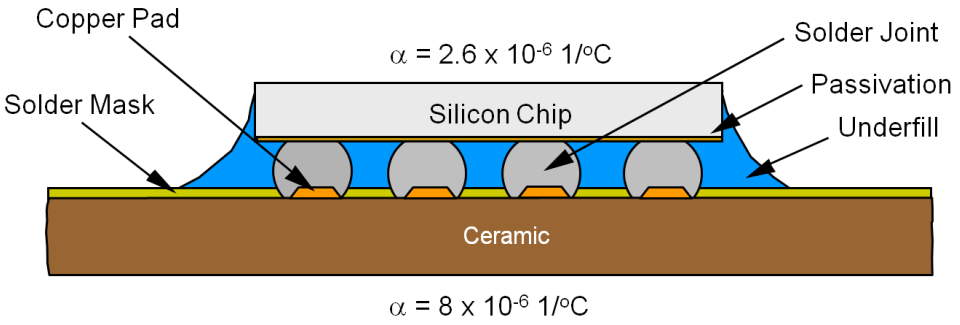

(b) FR-4 Substrate

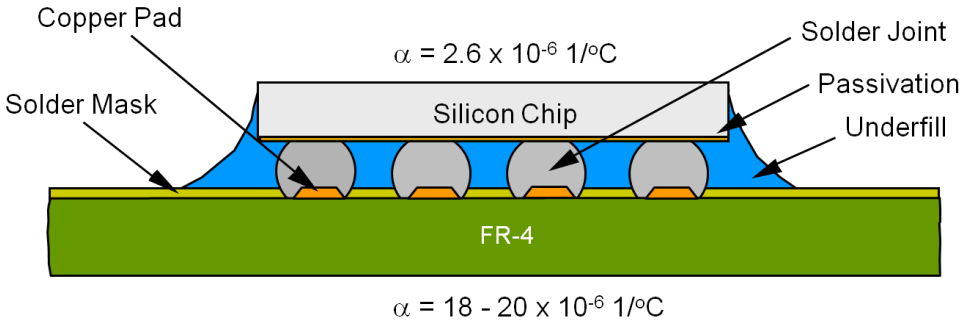

(c) STABLCOR Substrate

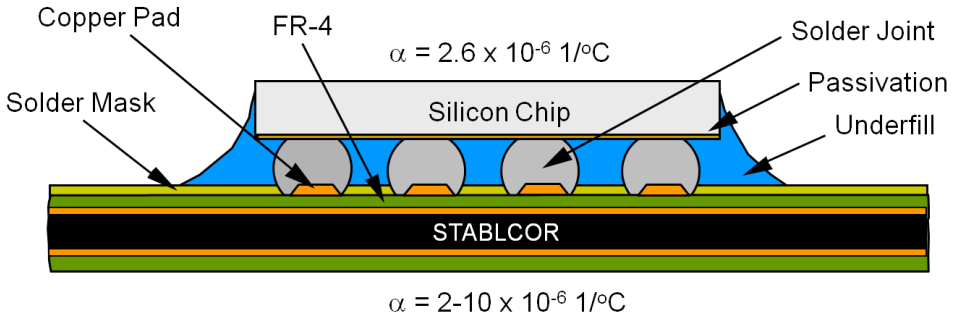

Figure 1. Typical Flip-chip Assemblies

Lamination theory was originally proposed for fiber-reinforced composite materials, and was based on a linear elastic orthotropic constitutive model and the typical assumptions of classical small deflection plate theory [6-7].

Lamination theory has often been applied to PCBs. For instance, Nakagawa and Yokoyama [8] used composite lamination theory in order to estimate deformation of the PCB during the reflow process. They also used the theory to optimize the stack up of the laminate to reduce PCB deformation. Tan and Ume [9] also used lamination theory to study PCB warpage during soldering processes and under normal operations.

In current high power electronic circuit design [10], it is common to have single or multiple thermal conductivity layers in PCB substrates. The ideal thermally conductive layers are metal plates or carbon-material plates. Metal materials such as copper-invar-copper, aluminum, and steel have been used as cores in PCBs to enhance thermal performance [11]. However, the main issue with these materials is undesirable weight. Jensen [12], patented a support board fabricated from graphite filament or aramid filament reinforced thermoset resin, which has a thermal coefficient of expansion less than 2 micro inch/inch/^{o}F. Leibowitz [13] showed that a multilayer combination between graphite and dielectric material, such as a polytetrafluoroethylene (PTFE) and woven glass laminate can provide both low dielectric constant and good mechanical strength with low or negative coefficient of thermal expansion. Moreover, he also claimed one of the principal advantages of the use of carbon fiber reinforced layers in the PCB structure is that they serve as a good conductors of heat, which normally flows from the mounted components through the copper layers of the board, through mounting bolts, and then to a housing or other heat sink.

Vasoya [14] also stated that PCB laminates made of continuous carbon fiber layers have the advantages on both high thermal conductivity and low in-plane CTE. STABLCOR® [15] (previously Thermount) is a trademarked carbon fiber based material set. Characteristic of STABLCOR materials include high thermal conductivity, low CTEs, and high elastic moduli. They are also of relatively low density compared to metals such as copper.

STABLCOR® [16-17] laminates have been used by various companies in the electronics industry such as Boeing, Ambient Energy, Infineon, Delphi, JPL, FLIR System, Los Alamos, Curtiss Wright, BAE System, Aehr Test System, Maxwell Technologies, Samsung, General Dynamics, and Raytheon. They are commonly used to replace certain layers in conventional PCBs such as copper-invar-copper, heavy copper, aluminum heat spreaders, thermal interface materials, and Thermount® materials [18]. STABLCOR® laminates also have additional benefits such as reduced moisture absorption, increasing rigidity without increasing weight, substantially increasing thermal conductivity, lowered assembly temperatures, and smaller z-axis expansion.

By considering all the advantages and benefits of STABLCOR®, carbon fiber based PCB ply materials have the potential to offer significantly lower CTE values as well as other improvements. In order to tailor the PCB into a desired CTE value and other related attributes, the choice of layer material properties and the laminate configuration are critical. For analysis purposes, composite lamination theory provides a strong theoretical background. Moreover, it will be shown in this thesis that lamination theory can be used to design and calculate performance for various laminate configurations with different types of STABLCOR® ply materials and provide predictions of the in-plane CTEs of the resulting PCB laminate.

II. LAMINATION THEORY FOR ORTHOTROPIC FIBER-REINFORCED COMPOSITES

Introduction

The fiber-reinforced composite materials considered in this work for PCB applications consist of glass and/or carbon fiber fabrics hardened with an epoxy resin. Macroscopically, a fiber-reinforced epoxy layer is an orthotropic material, where the elastic moduli are directionally dependent and are greatly affected by the angle to the fiber direction. The angle between the force and fiber direction determines the stiffness of the laminate. The fibers in such layers are long and continuous as opposed to whiskers. Several fiber-reinforced epoxy layers are typically stacked and bonded to form a composite material laminate. The mechanical response of a laminate can be modeled using the general purpose lamination theory presented in this chapter. The layers in the composite laminate are usually designed to be symmetrical in relation to the thickness of the board. This is especially true for laminates with carbon fiber layers since they have very low CTE and very high tensile modulus, and thus dominate the other glass reinforced layers [14].

All of the fiber-reinforced laminates used in this research were constructed from bi-directional $0^o/90^o$ woven layers. In this case, the principal material directions are 0^o (x_1-direction) and 90^o (x_2-direction) and layer is classified as an orthotropic material. For orthotropic materials, like isotropic materials, application of normal stresses in a principal direction results in extension in the direction of the stress and contraction perpendicular to the stress. The strain in one principal material direction could be different from the strain in another principal material direction, even under the same normal stress. In other words,

different elastic moduli exist for the various principal material directions in the orthotropic material. Moreover, due to the different stiffness properties in the two principal material directions, the contractions will also be different for the two principal directions. Thus, the Poisson's Ratios of an orthotropic material will typically vary with different pairs of principal material directions. Finally, the magnitude of the in-plane shearing deformation in an orthotropic layer is also independent from the elastic moduli and Poisson's Ratios. As discussed below, there are four unique material properties needed to describe the in-plane mechanical behavior of orthotropic materials.

Modeling of Orthotropic Material Thermal Expansion

The relationship between the free thermal expansion and temperature change of a material is often modeled using a linear relationship

$$\varepsilon_T = \alpha \cdot \Delta T \tag{1}$$

where ε_T is the thermal-induced strain, α is the coefficient of thermal expansion (CTE) of the material, and ΔT is the change in temperature. Thin orthotropic materials have two principal material directions in the plane of the layer. The x_1-direction is the primary principal material direction, which is normally the stiffest direction. Moreover, the x_2-direction is the in-plane direction perpendicular to the x_1-direction. The thermal strains upon these two directions are normally different. Thus, eq. (1) is typically generalized as

$$(\varepsilon_1)_T = \alpha_1 \cdot \Delta T \tag{2}$$

$$(\varepsilon_2)_T = \alpha_2 \cdot \Delta T \qquad (3)$$

where $(\varepsilon_1)_T$ and $(\varepsilon_2)_T$ are the thermal strains in the principal material directions, and α_1 and α_2 are the coefficients of thermal expansion in the principal material directions. During a temperature change, no thermally induced shear strains are produced in the coordinate system aligned along the directions of material symmetry.

Stress-Strain Relations and Material Properties for a Single Orthotropic Layer

A typical fiber reinforced layer is shown in Figure 2. The principal material directions of a constituent ply or lamina are denoted by 1, 2, and 3. They will often not be aligned with the chosen coordinate directions, denoted by x, y, and z. This is illustrated in Figure 3 for the case of rotation of angle θ about z-axis.

Linear elastic stress-strain relations are often used to model an individual layer. For the case of plane stress in the 1-2-3 coordinate system, the plane stress version of linear elastic stress-strain relations for an orthotropic lamina exposed to a thermal/temperature change have the form

$$\begin{bmatrix} \sigma_1 \\ \sigma_2 \\ \tau_{12} \end{bmatrix} = \begin{bmatrix} Q_{11} & Q_{12} & 0 \\ Q_{12} & Q_{22} & 0 \\ 0 & 0 & Q_{66} \end{bmatrix} \begin{bmatrix} \varepsilon_1 - \alpha_1 \Delta T \\ \varepsilon_2 - \alpha_2 \Delta T \\ \gamma_{12} \end{bmatrix} \qquad (4)$$

where σ_1, σ_2, τ_{12} are the in-plane normal and shear stresses, and ε_1, ε_2, γ_{12} are the in-plane normal and shear strains. The coefficients Q_{ij} in eq. (4) are the reduced stiffness's of the material that can be evaluated from the material properties of the layer using the following relations:

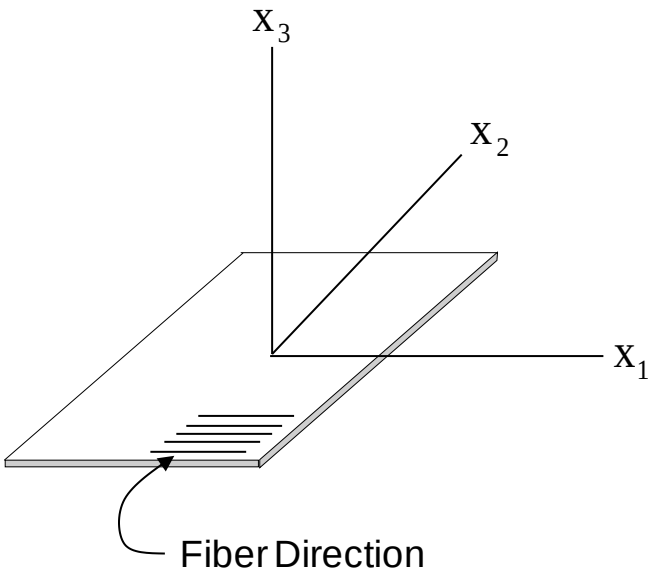

Figure 2. Single Fiber-Reinforced Layer

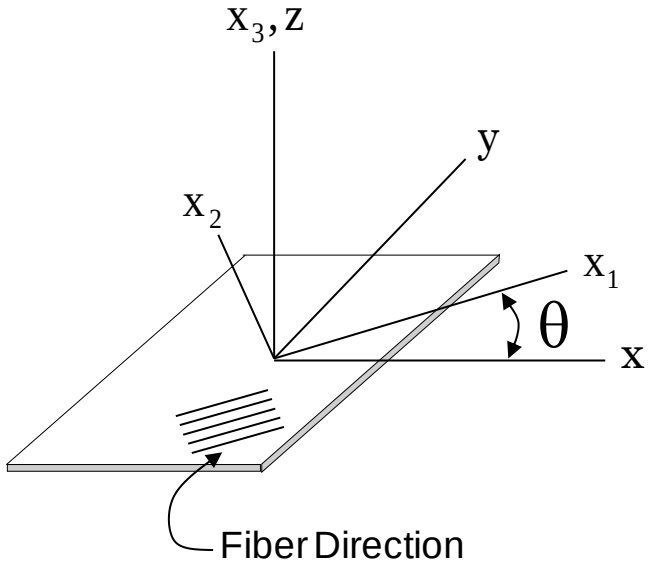

Figure 3. Single Fiber-Reinforced Layer with Fiber Angle θ

$$
\begin{aligned}
Q_{11} &= \frac{E_1}{\left(1-\nu_{12}\nu_{21}\right)} \\
Q_{22} &= \frac{E_2}{\left(1-\nu_{12}\nu_{21}\right)} \\
Q_{12} &= Q_{21} = \frac{\nu_{12}E_2}{\left(1-\nu_{12}\nu_{21}\right)} = \frac{\nu_{21}E_1}{\left(1-\nu_{12}\nu_{21}\right)} \\
Q_{66} &= G_{12} \\
Q_{16} &= Q_{26} = 0
\end{aligned}
\tag{5}
$$

where E_1 and E_2 are the elastic moduli, ν_{12} and ν_{21} are the Poisson's Ratios, and G_{12} is the shear modulus. Furthermore, it should be noted that the strains (ε_1, ε_2, γ_{12}) in eq. (4) are the total strains including both mechanical and thermal (CTE) induced contributions.

From the basic theory of mechanics of materials, the transformation relationships for the in-plane stresses and strains are

$$
\begin{pmatrix} \sigma_1 \\ \sigma_2 \\ \tau_{12} \end{pmatrix} = \left[T(\theta)\right] \begin{pmatrix} \sigma_x \\ \sigma_y \\ \tau_{xy} \end{pmatrix} \tag{6}
$$

and

$$
\begin{pmatrix} \varepsilon_1 \\ \varepsilon_2 \\ \frac{\gamma_{12}}{2} \end{pmatrix} = \left[T(\theta)\right] \begin{pmatrix} \varepsilon_x \\ \varepsilon_y \\ \frac{\gamma_{xy}}{2} \end{pmatrix} \tag{7}
$$

The transformation matrix $\left[T(\theta)\right]$ in eqs. (6,7) is given by

$$
\left[T(\theta)\right] = \begin{bmatrix} m^2 & n^2 & 2mn \\ n^2 & m^2 & -2mn \\ -mn & mn & \left(m^2-n^2\right) \end{bmatrix} \tag{8}
$$

where $m = \cos\theta$, $n = \sin\theta$, and positive θ are defined as shown in Figure 2. The inverse of this matrix is easily evaluated to be

$$\left[T(\theta)\right]^{-1} = \begin{bmatrix} m^2 & n^2 & 2mn \\ n^2 & m^2 & -2mn \\ -mn & mn & \left(m^2 - n^2\right) \end{bmatrix} = \left[T(-\theta)\right] \tag{9}$$

Equation (7) can be used to characterize the transformation of the coefficients of thermal expansion by applying it to the thermal expansion strains. In this case, the strain transformations have the form

$$\begin{pmatrix} (\varepsilon_1)_T \\ (\varepsilon_2)_T \\ 0 \end{pmatrix} = \left[T(\theta)\right] \begin{pmatrix} (\varepsilon_x)_T \\ (\varepsilon_y)_T \\ \left(\frac{\gamma_{xy}}{2}\right)_T \end{pmatrix} \tag{10}$$

or

$$\begin{pmatrix} \alpha_1 \Delta T \\ \alpha_2 \Delta T \\ 0 \end{pmatrix} = \left[T(\theta)\right] \begin{pmatrix} \alpha_x \Delta T \\ \alpha_y \Delta T \\ \frac{\alpha_{xy}}{2} \Delta T \end{pmatrix} \tag{11}$$

where α_x, α_y, and α_{xy} are the in-plane coefficients of thermal expansion for the x-y-z coordinate system. Inversion of eq. (11) leads to

$$\begin{pmatrix} \alpha_x \\ \alpha_y \\ \frac{\alpha_{xy}}{2} \end{pmatrix} = \left[T(-\theta)\right] \begin{pmatrix} \alpha_1 \\ \alpha_2 \\ 0 \end{pmatrix} \tag{12}$$

It is important to note that α_{xy} is often not zero. In other words, shear strains can be generated in an off-axis coordinate system when the temperature of the lamina changes.

Substitution of eqs. (6-9,12) into eq. (4) gives the plane stress version of the off-axis stress-strain relations in the x-y-z coordinate system as

$$\begin{bmatrix} \sigma_x \\ \sigma_y \\ \tau_{xy} \end{bmatrix} = \begin{bmatrix} \overline{Q}_{11} & \overline{Q}_{12} & \overline{Q}_{16} \\ \overline{Q}_{12} & \overline{Q}_{22} & \overline{Q}_{26} \\ \overline{Q}_{16} & \overline{Q}_{26} & \overline{Q}_{66} \end{bmatrix} \begin{bmatrix} \varepsilon_x - \alpha_x \Delta T \\ \varepsilon_y - \alpha_y \Delta T \\ \gamma_{xy} - \alpha_{xy} \Delta T \end{bmatrix} \tag{13}$$

where

$$\begin{aligned} \overline{Q}_{11} &= Q_{11}m^4 + 2\left(Q_{12} + 2Q_{66}\right)m^2n^2 + Q_{22}n^4 \\ \overline{Q}_{12} &= \left(Q_{11} + Q_{22} - 4Q_{66}\right)m^4n^4 + Q_{12}\left(m^4 + n^4\right) \\ \overline{Q}_{22} &= Q_{11}n^4 + 2\left(Q_{12} + 2Q_{66}\right)m^2n^2 + Q_{22}m^4 \\ \overline{Q}_{16} &= \left(Q_{11} - Q_{12} - 2Q_{66}\right)m^3n + \left(Q_{12} - Q_{22} + 2Q_{66}\right)mn^3 \\ \overline{Q}_{26} &= \left(Q_{11} - Q_{12} - 2Q_{66}\right)mn^3 + \left(Q_{12} - Q_{22} + 2Q_{66}\right)m^3n \\ \overline{Q}_{66} &= \left(Q_{11} + Q_{22} - 2Q_{12} - 2Q_{66}\right)m^2n^2 + Q_{66}\left(m^4 + n^4\right) \end{aligned} \tag{14}$$

are the transformed reduced stiffness coefficients. Expressions for the transformed coefficient of thermal expansion in eq. (13) are obtained by expanding eq. (12) to

$$\begin{aligned} \alpha_x &= \alpha_1 m^2 + \alpha_2 n^2 \\ \alpha_y &= \alpha_2 m^2 + \alpha_1 n^2 \\ \alpha_{xy} &= \left(\alpha_1 - \alpha_2\right)mn \end{aligned} \tag{15}$$

Analysis of Laminated Plates

As discussed previously, a typical fiber reinforced laminate is often constructed by stacking and bonding multiple orthotropic and/or isotropic layers together. An example is shown in Figure 4. In this section, the general theory for the thermal-mechanical behavior of laminated fiber-reinforced materials is presented. This formulation is usually known as composite material lamination theory [6]. In this development, each layer is considered as linear elastic and the laminate experiences only small out-of-plane deformations.

A general illustration of a laminate composed of N lamina is shown in Figure 5. The layers of the laminate are numbered as 1, 2, 3,…,N from top to bottom. Each orthotropic ply is also associated with an angle θ which represents the orientation of the 1-direction for that ply. The angle between the 1-direction of the kth layer and the x-axis is denoted θ_k, where subscript k is the notation for the kth ply of the laminate. The z-axis is taken to be perpendicular to the plate with the positive downward direction and z = 0 at the middle surface.

A basic assumption of lamination theory is that the out-of-plane stresses are negligible in comparison to the in-plane stresses. Therefore, the plane stress version of orthotropic Hooke's law can be used for representing the linear elastic layers of the plate. Using eq. (13), the stress-strain relations for the kth layer are

$$\begin{bmatrix} \sigma_x \\ \sigma_y \\ \tau_{xy} \end{bmatrix}_k = \begin{bmatrix} \overline{Q}_{11} & \overline{Q}_{12} & \overline{Q}_{16} \\ \overline{Q}_{12} & \overline{Q}_{22} & \overline{Q}_{26} \\ \overline{Q}_{16} & \overline{Q}_{26} & \overline{Q}_{66} \end{bmatrix}_k \begin{bmatrix} \varepsilon_x - \alpha_x \Delta T \\ \varepsilon_y - \alpha_y \Delta T \\ \gamma_{xy} - \alpha_{xy} \Delta T \end{bmatrix}_k \qquad (16)$$

where the subscript k on the reduced stiffness matrix implies that the material properties and angle θ appropriate for kth layer should be used to evaluate the $\overline{Q}_{ij}$ coefficients.

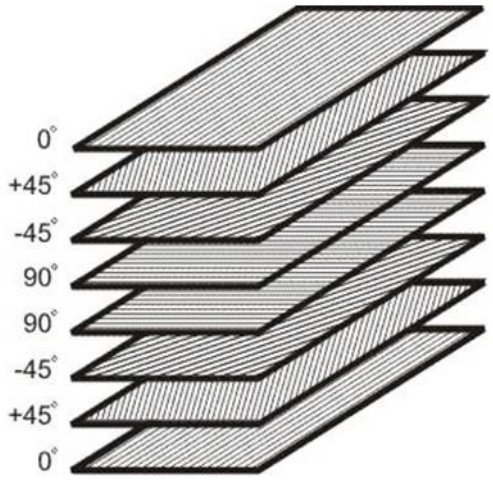

Figure 4. Various Angle Layers Stack Up Illustration

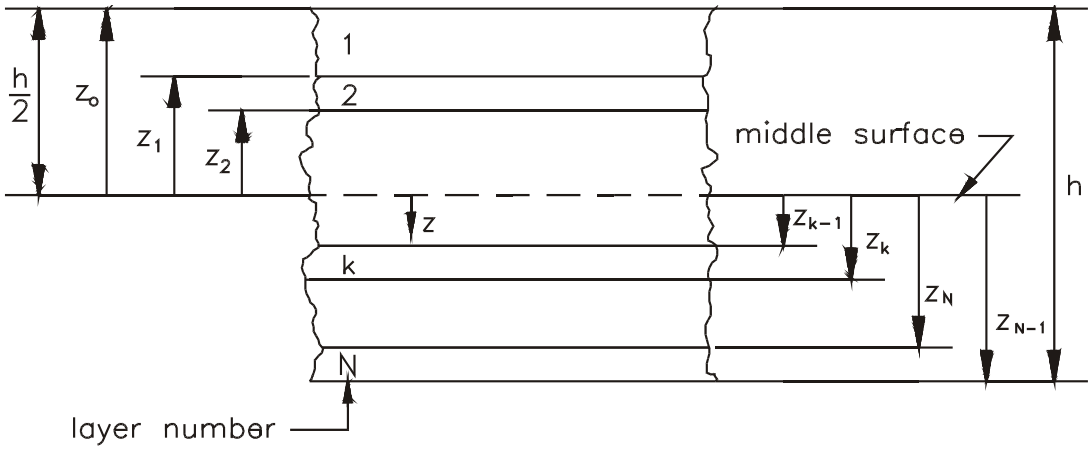

Figure 5. Illustration of N-ply Laminate Composition

The linearized strain-displacement relations for a body experiencing small strains and deformations are

$$\begin{aligned}
\varepsilon_x &= \frac{\partial u}{\partial x} \\
\varepsilon_y &= \frac{\partial v}{\partial y} \\
\varepsilon_z &= \frac{\partial w}{\partial z} \\
\gamma_{xz} &= \frac{1}{2}\left(\frac{\partial u}{\partial z} + \frac{\partial w}{\partial x}\right) \\
\gamma_{yz} &= \frac{1}{2}\left(\frac{\partial v}{\partial z} + \frac{\partial w}{\partial y}\right) \\
\gamma_{xy} &= \frac{1}{2}\left(\frac{\partial u}{\partial y} + \frac{\partial v}{\partial x}\right)
\end{aligned} \tag{17}$$

where u, v, w are the displacements in the x, y, z directions. The other standard assumption used in lamination theory is that the change in thickness dimension is relatively small and negligible. Using the third equation of eq. (17), rewritten as eq. (18).

$$\varepsilon_z = \frac{\partial w}{\partial z} \approx 0 \tag{18}$$

Another classic assumption is that “Plane sections remain plane after loading”. This implies that the out-of-plane shear strains γ_{xz} and γ_{yz} are approximately equal to zero. From the fourth and fifth sub-equations in eq. (17), this assumption becomes

$$\begin{aligned}
\gamma_{xz} &= \frac{1}{2}\left(\frac{\partial u}{\partial z} + \frac{\partial w}{\partial x}\right) \approx 0 \\
\gamma_{yz} &= \frac{1}{2}\left(\frac{\partial v}{\partial z} + \frac{\partial w}{\partial y}\right) \approx 0
\end{aligned} \tag{19}$$

If eqs. (18,19) are assumed to be equalities and integrated, the following results are obtained for the laminated plate displacement fields:

$$\begin{aligned} u &= U_0(x,y) - z\frac{\partial w}{\partial x} \\ v &= V_0(x,y) - z\frac{\partial w}{\partial y} \\ w &= w(x,y) \end{aligned} \tag{20}$$

where $U_0(x,y)$, $V_0(x,y)$ are the middle surface in-plane displacement fields.

Substituting eq. (20) into eqs. (17) gives the general form for the in-plane strain fields of the laminated plate

$$\begin{aligned} \varepsilon_x &= \frac{\partial U_0(x,y)}{\partial x} - z\frac{\partial^2 w}{\partial x^2} \\ \varepsilon_x &= \frac{\partial V_0(x,y)}{\partial y} - z\frac{\partial^2 w}{\partial y^2} \\ \gamma_{xy} &= \frac{\partial U_0(x,y)}{\partial y} + \frac{\partial V_0(x,y)}{\partial x} - 2z\frac{\partial^2 w}{\partial x \partial y} \end{aligned} \tag{21}$$

The form of these relations is usually simplified by introducing additional notations for the middle surface strains and curvatures. The three middle surface strains (z = 0) are defined as

$$\begin{aligned} \varepsilon_x^0 &= \frac{\partial U_0(x,y)}{\partial x} \\ \varepsilon_y^0 &= \frac{\partial V_0(x,y)}{\partial y} \\ \gamma_{xy}^0 &= \frac{\partial U_0(x,y)}{\partial y} + \frac{\partial V_0(x,y)}{\partial x} \end{aligned} \tag{22}$$

and the three middle surface curvatures are defined as

$$\kappa_x = -\frac{\partial^2 w}{\partial x^2}$$
$$\kappa_y = -\frac{\partial^2 w}{\partial y^2} \qquad (23)$$
$$\kappa_x = -2\frac{\partial^2 w}{\partial x \partial y}$$

The six expressions showed in eqs. (22, 23) are a set of equivalent strain-displacement relations for the mid-surface strains and curvatures of the laminated plate. Using these definitions, eq. (21) can be rewritten in matrix form as

$$\begin{pmatrix} \varepsilon_x \\ \varepsilon_y \\ \gamma_{xy} \end{pmatrix} = \begin{bmatrix} \varepsilon_x^0 \\ \varepsilon_y^0 \\ \gamma_{xy}^0 \end{bmatrix} + z \begin{bmatrix} \kappa_x \\ \kappa_y \\ \kappa_{xy} \end{bmatrix} \qquad (24)$$

From eqs. (20, 24) it is clear that the in-plane displacement and strain fields vary linearly through the thickness of the laminated composite material.

Substituting the results given in eq. (24) into eq. (16) gives the in-plane stress-strain relations for the laminated composite material plate in matrix form

$$\begin{bmatrix} \sigma_x \\ \sigma_y \\ \tau_{xy} \end{bmatrix}_k = \begin{bmatrix} \overline{Q}_{11} & \overline{Q}_{12} & \overline{Q}_{16} \\ \overline{Q}_{12} & \overline{Q}_{22} & \overline{Q}_{26} \\ \overline{Q}_{16} & \overline{Q}_{26} & \overline{Q}_{66} \end{bmatrix}_k \left\{ \begin{bmatrix} \varepsilon_x^0 \\ \varepsilon_y^0 \\ \gamma_{xy}^0 \end{bmatrix} + z \begin{bmatrix} \kappa_x \\ \kappa_y \\ \kappa_{xy} \end{bmatrix} - \begin{bmatrix} \alpha_x \\ \alpha_y \\ \alpha_{xy} \end{bmatrix} \Delta T \right\}_k \qquad (25)$$

From eq. (25), it can be seen that the in-plane stresses vary linearly in any given layer of the laminated plate. However, the behavior is piecewise linear with discontinuities when graphing the stresses through the entire thickness of laminate. This is due to the fact that the values of the reduced stiffnesses $\overline{Q}_{ij}$ can vary discontinuously from one layer to the other.

From the development of classical plate theory [6], internal forces and moments per unit length can be defined and used as auxiliary variables which are related to the stresses but

independent of the thickness coordinate z. The in-plane forces per unit length or in-plane force resultants are defined as integrals of the in-plane stresses through the thickness of the plate as

$$N_x = \int_{-\frac{h}{2}}^{+\frac{h}{2}} \sigma_x dz$$
$$N_y = \int_{-\frac{h}{2}}^{+\frac{h}{2}} \sigma_y dz \qquad (26)$$
$$N_{xy} = \int_{-\frac{h}{2}}^{+\frac{h}{2}} \tau_{xy} dz = N_{yx}$$

where h is the thickness of the plate. The shear forces per unit length or the shear force resultants are similarly defined as the integrals of the out-of-plane shear stresses through the thickness of the plate

$$Q_x = \int_{-\frac{h}{2}}^{+\frac{h}{2}} \tau_{xz} dz$$
$$Q_y = \int_{-\frac{h}{2}}^{+\frac{h}{2}} \tau_{yz} dz \qquad (27)$$

The moments per unit length or the moment resultants are defined as the integrals of the moment of the in-plane stresses through the thickness of the plate as

$$M_x = \int_{-\frac{h}{2}}^{+\frac{h}{2}} \sigma_x z dz$$
$$M_y = \int_{-\frac{h}{2}}^{+\frac{h}{2}} \sigma_y z dz \qquad (28)$$
$$M_{xy} = \int_{-\frac{h}{2}}^{+\frac{h}{2}} \tau_{xy} z dz = M_{yx}$$

In these relations, both the force and moment resultants depend only on coordinates x and y. On the plate elements illustrated in Figures 6 and 7, the positive directions of all of the force and moment resultants are shown, which are consistent with the positive directions of the stresses integrated in eqs. (26-28).

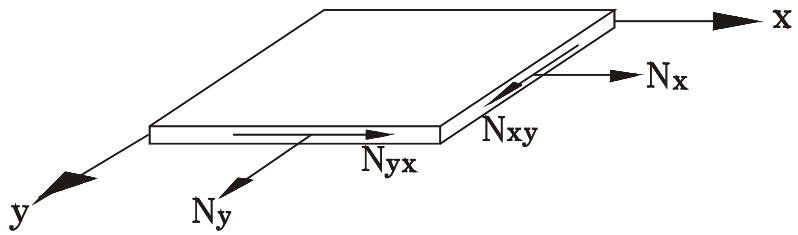

Figure 6. Positive Direction for the Force Resultants on the Laminate

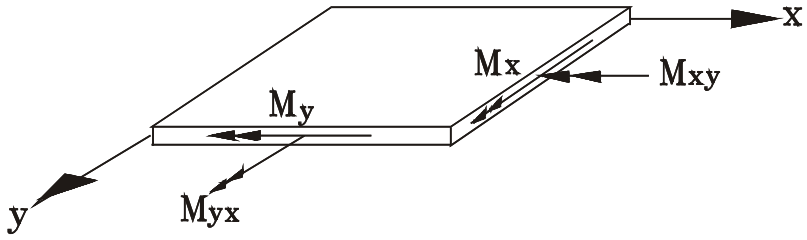

Figure 7. Positive Directions for the Moment Resultants on the Laminate

For laminated plate calculations, eq. (26) is applied to evaluate the in-plane force resultants by integrating through each layer. Furthermore, the results from each individual layer are been added to treat as a bulk material.

$$\begin{Bmatrix} N_x \\ N_y \\ N_{xy} \end{Bmatrix} = \int_{-\frac{h}{2}}^{+\frac{h}{2}} \begin{bmatrix} \sigma_x \\ \sigma_y \\ \tau_{xy} \end{bmatrix} dz = \sum_{k=1}^{N} \int_{z_{k-1}}^{z_k} \begin{bmatrix} \sigma_x \\ \sigma_y \\ \tau_{xy} \end{bmatrix}_k dz \tag{29}$$

where z_k and z_{k-1} are the distances to the ply interfaces of the kth ply (see Figure 3). By substituting eq. (25) into eq. (29), the following expression results:

$$\begin{Bmatrix} N_x \\ N_y \\ N_{xy} \end{Bmatrix} = \sum_{k=1}^{N} \int_{z_{k-1}}^{z_k} \left(\begin{bmatrix} \overline{Q}_{11} & \overline{Q}_{12} & \overline{Q}_{16} \\ \overline{Q}_{12} & \overline{Q}_{22} & \overline{Q}_{26} \\ \overline{Q}_{16} & \overline{Q}_{26} & \overline{Q}_{66} \end{bmatrix}_k \left\{ \begin{bmatrix} \varepsilon_x^0 \\ \varepsilon_y^0 \\ \gamma_{xy}^0 \end{bmatrix} + z \begin{bmatrix} \kappa_x \\ \kappa_y \\ \kappa_{xy} \end{bmatrix} - \begin{bmatrix} \alpha_x \\ \alpha_y \\ \alpha_{xy} \end{bmatrix} \Delta T \right\}_k \right) dz \tag{30}$$

The integrands in eq. (30) contain only terms that are constant and linear in z. These can be easily integrated to give

$$\begin{Bmatrix} N_x \\ N_y \\ N_{xy} \end{Bmatrix} = \begin{bmatrix} A_{11} & A_{12} & A_{16} \\ A_{12} & A_{22} & A_{26} \\ A_{16} & A_{26} & A_{66} \end{bmatrix}_k \begin{Bmatrix} \varepsilon_x^0 \\ \varepsilon_y^0 \\ \gamma_{xy}^0 \end{Bmatrix} + \begin{bmatrix} B_{11} & B_{12} & B_{16} \\ B_{12} & B_{22} & B_{26} \\ B_{16} & B_{26} & B_{66} \end{bmatrix} \begin{Bmatrix} \kappa_x \\ \kappa_y \\ \kappa_{xy} \end{Bmatrix} - \begin{Bmatrix} N_x^T \\ N_y^T \\ N_{xy}^T \end{Bmatrix} \tag{31}$$

or in concise form

$$\{N\} = [A]\{\varepsilon^0\} + [B]\{\kappa\} - \{N^T\} \tag{32}$$

where

$$\begin{aligned} A_{ij} &= \sum_{k=1}^{N} \left(\overline{Q}_{ij}\right)_k \left[z_k - z_{k-1}\right] \\ B_{ij} &= \frac{1}{2} \sum_{k=1}^{N} \left(\overline{Q}_{ij}\right)_k \left[{z_k}^2 - {z_{k-1}}^2\right] \\ &\left[i, j = 1,2,6\right] \end{aligned} \tag{33}$$

Here, A_{ij} are the extensional stiffnesses, and B_{ij} are the coupling stiffnesses. The thermal stress term in eqs. (31, 32) is calculated from

$$\begin{Bmatrix} N_x^T \\ N_y^T \\ N_{xy}^T \end{Bmatrix} = \sum_{k=1}^{N} \int_{z_{k-1}}^{z_k} \begin{bmatrix} \overline{Q}_{11} & \overline{Q}_{12} & \overline{Q}_{16} \\ \overline{Q}_{12} & \overline{Q}_{22} & \overline{Q}_{26} \\ \overline{Q}_{16} & \overline{Q}_{26} & \overline{Q}_{66} \end{bmatrix}_k \begin{bmatrix} \alpha_x \\ \alpha_y \\ \alpha_{xy} \end{bmatrix}_k \Delta T dz \tag{34}$$

By using a similar procedure, the moment resultants can also be expressed in terms of the mid-surface strains and curvatures. The integrals for each single layer can be obtained by breaking up the stacked total thickness integral.

$$\begin{Bmatrix} M_x \\ M_y \\ M_{xy} \end{Bmatrix} = \int_{-\frac{h}{2}}^{+\frac{h}{2}} \begin{bmatrix} \sigma_x \\ \sigma_y \\ \tau_{xy} \end{bmatrix} z dz = \sum_{k=1}^{N} \int_{z_{k-1}}^{z_k} \begin{bmatrix} \sigma_x \\ \sigma_y \\ \tau_{xy} \end{bmatrix}_k z dz \tag{35}$$

Combining eq. (25) and (35), leads to

$$\begin{Bmatrix} M_x \\ M_y \\ M_{xy} \end{Bmatrix} = \sum_{k=1}^{N} \int_{z_{k-1}}^{z_k} \left(\begin{bmatrix} \overline{Q}_{11} & \overline{Q}_{12} & \overline{Q}_{16} \\ \overline{Q}_{12} & \overline{Q}_{22} & \overline{Q}_{26} \\ \overline{Q}_{16} & \overline{Q}_{26} & \overline{Q}_{66} \end{bmatrix}_k \left\{ z \begin{bmatrix} \varepsilon_x^0 \\ \varepsilon_y^0 \\ \gamma_{xy}^0 \end{bmatrix} + z^2 \begin{bmatrix} \kappa_x \\ \kappa_y \\ \kappa_{xy} \end{bmatrix} - \begin{bmatrix} \alpha_x \\ \alpha_y \\ \alpha_{xy} \end{bmatrix} z \Delta T \right\}_k \right) dz \tag{36}$$

Integrating eq. (36) then gives:

$$\begin{Bmatrix} M_x \\ M_y \\ M_{xy} \end{Bmatrix} = \begin{bmatrix} B_{11} & B_{12} & B_{16} \\ B_{12} & B_{22} & B_{26} \\ B_{16} & B_{26} & B_{66} \end{bmatrix}_k \begin{Bmatrix} \varepsilon_x^0 \\ \varepsilon_y^0 \\ \gamma_{xy}^0 \end{Bmatrix} + \begin{bmatrix} D_{11} & D_{12} & D_{16} \\ D_{12} & D_{22} & D_{26} \\ D_{16} & D_{26} & D_{66} \end{bmatrix} \begin{Bmatrix} \kappa_x \\ \kappa_y \\ \kappa_{xy} \end{Bmatrix} - \begin{Bmatrix} M_x^T \\ M_y^T \\ M_{xy}^T \end{Bmatrix} \tag{37}$$

or in concise form

$$\{M\} = [B]\{\varepsilon^0\} + [D]\{\kappa\} - \{M^T\} \tag{38}$$

The coupling stiffnesses B_{ij} in eqs. (37, 38) have already been defined in eq. (33). The bending stiffnesses D_{ij} are defined as

$$D_{ij} = \frac{1}{3}\sum_{k=1}^{N}\left(\overline{Q}_{ij}\right)_k\left[{z_k}^3 - {z_{k-1}}^3\right] \quad [i, j = 1,2,6] \tag{39}$$

And the thermally-induced moment term can be expressed as

$$\begin{Bmatrix} M_x^T \\ M_y^T \\ M_{xy}^T \end{Bmatrix} = \sum_{k=1}^{N}\int_{z_{k-1}}^{z_k} \begin{bmatrix} \overline{Q}_{11} & \overline{Q}_{12} & \overline{Q}_{16} \\ \overline{Q}_{12} & \overline{Q}_{22} & \overline{Q}_{26} \\ \overline{Q}_{16} & \overline{Q}_{26} & \overline{Q}_{66} \end{bmatrix}_k \begin{bmatrix} \alpha_x \\ \alpha_y \\ \alpha_{xy} \end{bmatrix}_k \Delta T z dz \tag{40}$$

By combining eq. (31) and (37), the following 6 × 6 matrix equation can be established:

$$\begin{Bmatrix} N_x \\ N_y \\ N_{xy} \\ M_x \\ M_y \\ M_{xy} \end{Bmatrix} = \begin{bmatrix} A_{11} & A_{12} & A_{16} & B_{11} & B_{12} & B_{16} \\ A_{12} & A_{22} & A_{26} & B_{12} & B_{22} & B_{26} \\ A_{16} & A_{26} & A_{66} & B_{16} & B_{26} & B_{66} \\ B_{11} & B_{12} & B_{16} & D_{11} & D_{12} & D_{16} \\ B_{12} & B_{22} & B_{26} & D_{12} & D_{22} & D_{26} \\ B_{16} & B_{26} & B_{66} & D_{16} & D_{26} & D_{66} \end{bmatrix} \begin{Bmatrix} \varepsilon_x^0 \\ \varepsilon_y^0 \\ \gamma_{xy}^0 \\ \kappa_x^0 \\ \kappa_y^0 \\ \kappa_{xy}^0 \end{Bmatrix} - \begin{Bmatrix} N_x^T \\ N_y^T \\ N_{xy}^T \\ M_x^T \\ M_y^T \\ M_{xy}^T \end{Bmatrix} \tag{41}$$

This relation is the well-known governing equation of composite material lamination theory and can be rewritten in concise form as

$$\begin{Bmatrix} N \\ M \end{Bmatrix} = \begin{bmatrix} A & B \\ B & D \end{bmatrix} \begin{Bmatrix} \varepsilon^0 \\ \kappa \end{Bmatrix} - \begin{Bmatrix} N^T \\ M^T \end{Bmatrix} \tag{42}$$

For the case of a symmetric laminate (B_{ij} = 0) and no mechanical loading (N_x, N_y, and N_{xy} are 0), eq. (31) can be rewritten as

$$\begin{Bmatrix} 0 \\ 0 \\ 0 \end{Bmatrix} = \begin{bmatrix} A_{11} & A_{12} & A_{16} \\ A_{12} & A_{22} & A_{26} \\ A_{16} & A_{26} & A_{66} \end{bmatrix} \begin{Bmatrix} \varepsilon_x^0 \\ \varepsilon_y^0 \\ \gamma_{xy}^0 \end{Bmatrix} - \begin{Bmatrix} N_x^T \\ N_y^T \\ N_{xy}^T \end{Bmatrix} \tag{43}$$

or

$$\begin{Bmatrix} N_x^T \\ N_y^T \\ N_{xy}^T \end{Bmatrix} = \begin{bmatrix} A_{11} & A_{12} & A_{16} \\ A_{12} & A_{22} & A_{26} \\ A_{16} & A_{26} & A_{66} \end{bmatrix} \begin{Bmatrix} \varepsilon_x^0 \\ \varepsilon_y^0 \\ \gamma_{xy}^0 \end{Bmatrix} \tag{44}$$

This result can be inverted to give

$$\begin{Bmatrix} \varepsilon_x^0 \\ \varepsilon_y^0 \\ \gamma_{xy}^0 \end{Bmatrix} = \begin{bmatrix} A_{11}^{-1} & A_{12}^{-1} & A_{13}^{-1} \\ A_{21}^{-1} & A_{22}^{-1} & A_{23}^{-1} \\ A_{31}^{-1} & A_{32}^{-1} & A_{33}^{-1} \end{bmatrix} \begin{Bmatrix} N_x^T \\ N_y^T \\ N_{xy}^T \end{Bmatrix} \tag{45}$$

If the thermal loading consists of a uniform temperature change, eq. (34) can be rewritten as

$$\begin{Bmatrix} N_x^T \\ N_y^T \\ N_{xy}^T \end{Bmatrix} = \sum_{k=1}^{N} \begin{bmatrix} \overline{Q}_{11} & \overline{Q}_{12} & \overline{Q}_{16} \\ \overline{Q}_{12} & \overline{Q}_{22} & \overline{Q}_{26} \\ \overline{Q}_{16} & \overline{Q}_{26} & \overline{Q}_{66} \end{bmatrix}_k \begin{bmatrix} \alpha_x \\ \alpha_y \\ \alpha_{xy} \end{bmatrix}_k h_k \Delta T \tag{46}$$

where h_k is the thickness of the k_{th} layer

Substitution of eq. (46) into eq. (45) yields

$$\begin{Bmatrix} \varepsilon_x^0 \\ \varepsilon_y^0 \\ \gamma_{xy}^0 \end{Bmatrix} = \left[\sum_{k=1}^{N} \begin{bmatrix} A_{11}^{-1} & A_{12}^{-1} & A_{13}^{-1} \\ A_{21}^{-1} & A_{22}^{-1} & A_{23}^{-1} \\ A_{31}^{-1} & A_{32}^{-1} & A_{33}^{-1} \end{bmatrix} \begin{bmatrix} \overline{Q}_{11} & \overline{Q}_{12} & \overline{Q}_{16} \\ \overline{Q}_{12} & \overline{Q}_{22} & \overline{Q}_{26} \\ \overline{Q}_{16} & \overline{Q}_{26} & \overline{Q}_{66} \end{bmatrix}_k \begin{bmatrix} \alpha_x \\ \alpha_y \\ \alpha_{xy} \end{bmatrix}_k h_k \right] \Delta T \tag{47}$$

The effective (average) CTE of a laminate can be obtained by rewriting eq. (1) as:

$$\alpha^\circ = \frac{\varepsilon_T^\circ}{\Delta T} \tag{48}$$

Thus, eq. (47) can be rearranged to yield expressions for the effective (average) expansion coefficients of the laminate:

$$\begin{bmatrix} \alpha_x^0 \\ \alpha_y^0 \\ \alpha_{xy}^0 \end{bmatrix} = \begin{Bmatrix} \dfrac{\varepsilon_x^0}{\Delta T} \\ \dfrac{\varepsilon_y^0}{\Delta T} \\ \dfrac{\gamma_{xy}^0}{\Delta T} \end{Bmatrix} = \left[\sum_{k=1}^{N} \begin{bmatrix} A_{11}^{-1} & A_{12}^{-1} & A_{13}^{-1} \\ A_{21}^{-1} & A_{22}^{-1} & A_{23}^{-1} \\ A_{31}^{-1} & A_{32}^{-1} & A_{33}^{-1} \end{bmatrix} \begin{bmatrix} \overline{Q}_{11} & \overline{Q}_{12} & \overline{Q}_{16} \\ \overline{Q}_{12} & \overline{Q}_{22} & \overline{Q}_{26} \\ \overline{Q}_{16} & \overline{Q}_{26} & \overline{Q}_{66} \end{bmatrix}_k \begin{bmatrix} \alpha_x \\ \alpha_y \\ \alpha_{xy} \end{bmatrix}_k h_k \right] \quad (49)$$

By using eq. (49), one can determine the surface (effective) CTEs for a laminated PCB, based on the relationship between thermal induced strain and temperature change. PCBs are typically constructed with symmetric layer configurations with all layers having fiber directions either at $\theta = 0^o$ or $\theta = 90^o$ [14]. In this case, the shear CTE α_{xy} will be zero for all layers.

There are seven material properties for each layer that need to be known in order to use eq. (49). The necessary material properties are α_1 (the coefficient of thermal expansion along first principal material direction), α_2 (the coefficient of thermal expansion along second principal material direction), E_1 (elastic modulus along the first principal material direction), E_2 (elastic modulus along the second principal material direction), ν_{12} and ν_{21} (Poisson's Ratios along first and second principal material directions), and G_{12} (shear modulus). These properties have been evaluated for several PCB layers as discussed in subsequent chapters.

III. STRAIN GAGE CALIBRATION AND MEASUREMENT EXPERIMENTS

Introduction

Most typical strain gages contain a long, thin conductive strip in a serpentine pattern of parallel lines as shown in Figure 8. By this particular formation, even a small amount of stress in the direction of the orientation of the parallel lines results in a multiplicatively larger strain over the effective length of the conductor. Strain gage measurements have been used to provide accurate, reliable, and repeatable test results on isotropic materials for the past 70 years. They were invented by Edward E. Simmons and Arthur C. Ruge in 1938. Strain gages typically contain two parts, a metallic foil pattern and an insulating flexible backing film on which the foil pattern is bonded. The strain gage backing film can be bonded to the target object with various kinds of adhesives, such as cyanoacrylate or epoxy adhesives. Due to the bonding, the metallic foil pattern on the strain gage will experience the same deformations as the specimen it is bonded to. Once the metallic foil is deformed, its electrical resistance will be changed and correlated to the degree of deformation. The changing resistance can be measured using a circuit such as a Wheatstone Bridge.

The main strain gage performance characteristics are the electrical conductance of the metal foil material and conductor's geometry. In the tension case, the strain testing is limited within the elastic limit of the metal foil such that it does not break or yield as shown in Figure 9. The end-to-end electrical resistance will be increased. In the compressive case, the conductor will tend to become shorter and broader if not buckled. It will result in decreasing the overall end-to-end resistance as shown in Figure 10. In either case, the change of resistance will alter

the output voltage when current is passing through the metal foil. The altered output voltage can be observed by voltage meter. Strain gages measure only local deformations under the bonded region.

The primary equation relating the resistance change to the strain is

$$\frac{\Delta R}{R} = (GF)\varepsilon \tag{50}$$

where ΔR is the change in resistance caused by strain, R is the resistance of the undeformed gage, ε is the strain, and GF is the gage factor. For metallic foil gages, the gage factor is usually around 2.0. When using a Wheatstone Bridge in a quarter bridge configuration, the output voltage from the bridge is:

$$V = \frac{BV \cdot GF \cdot \varepsilon}{4} \tag{51}$$

where BV is the bridge excitation voltage.

The excitation voltage is usually applied directly into the wires which are connected between the strain reader and strain gage terminals. Moreover, the typical input voltages are from 2V to 12V with output readings in millivolts. In this study, the excitation voltage has been set at 2V for all experiments, since higher excitation voltages tend to heat up the strain gage and raise the temperature of the metal foil, leading to measurement errors.

Strain gages are attached to the specimen with special adhesives. The type of adhesive depends on both the required lifetime of the measurement system and the specimen material type. For instance, cyanoacrylic adhesive is often used as the preferable adhesive with short term testing (usually weeks) and measurements done under normal room temperature. However, for long lasting installation and wide range temperature operation, an epoxy

adhesive will be the more ideal solution. Epoxy adhesives need to be cured with a high temperature (80 ^{o}C – 200 ^{o}C) curing profile in order to have an optimal bond to the specimen.

Temperature variation during testing will cause a multitude of effects on strain gage measurements. In order to compensate for thermal errors, two identical strain gages need to be mounted on two different objects made from the same material. The first strain gage needs to be mounted on the target specimen while the other strain gage (dummy gage) should be mounted on an unloaded material. Both materials should experience the same temperature change. Using two arms of a Wheatstone Bridge, the thermally induced errors in each gage will be subtracted and compensate for each other in the bridge output voltage.

Example Application and Verification of the Strain Gage Measurement

As a trial experiment to explore the accuracy of strain gages, an axial gage was mounted on a cantilever aluminum bar (with one clamped boundary). A concentrated load was applied at the top of the beam using a micrometer as shown in Figure 11. The strain gage was mounted near the clamped end of the bar, and the load was applied at the free end of the bar.

The strain gage used in this experiment was the general purpose strain gage CEA-250UN-350 manufactured by Vishay Measurements Group [22], and the measurement instrument was a Vishay Micro-Measurements Model 3800 Wide Range Strain Indicator. This instrument has a resolution of 1 $\mu\varepsilon$ at any gage factor from 0.0500 to 50.00. Moreover, the excitation voltage was changeable from 1 – 15 Vdc with 0.02% error.

The test cantilever bar was made of aluminum and had a thickness t = 0.248 inches, width b = 1.0 inches, length L = 10 inches, and the elastic modulus E = 10 x 10^{6} psi. The strain

gage measurements were recorded for every 0.025 inch change of the micrometer displacement. Since the micrometer displacements were increased linearly and the beam did not yield, the resulting strain measurements should also show a linear dependence on the applied beam deflection.

The classical beam theory solution for the out-of-plane deflection distribution of the cantilevered beam considered as

$$v(x)=\frac{PL^3}{EI}\left[\frac{1}{6}\left(\frac{x}{L}\right)^3-\frac{1}{2}\left(\frac{x}{L}\right)\right] \tag{50}$$

where v is the beam deflection, P is the applied concentrated load, E is the modulus of elasticity, I is the moment of inertia, x is the distance measured from the fix end, and L is the length of the beam. This expression can be rewritten in terms of the prescribed end deflection $\delta = v(L)$ which is applied by the micrometer. Plugging x = L into eq. (52) and solving for the applied load gives

$$P=\frac{3EI\delta}{L^3} \tag{51}$$

By substituting eq. (53) into eq. (52), the theoretical out-of-plane deflection distribution is found in terms of the end displacement applied by the micrometer

$$v(x)=3\delta\left[\frac{1}{6}\left(\frac{x}{L}\right)^3-\frac{1}{2}\left(\frac{x}{L}\right)\right] \tag{52}$$

The strain at the gage location can be calculated from beam theory as

$$\varepsilon_x=\left[\frac{3t\left(L-d\right)}{2L^3}\right]\delta=\left[\frac{3tD}{2L^3}\right]\delta \tag{53}$$

where ε_x is the strain at the gage location, δ is the deflection of beam at micrometer loading point, t is the beam thickness, L is the beam length, and d is the x-position of the strain gage.

Theoretical and experimental results for the surface strain at the gage location are listed in Table 1 and 2 for $D = 8.25$ and $D = 7.5$ inch. The experimental results were found to agree well with theoretical calculations, and the errors were found to be lower than 3%. The normalized plots of the out-of-plane displacement versus longitudinal position matched extremely well, which are shown in Figure 12 and 13. Based on the accurate results of these example tests, the strain gage measuring method is considered as an effective and accurate method for measuring specimen strain.

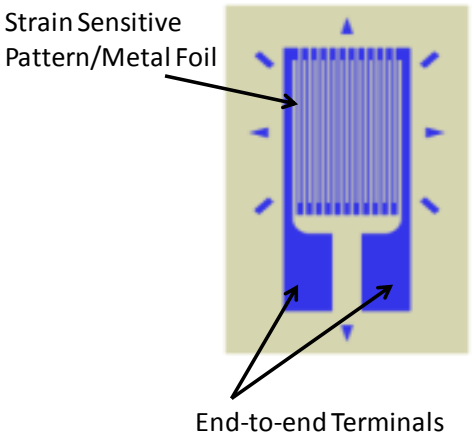

Figure 8. Typical Thin Film Metal Foil Strain Gage

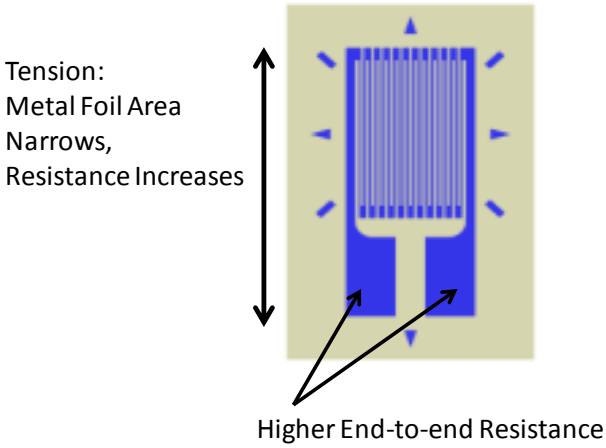

Figure 9. Tension Testing Using a Strain Gage

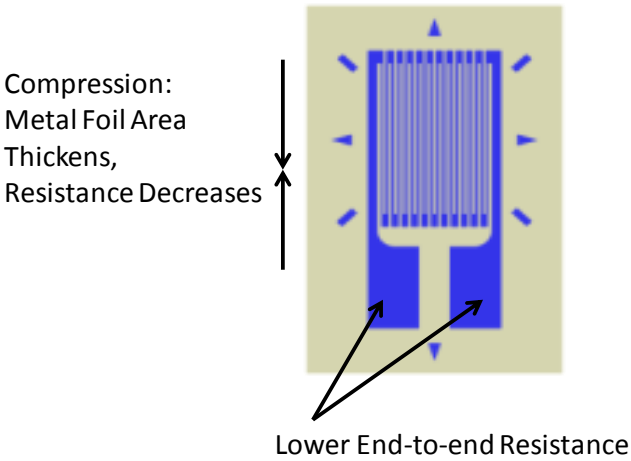

Figure 10. Compression Testing Using a Strain Gage

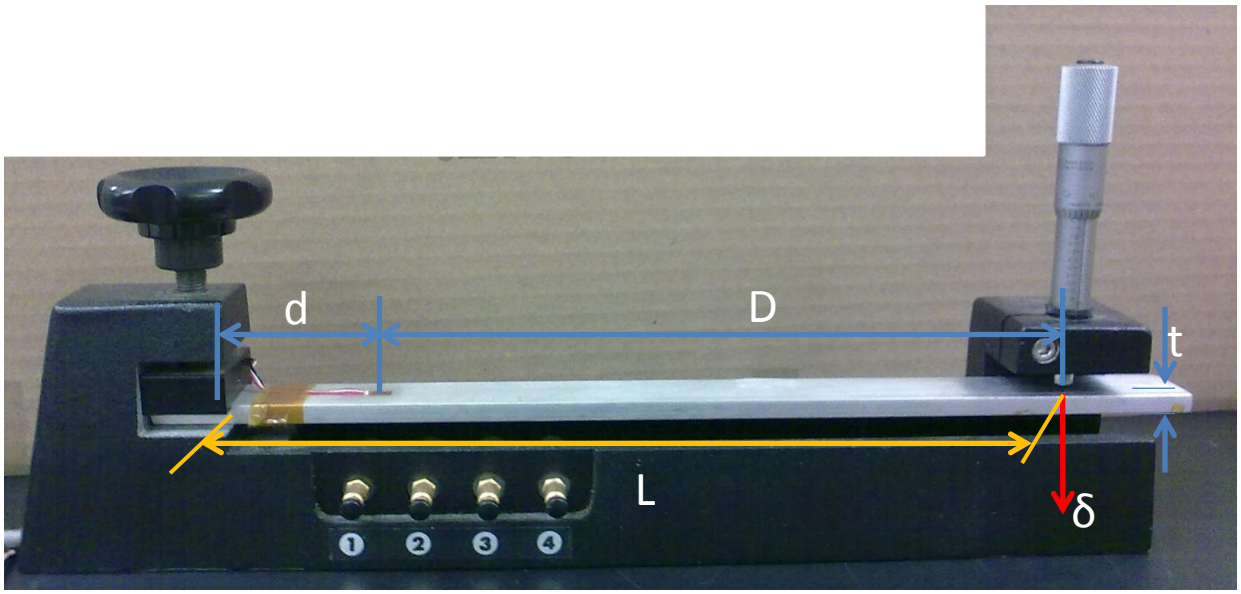

Figure 11. Strain Gage Calibration: Cantilever Beam Surface Strain Testing Setup

Table 1. Strain Gage Calibration:
Surface Strain Theoretical and Experimental Comparison Results (D = 8.25 inch)

D = 8.25 inch				
N (increment of 0.025 inch)	δ (inch)	ε_x ($\mu\varepsilon$)(Theoretical)	ε_x ($\mu\varepsilon$)(Experimental)	%Error
1	0.025	77	79	2.9
2	0.050	153	157	2.3
3	0.075	230	236	2.5
4	0.100	307	314	2.3
5	0.125	384	393	2.4
6	0.150	460	471	2.3
7	0.175	537	547	1.8
8	0.200	614	626	1.9
9	0.225	691	704	1.9

Table 2. Strain Gage Calibration:
Surface Strain Theoretical and Experimental Comparison Results (D = 7.5 inch)

D = 7.5 inch				
N (increment of 0.025 inch)	δ (inch)	ε_x ($\mu\varepsilon$)(Theoretical)	ε_x ($\mu\varepsilon$)(Experimental)	%Error
1	0.025	70	72	3.1
2	0.050	140	143	2.4
3	0.075	209	214	2.2
4	0.100	279	285	2.1
5	0.125	349	356	2.0
6	0.150	419	426	1.8
7	0.175	488	496	1.6
8	0.200	558	567	1.6
9	0.225	628	637	1.5

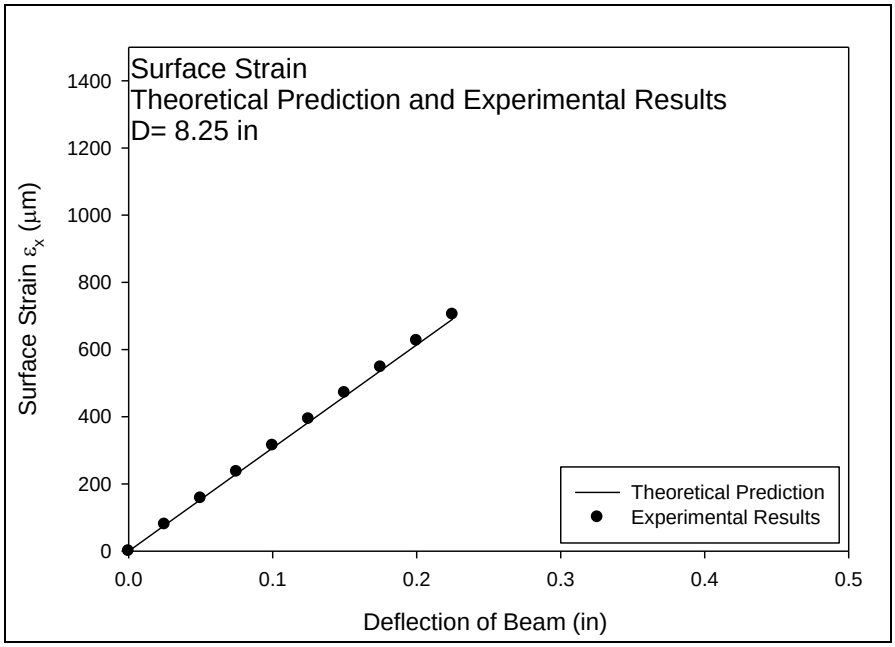

Figure 12. Surface Strain: Theoretical Prediction and Experimental Results (D = 8.25 in)

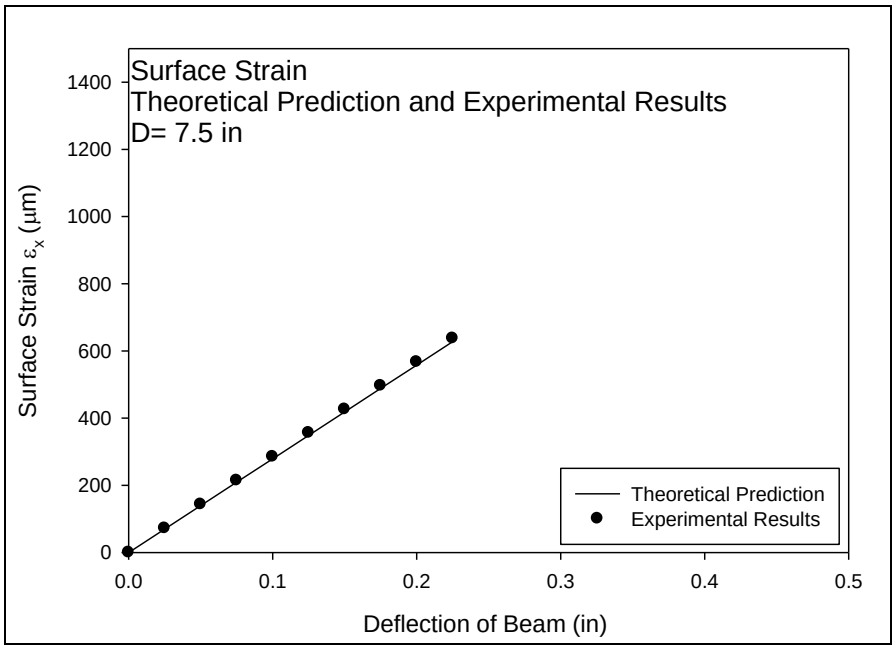

Figure 13. Surface Strain: Theoretical Prediction and Experimental Results (D = 7.5 in)

IV. MEASUREMENT OF COEFFICIENTS OF THERMAL EXPANSION

Introduction

In this chapter, experimental measurements of the thermal expansion coefficients α_1 and α_2 along the first and second principal directions of several different single-ply carbon fiber reinforced layers are presented. These results will be used in modeling of the material properties of the carbon fiber reinforced printed circuit boards later in this thesis. The CTEs for the two principal directions were measured by strain gages. Two sets of samples were prepared for each ply material and three tests were performed for each sample. The same testing procedure was used for all of the different carbon fiber ply materials tested.

The carbon fiber ply materials tested in this study were STABLCOR carbon fiber reinforced epoxy laminates layers that were specially designed to implement in high-end printed circuit boards. The STABLCOR laminates offer higher stiffness properties and better heat conduction than traditional FR-4 glass-epoxy materials. Moreover, STABLCOR laminates also have better strength to weight ratios, which make them attractive for high performance applications.

Description of Specimens and Environment Conditions

In this study, 18 different kinds of STABLCOR carbon-fiber epoxy ply materials were evaluated. The basic material designations and thicknesses are listed in Table 3. The copper weight column in the table describes the amount of copper plating on the specimen. In this category, “NONE” corresponds to no copper plating layer, “H/H” corresponds to a half ounce

Table 3. STABLCOR Layer Material Table

Sample No.	Material Description	Product Category	Copper Weight	Core Thickness
1	ST10F-0.005	ST10	NONE	0.005" (0.127mm)
2	ST10F-0.006	ST10	NONE	0.006" (0.152mm)
3	ST10P-0.006	ST10	NONE	0.006" (0.152mm)
4	ST10F-0.006 H/H	ST10	1/2 oz over 1/2 oz	0.006" (0.152mm)
5	ST10F-0.006 1/1	ST10	1 oz over 1 oz	0.006" (0.152mm)
6	ST10P-0.006 H/H	ST10	1/2 oz over 1/2 oz	0.006" (0.152mm)
7	ST10F-0.008	ST10	NONE	0.008" (0.203mm)
8	ST10P-0.008	ST10	NONE	0.008" (0.203mm)
9	ST10F-0.008 H/H	ST10	1/2 oz over 1/2 oz	0.008" (0.203mm)
10	ST10P-0.008 H/H	ST10	1/2 oz over 1/2 oz	0.008" (0.203mm)
11	ST10F-0.008 1/1	ST10	1 oz over 1 oz	0.008" (0.203mm)
12	ST325P-180	ST325	NONE	0.007" (0.180mm)
13	ST325P-180 H/H	ST325	1/2 oz over 1/2 oz	0.007" (0.180mm)
14	ST325P-0.008	ST325	NONE	0.008" (0.203mm)
15	ST325P-0.008 H/H	ST325	1/2 oz over 1/2 oz	0.008" (0.203mm)
16	ST325P-0.010	ST325	NONE	0.010" (0.255mm)
17	ST325P-0.010 H/H	ST325	1/2 oz over 1/2 oz	0.010" (0.255mm)
18	ST325P-0.010 1/1	ST325	1 oz over 1 oz	0.009" (0.240mm)

copper per square foot plating layer on both sides, and "1/1" corresponds to a one ounce per square foot copper plating layer on both sides. The CTE specimens consisted of 1" x 1" square samples cut along the first and second principal material directions. Two strain gages were mounted on each of the test specimens, with one strain gage aligned along each principal material direction. All tests were conducted in a Delta Design 9028 temperature controlled chamber (Figure 14), which was controlled by a LabView based data acquisition program. The temperature controlled chamber heats by hot air and cools with liquid nitrogen. The tests were run from T = 30 ^{o}C to T = 140 ^{o}C, with measurements made on 10 ^{o}C increments.

Experiment Setup and Calibration

All strain gage readings were processed in real time by a Wheatstone Bridge based Vishay Measurement Group 2120 strain indicator with a model MG2000 Analog to Digital Converter (Figure 15). This system allowed the Wheatstone Bridge voltage signals from the strain gages to be conditioned and transformed into digital readings. A LabView program recorded both the temperature and strain gage readings. The testing equipment has the ability to track and record 8 channels simultaneously. The excitation voltages on all channels were calibrated with a HP 3478A digital multimeter with errors not larger than ±0.001 VDC.

Initial testing for system calibration purposes was performed with copper and aluminum samples with known CTEs. The well established procedure for strain gage based CTE measurement requires strain gages to be mounted on both the specimen material of interest and a reference material of known CTE. Both materials are then subjected to controlled

temperature change. Due to thermally induced strain gage errors, the strain gage readings must be processed to extract the correct CTE values using the following expression [22]:

$$(\varepsilon_S)_{APP} - (\varepsilon_R)_{APP} = (\alpha_S - \alpha_R)T - (\alpha_S - \alpha_R)T_0 \qquad (50)$$

where α_R is the CTE of a known reference material, α_S is the unknown CTE of the test specimen, $(\varepsilon_S)_{APP}$ is the thermal output (apparent strain) of the specimen strain gage, $(\varepsilon_R)_{APP}$ is the thermal output (apparent strain) of the reference material strain gage, T is the testing temperature, and T_0 is the initial (zero strain) temperature (normally room temperature). Equation (56) can be rewritten in compact form as

$$\alpha_S = \frac{(\varepsilon_S)_{APP} - (\varepsilon_R)_{APP}}{\Delta T} + \alpha_R \qquad (51)$$

where $\Delta T = T - T_\circ$ is the temperature change from the initial reference temperature.

The reference material is a critical element of the CTE experiments. In this work, the reference material was titanium silicate from Corning Glass Company. This material has an extremely low thermal expansion coefficient that has been well characterized over a wide temperature range. Vishay WK series strain gages were used in all of the CTE tests, and Vishay M-Bond 610 adhesive was used to mount them to the specimen and reference materials. The tests were performed with an initial temperature of 30 ^{o}C with temperature steps of 10 ^{o}C up to a maximum temperature of 140 ^{o}C. At each measurement temperature, the materials were allowed to stabilize for 20 minutes before readings were taken. Sample data for copper and aluminum test specimens are shown in Figure 16. Graphs of the copper and aluminum CTE data are shown in Figures 17 and 18. From the testing results, the average CTEs in Figure 16

were 24.15 ppm/^{o}C for the aluminum specimen and 17.99 ppm/^{o}C for the copper specimen. These values agree well with standard handbook values for these materials.

Experimental Procedure and Results

The coefficients of thermal expansion of the 18 different STABLCOR ply material types were evaluated using the procedure outlined in the previous pages. Specimens were placed at the center of the temperature controlled chamber with free unconstrainted edges as shown in Figure 19.

Two samples were prepared for each STABLCOR material and each sample was tested 3 times. Example thermal strain vs. temperature raw data for the various materials are shown in Figures 20-37. All of the graphs show an extremely linear dependence of the thermal strain with temperature. The CTE values were calculated using eq. (57) and the procedure outlined in Figure 16. Tabulated results for the CTE values of the STABLCOR ply materials are listed in Table 4.

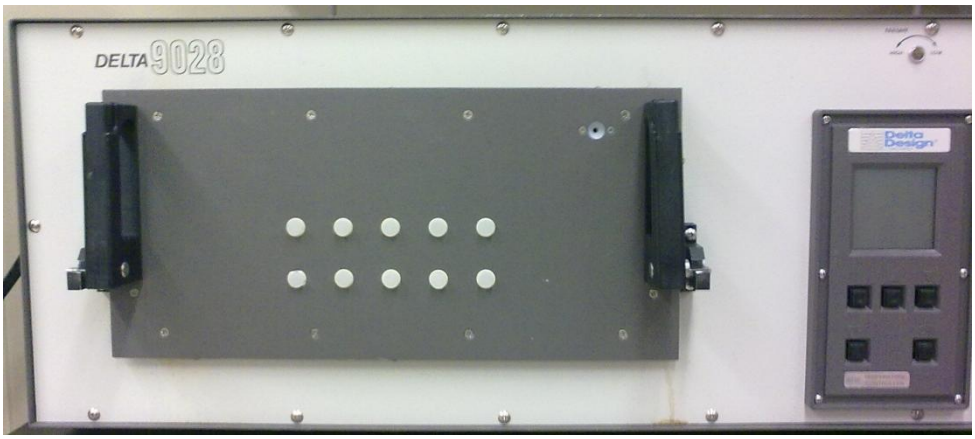

Figure 14. Environmental Chamber (Delta Design 9028)

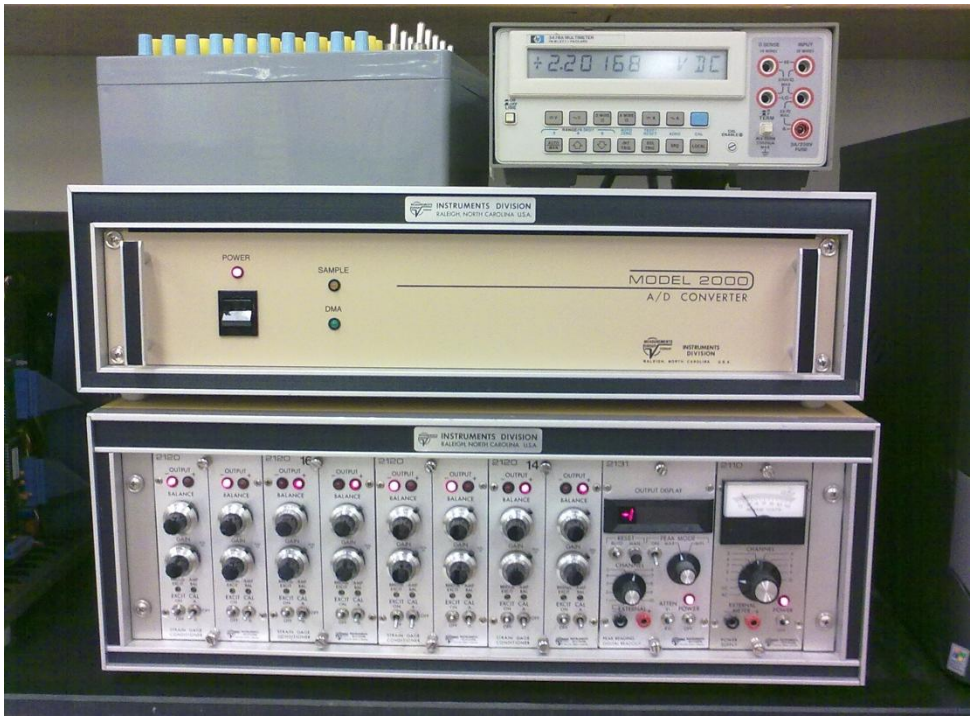

Figure 15. Vishay Strain Gage Signal Processing Equipment

Sample CTE Measurement Calculations							
Temp T	Delta T ΔT	Cu Specimen Strain Gage Reading $\varepsilon_{T/O(G/S)}$	Al Specimen Strain Gage Reading $\varepsilon_{T/O(G/S)}$	Reference Material Strain Gage Reading $\varepsilon_{T/O(G/R)}$	Cu Corrected Strain Gage Reading ε_{CORR}	Al Corrected Strain Gage Reading ε_{CORR}	Reference Material CTE α_R
30	0	-12.23	-26.046	-7.012	-5.218	-19.034	-0.9
40	10	-80.419	-30.403	-264.628	184.209	234.225	-1
50	20	-146.243	-44.726	-502.243	356	457.517	-0.9
60	30	-226.732	-57.747	-753.401	526.669	695.654	-0.8
70	40	-304.497	-70.193	-1007.193	702.696	937	-0.6
80	50	-380.195	-86.474	-1246.644	866.449	1160.17	-0.4
90	60	-456.962	-90.03	-1499.475	1042.513	1409.445	0.2
100	70	-537.105	-96.911	-1753.868	1216.763	1656.957	0.7
110	80	-590.618	-100.691	-2004.518	1413.9	1903.827	1.3
120	90	-667.052	-93.234	-2250.703	1583.651	2157.469	1.8
130	100	-726.143	-79.638	-2491.652	1765.509	2412.014	2.4
140	110	-775.287	-62.226	-2729.746	1954.459	2667.52	3.1
Sum	660	-4903.483	-838.319	-16511.083			
					Cu	Al	Avg CTE
				CTE	α_S 17.99	α_S 24.15	α_R 0.408

$$\alpha_S = \frac{(\varepsilon_{T/O(G/S)} - \varepsilon_{T/O(G/R)})}{\Delta T} + \alpha_R$$

$\varepsilon_{T/O(G/S)}$: Thermal output (apparent strain) of gage on specimen material

$\varepsilon_{T/O(G/R)}$: Thermal output (apparent strain) of gage on reference material

ΔT : Temperature change from initial reference temperature of 30 °C

α_S : CTE of specimen material

α_R : CTE of reference material

ε_{CORR} :Corrected Thermal Induced Strain

Figure 16. Sample of CTE Measurement Calculations

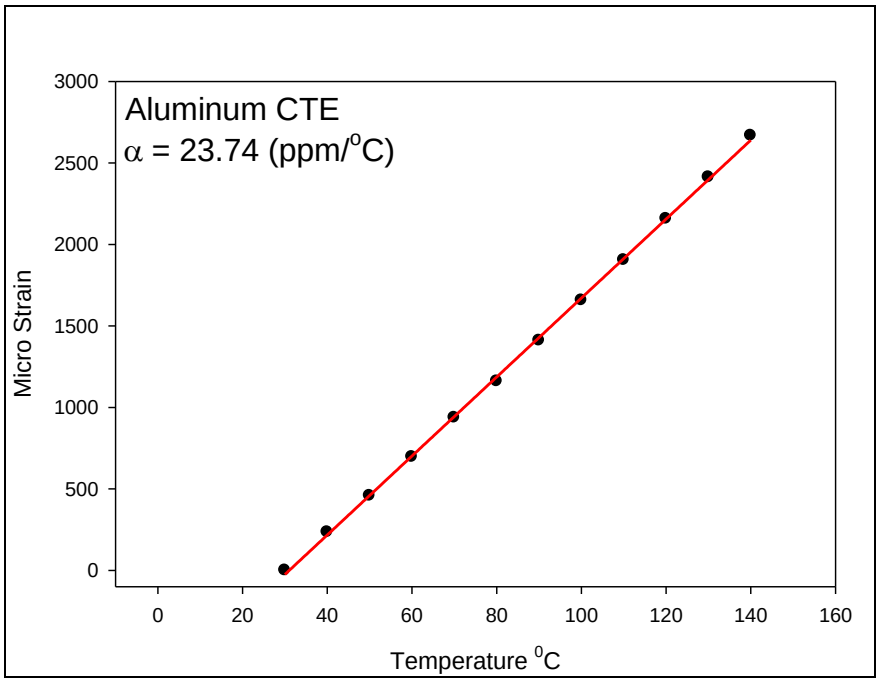

Figure 17. Testing Results for Aluminum CTE

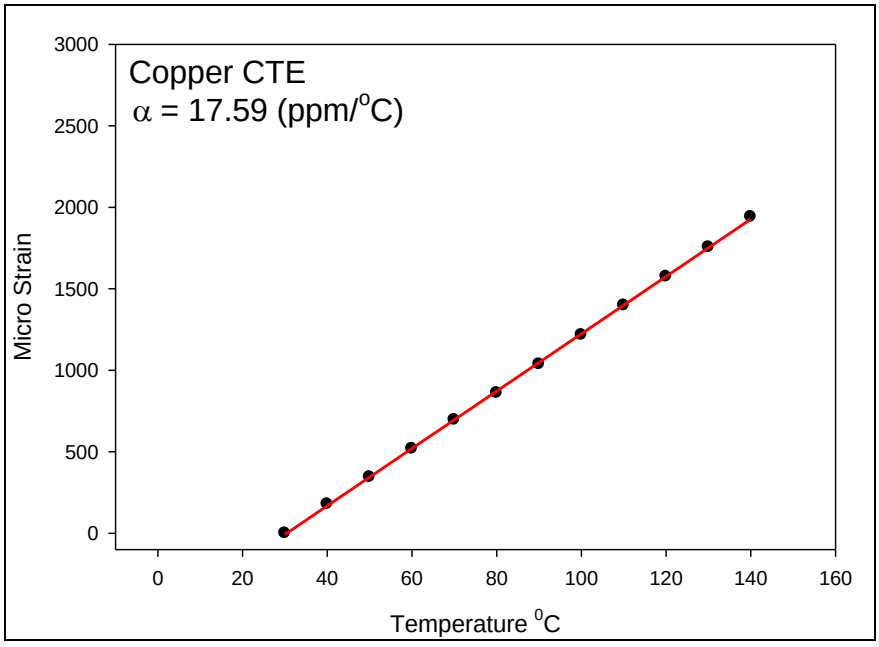

Figure 18. Testing Results for Copper CTE

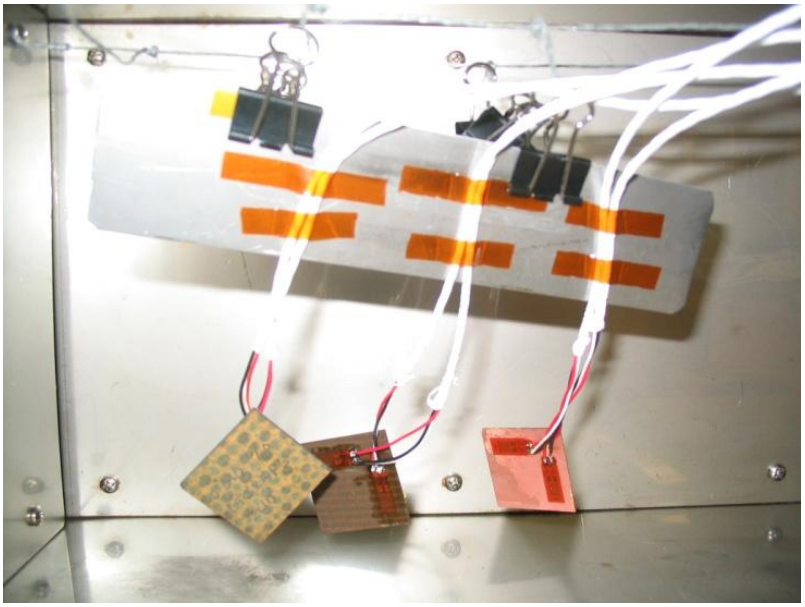

Figure 19. CTE Testing Specimens in Temperature Controlled Chamber

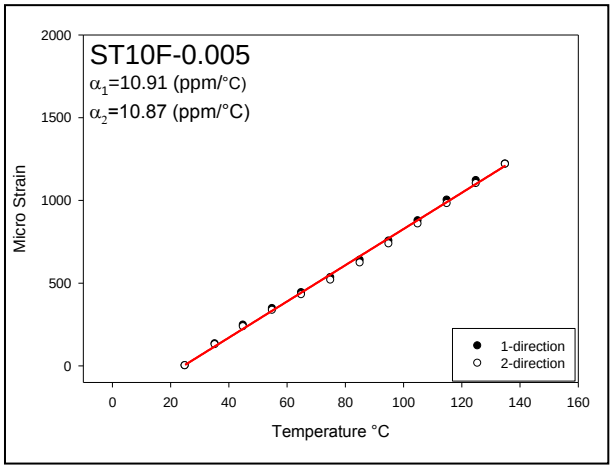

Figure 20. ST10F-0.005 Thermal Strain versus Temperature

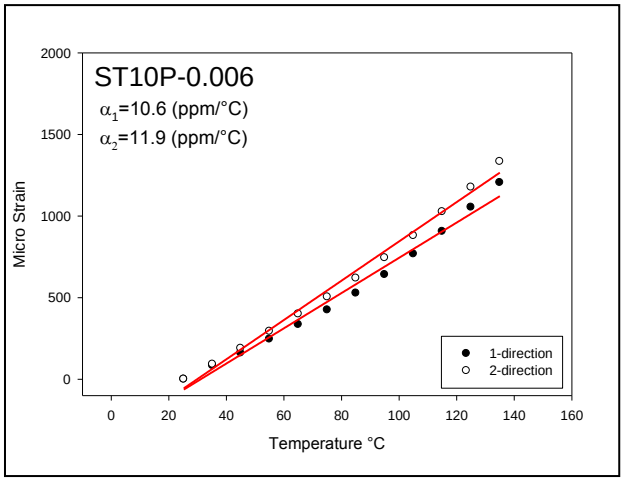

Figure 21. ST10P-0.006 Thermal Strain versus Temperature

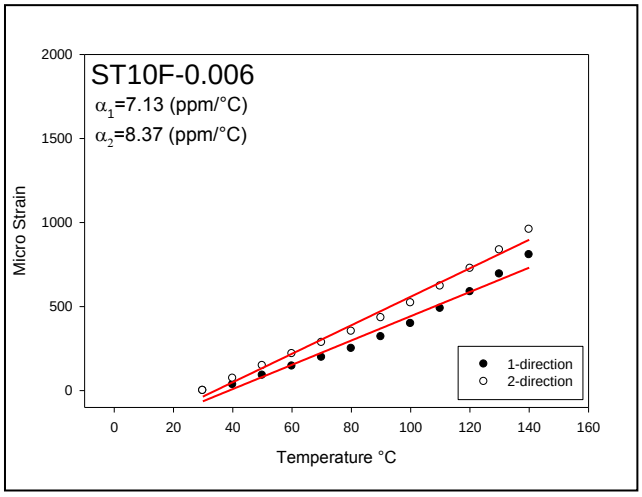

Figure 22. ST10F-0.006 Thermal Strain versus Temperature

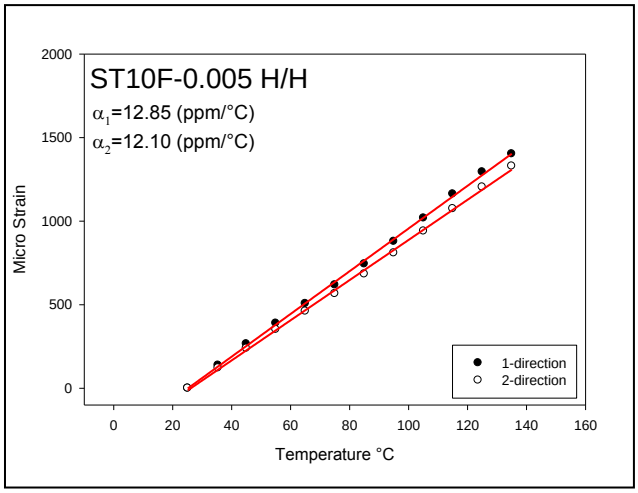

Figure 23. ST10F-0.005 H/H Thermal Strain versus Temperature

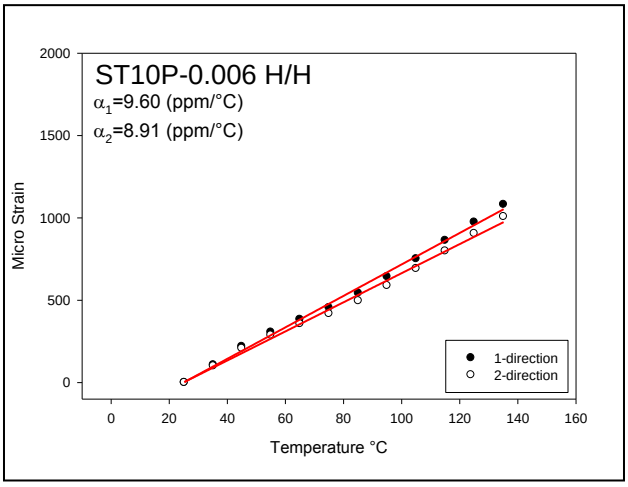

Figure 24. ST10P-0.006 H/H Thermal Strain versus Temperature

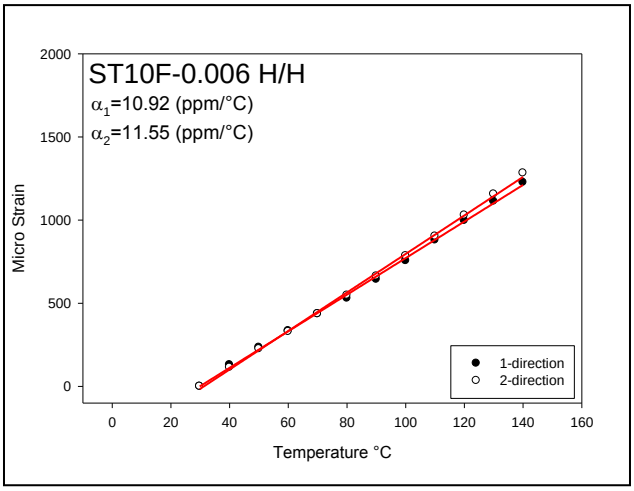

Figure 25. ST10F-0.006 H/H Thermal Strain versus Temperature

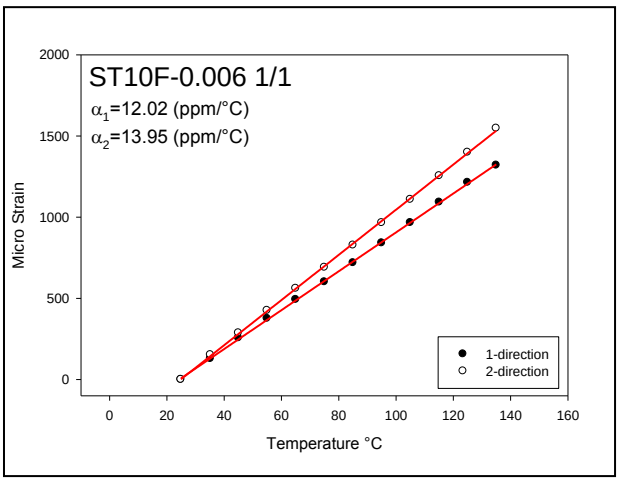

Figure 26. ST10F-0.006 1/1 Thermal Strain versus Temperature

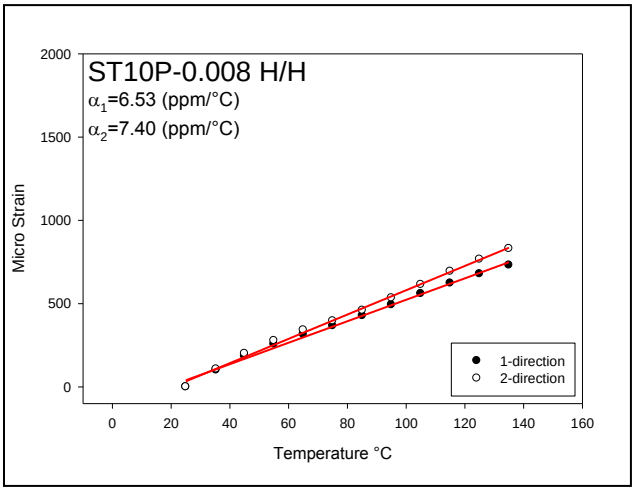

Figure 27. ST10P-0.008 H/H Thermal Strain versus Temperature

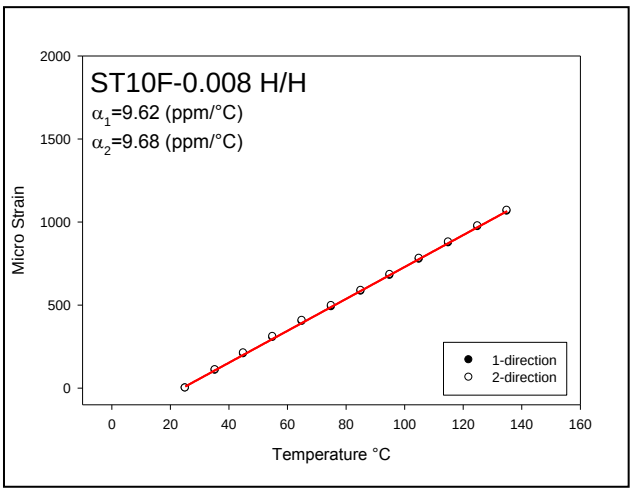

Figure 28. ST10F-0.008 H/H Thermal Strain versus Temperature

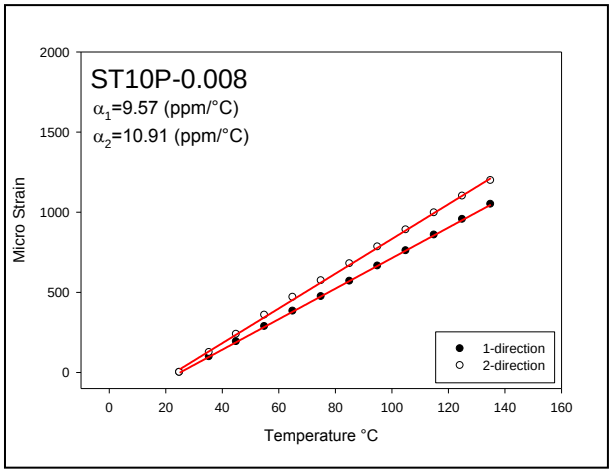

Figure 29. ST10P-0.008 Thermal Strain versus Temperature

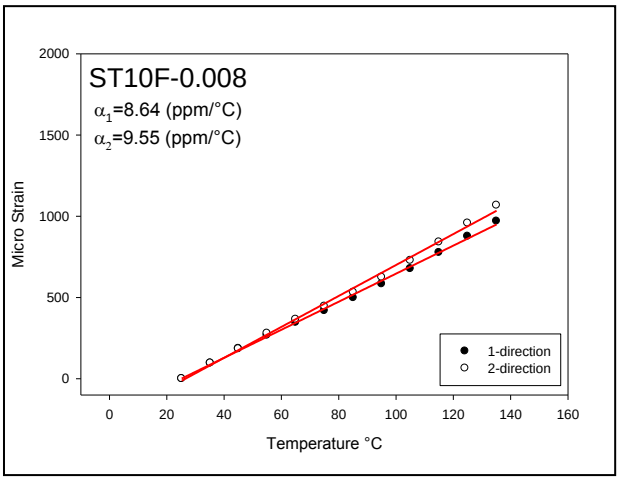

Figure 30. ST10F-0.008 Thermal Strain versus Temperature

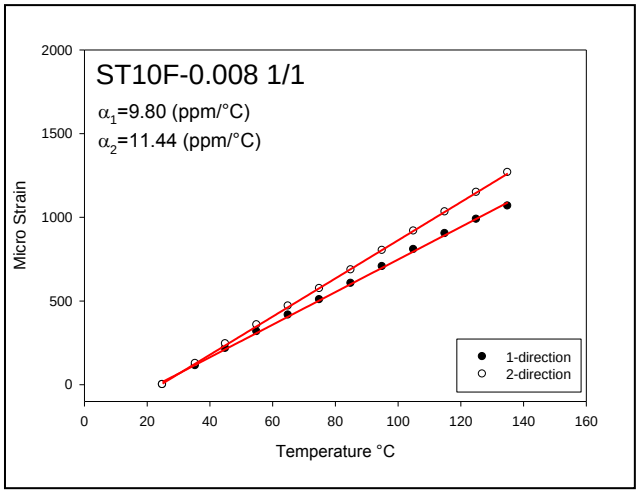

Figure 31. ST10F-0.008 1/1 Thermal Strain versus Temperature

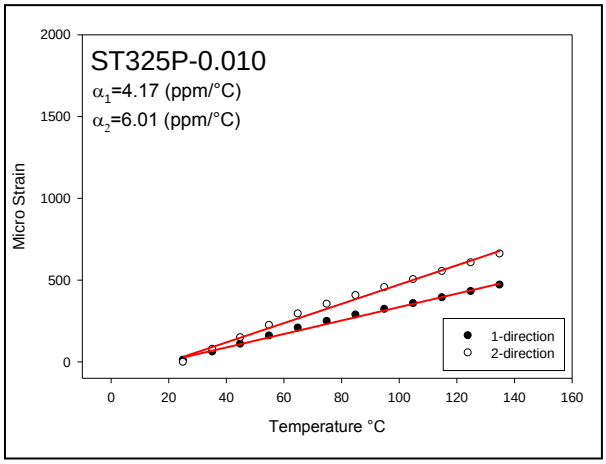

Figure 32. ST325P-0.010 Thermal Strain versus Temperature

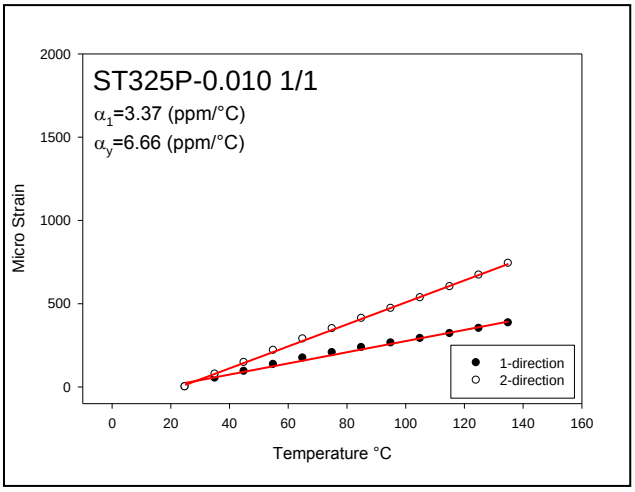

Figure 33. ST325P-0.010 1/1 Thermal Strain versus Temperature

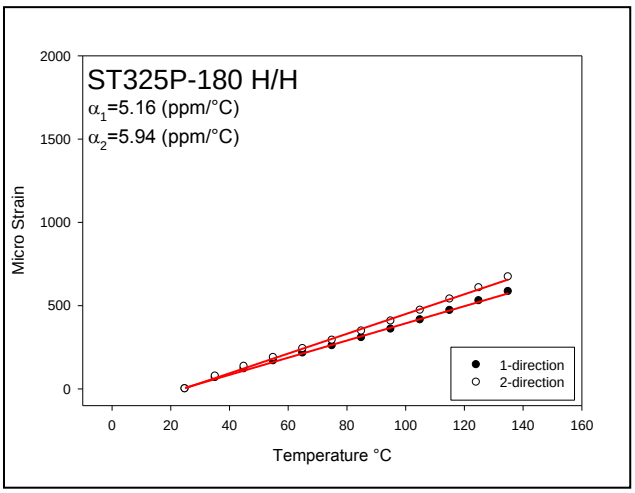

Figure 34. ST325P-180 H/H Thermal Strain versus Temperature

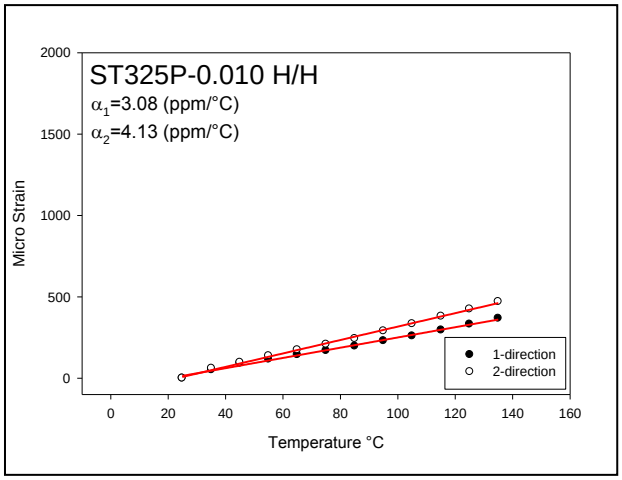

Figure 35. ST325P-0.010 H/H Thermal Strain versus Temperature

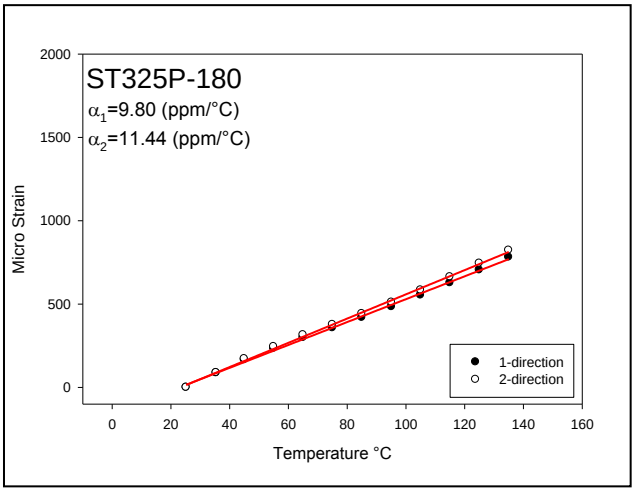

Figure 36. ST325P-180 Thermal Strain versus Temperature

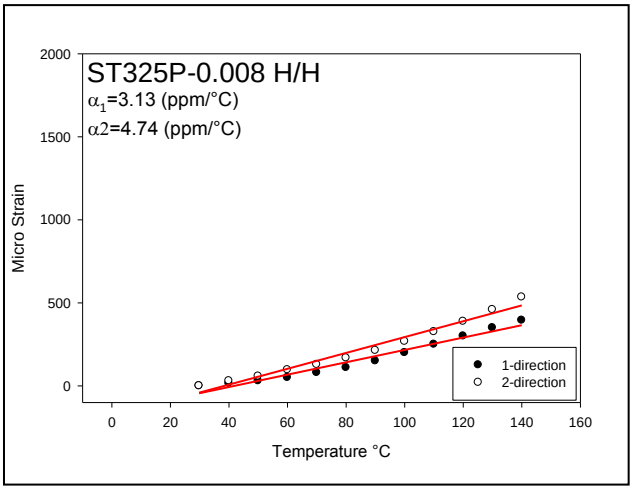

Figure 37. ST325P-0.008 H/H Thermal Strain versus Temperature

Table 4. Coefficients of Thermal Expansion for STABLCOR Ply Materials

Sample No.	Material Description	α_1 CTE (ppm/ ^{o}C) Avg (Standard dev)	α_2 CTE (ppm/ ^{o}C) Avg (Standard dev)
1	ST10F-0.005	10.79 (0.27)	10.87 (0.28)
2	ST10F-0.006	7.22 (0.37)	8.15 (0.34)
3	ST10P-0.006	10.22 (0.33)	11.97 (0.32)
4	ST10F-0.006 H/H	11.05 (0.26)	11.55 (0.23)
5	ST10F-0.006 1/1	12.08 (0.26)	14.02 (0.27)
6	ST10P-0.006 H/H	9.75 (0.30)	9.05 (0.33)
7	ST10F-0.008	8.79 (0.33)	9.46 (0.34)
8	ST10P-0.008	9.58 (0.42)	11.03 (0.44)
9	ST10F-0.008 H/H	9.71 (0.28)	9.8 (0.28)
10	ST10P-0.008 H/H	6.57 (0.30)	7.33 (0.31)
11	ST10F-0.008 1/1	9.74 (0.27)	11.33 (0.38)
12	ST325P-180	6.7 (0.30)	7.07 (0.34)
13	ST325P-180 H/H	5.04 (0.29)	5.85 (0.33)
14	ST325P-0.008	4.58 (0.31)	6.17 (0.33)
15	ST325P-0.008 H/H	3.14 (0.29)	4.77 (0.30)
16	ST325P-0.010	4.1 (0.42)	6.04 (0.44)
17	ST325P-0.010 H/H	3.03 (0.26)	4.08 (0.28)
18	ST325P-0.010 1/1	3.42 (0.24)	6.71 (0.26)

V. MEASUREMENT OF ELASTIC MODULI

Introduction

Lamination theory requires input material properties for each fiber-reinforced layer including the elastic moduli E_1 and E_2 along the first and second principal material directions, the Poisson's ratios ν_{12} and ν_{21}, and the shear modulus G_{12}. In this chapter, the elastic moduli of 18 different STABLCOR carbon fiber ply materials have been measured by mechanical testing.

Description of Specimens and Testing Conditions

The uniaxial test specimens for mechanical testing were cut out from single ply samples. The nominal dimensions were 5 mm in width and 60 mm in length. Three specimens were prepared for each material in each of the principal material directions, and three tests were performed on each specimen and the results were averaged. All tests were performed at 25^{o}C with crosshead speed of 0.0006 mm/s. With the gage length of 60 mm, this resulted in a strain rate of $\dot{\varepsilon} = 1 \times 10^{-5}\,\mathrm{sec}^{-1}$. Photographs of uniaxial specimens in the mechanical testing machine are shown in Figures 38 and 39. This setup recorded both axial force and crosshead displacement, from which the axial stress and axial strain could be calculated. Ten data points were recorded per second, and the maximum load limit was set to 50 N.

To further refine the specimen strain measurements, axial strain gages were also applied to the specimens (type CEA-13-125UN-350 from Vishay). However, it was found that the gages only yielded accurate measurements for the fine weave carbon fiber specimens. For

larger weave materials, the gages were too small and picked up local mismatches in the deformations of the carbon fibers and epoxy matrix.

Results and Conclusion

Typical stress-strain curves recorded for the 18 carbon fiber ply materials are shown in Figures 40 – 79. In these results, strains were calculated using the measured crosshead displacement, and Least-Squares linear regression fits were used to fit the data points. The regression fits are shown as red lines on the graphs. The slopes of the regression lines are the elastic moduli of the specimens. The average elastic moduli for all of the ply materials are tabulated in Table 5. Table 6 compares the results of the 1-direction elastic modulus measurements obtained from strains evaluated with the crosshead displacements with modulus measurements obtained from strains found with strain gages. An example specimen with strain gages mounted is show in Figure 80. In summary, good correlation was only obtained for the two methods when the carbon fiber ply material had a very small/fine weave (samples 1 – 5). For the other specimen materials, the strain gages were too small compared to the weave and recorded local effects (e.g. only measured strains in the epoxy or in the fibers, instead of the average strains in the fiber-reinforced composite).

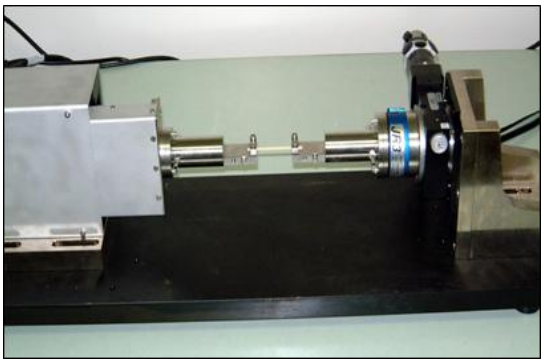

Figure 38. Uniaxial Specimen in Mechanical Testing Machine

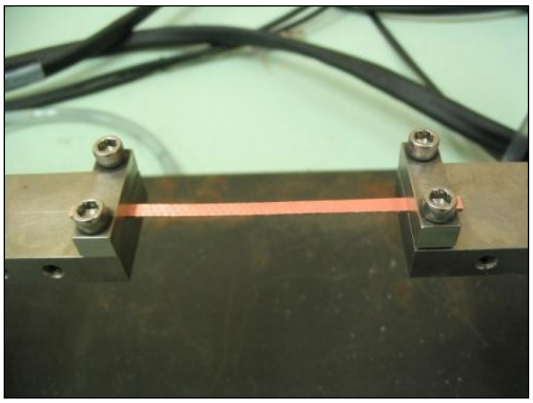

Figure 39. Close-up Photograph of Uniaxial Specimen

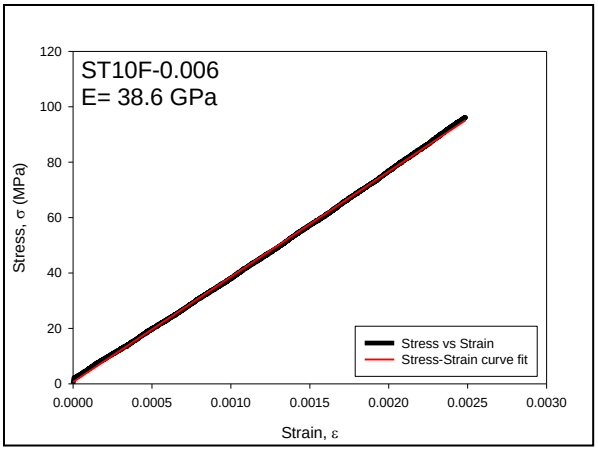

Figure 40. ST10F-0.006 Stress versus Strain (1-direction)

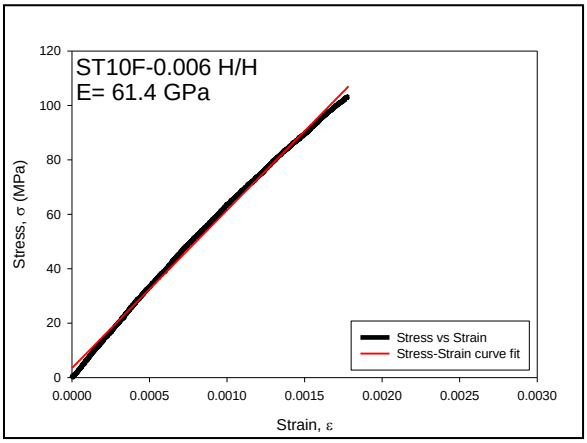

Figure 41. ST10F-0.006 H/H Stress versus Strain (1-direction)

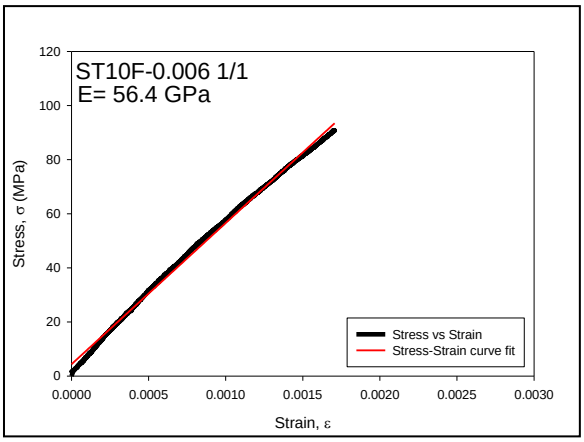

Figure 42. ST10F-0.006 1/1 Stress versus Strain (1-direction)

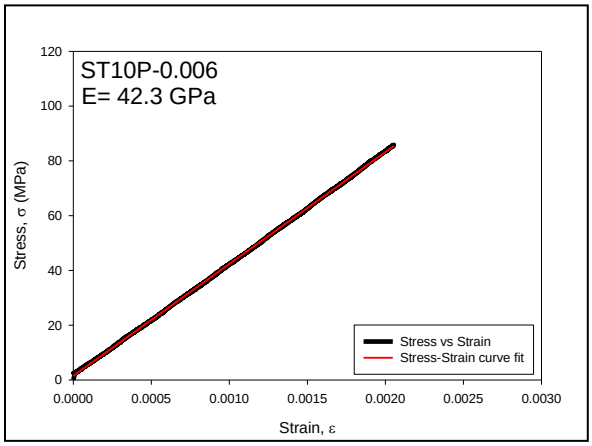

Figure 43. ST10P-0.006 Stress versus Strain (1-direction)

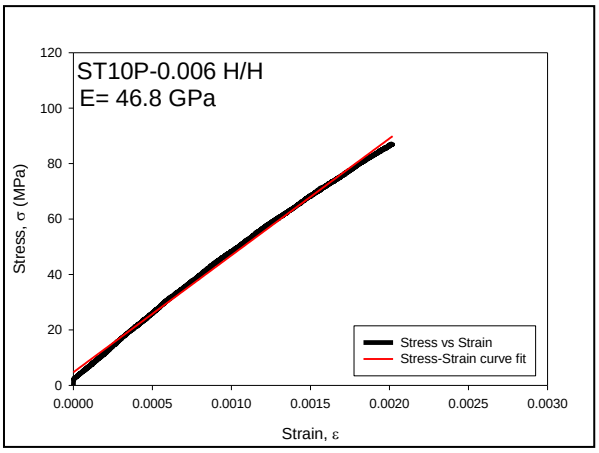

Figure 44. ST10P-0.006 H/H Stress versus Strain (1-direction)

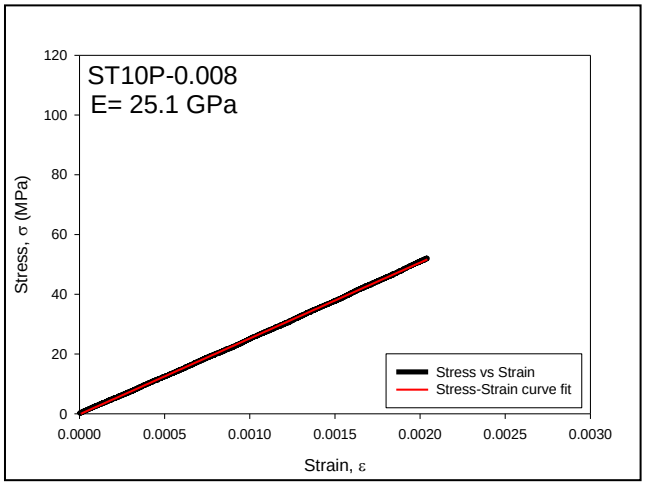

Figure 45. ST10P-0.008 Stress versus Strain (1-direction)

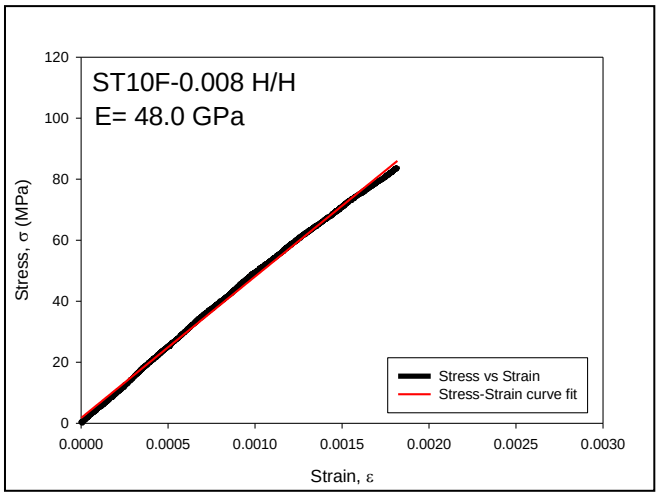

Figure 46. ST10F-0.008 H/H Stress versus Strain (1-direction)

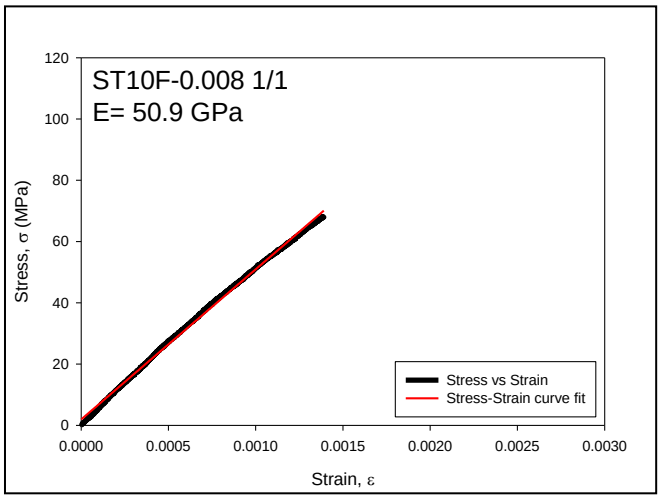

Figure 47. ST10F-0.008 1/1 Stress versus Strain (1-direction)

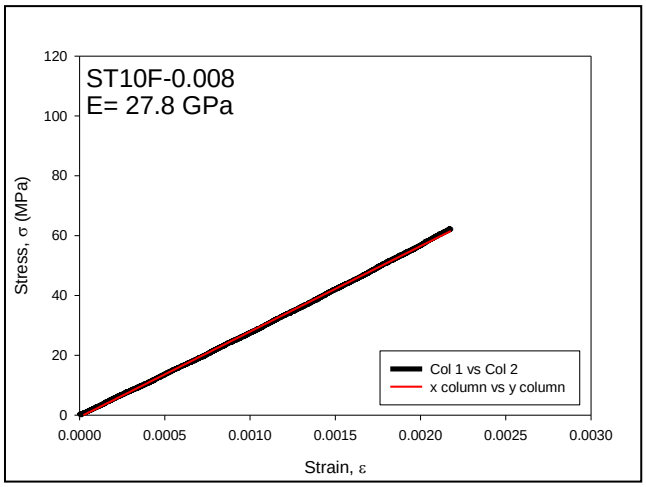

Figure 48. ST10F-0.008 Stress versus Strain (1-direction)

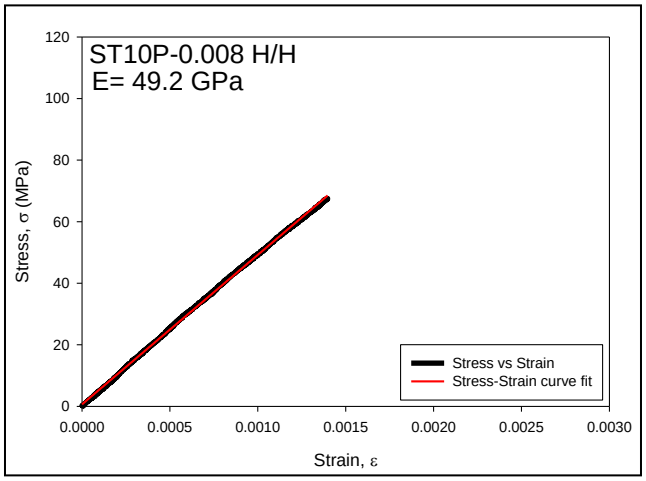

Figure 49. ST10P-0.008 H/H Stress versus Strain (1-direction)

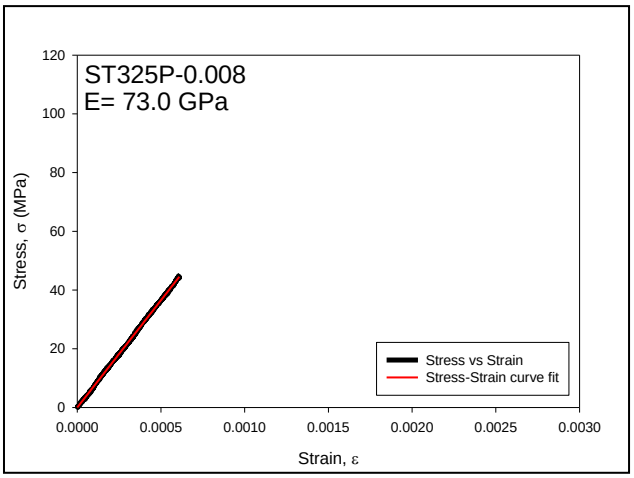

Figure 50. ST325P-0.008 Stress versus Strain (1-direction)

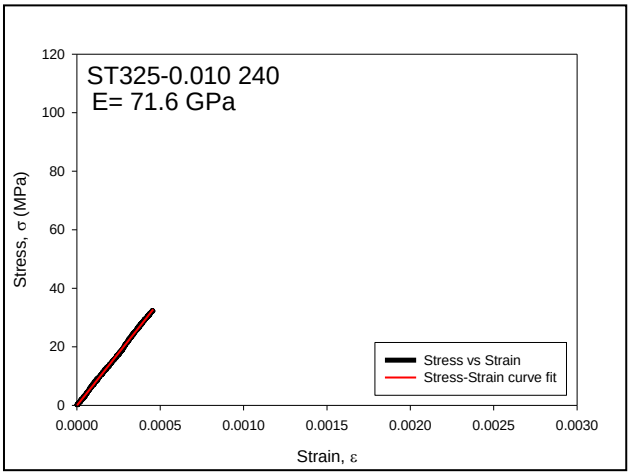

Figure 51. ST325P-0.010 240 Stress versus Strain (1-direction)

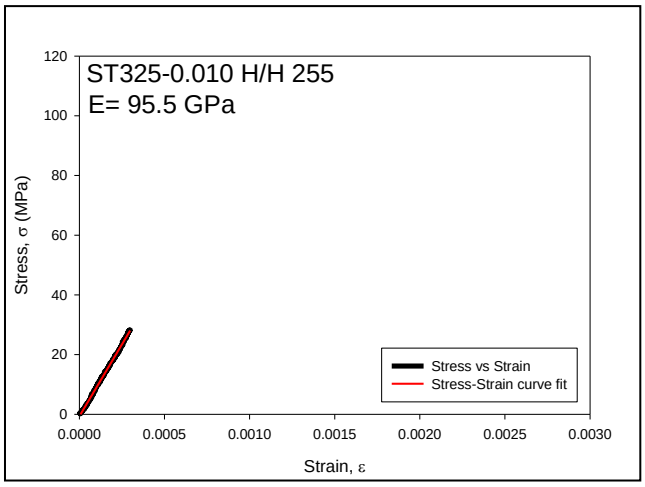

Figure 52. ST325P-0.010 H/H 255 Stress versus Strain (1-direction)

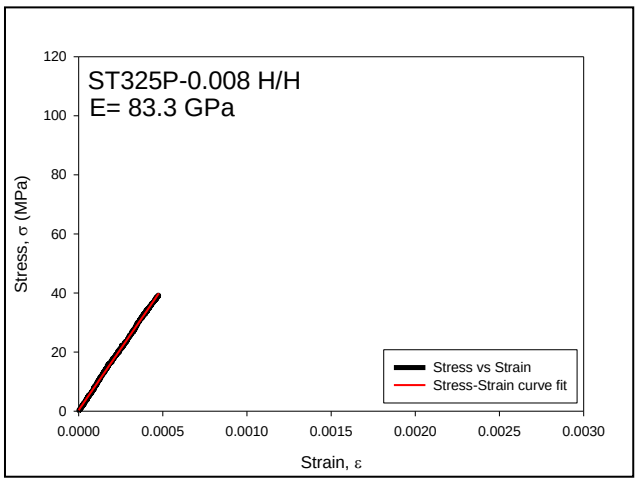

Figure 53. ST325P-0.008 H/H Stress versus Strain (1-direction)

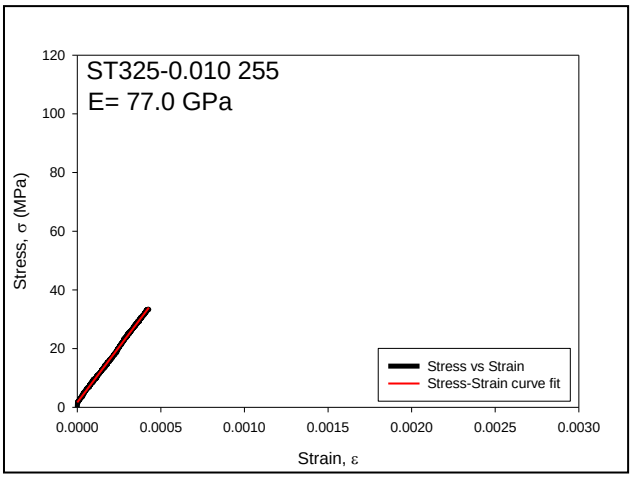

Figure 54. ST325P-0.010 255 Stress versus Strain (1-direction)

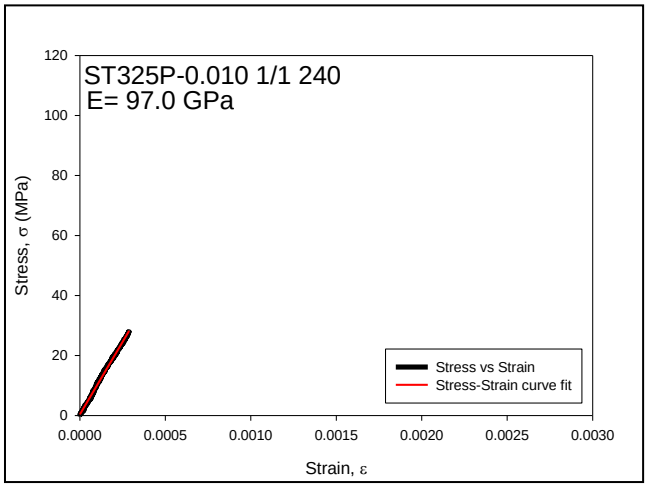

Figure 55. ST325P-0.010 1/1 240 Stress versus Strain (1-direction)

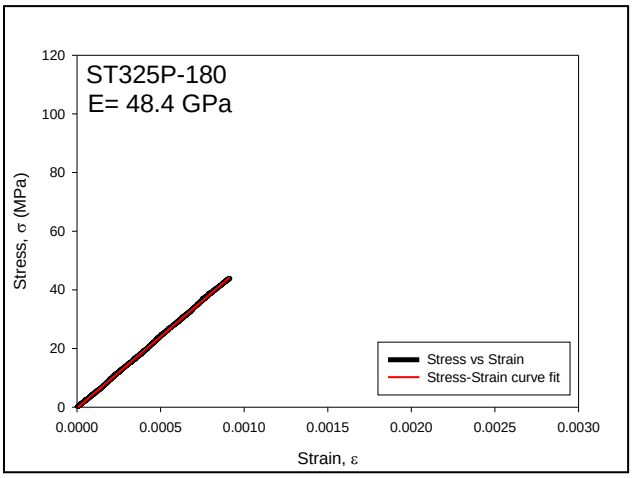

Figure 56. ST325P-180 Stress versus Strain (1-direction)

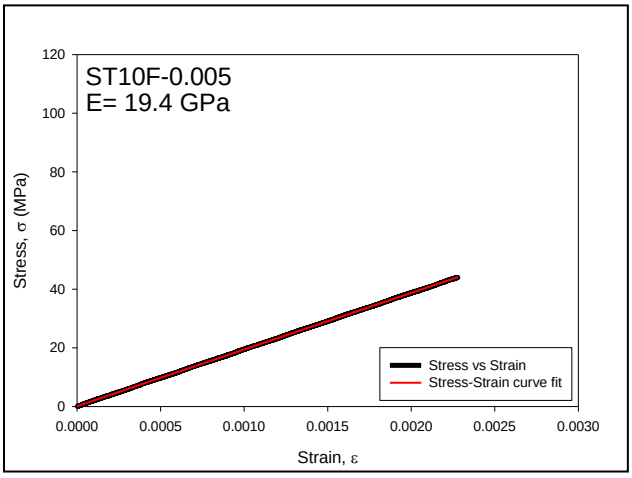

Figure 57. ST10F-0.005 Stress versus Strain (1-direction)

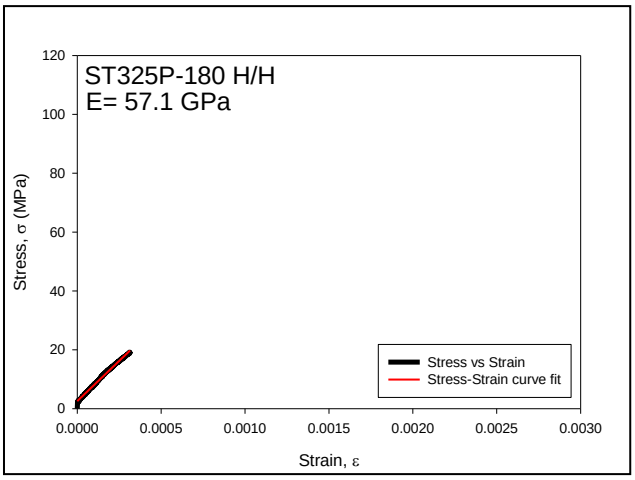

Figure 58. ST325P-180 H/H Stress versus Strain (1-direction)

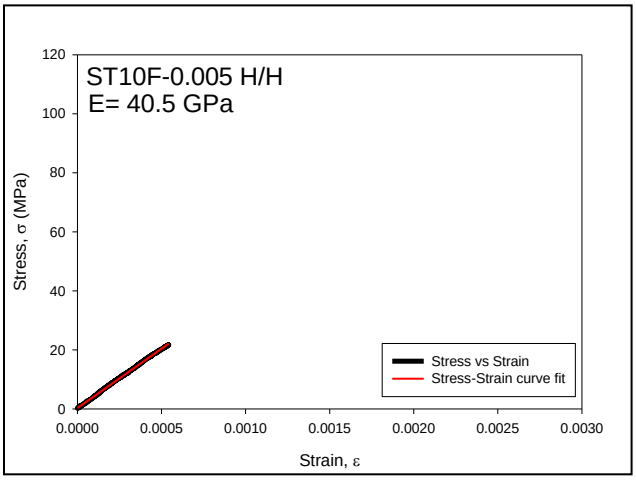

Figure 59. ST10F-0.005 H/H Stress versus Strain (1-direction)

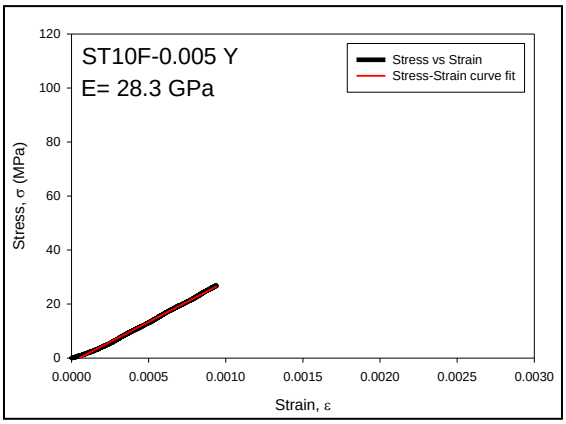

Figure 60. ST10F-0.005 H/H Stress versus Strain (2-direction)

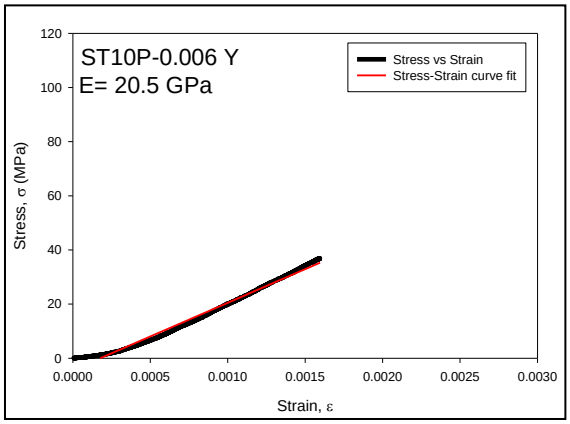

Figure 61. ST10P-0.006 Stress versus Strain (2-direction)

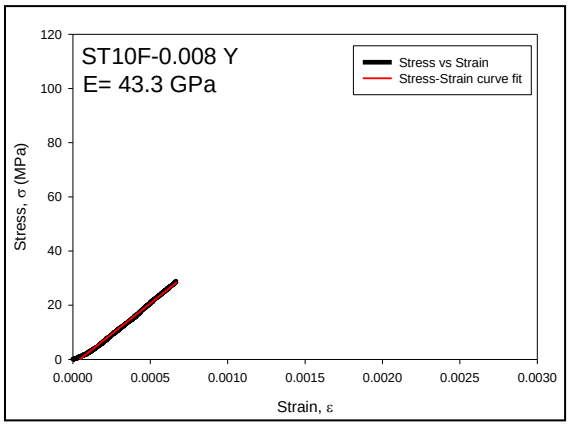

Figure 62. ST10F-0.008 Stress versus Strain (2-direction)

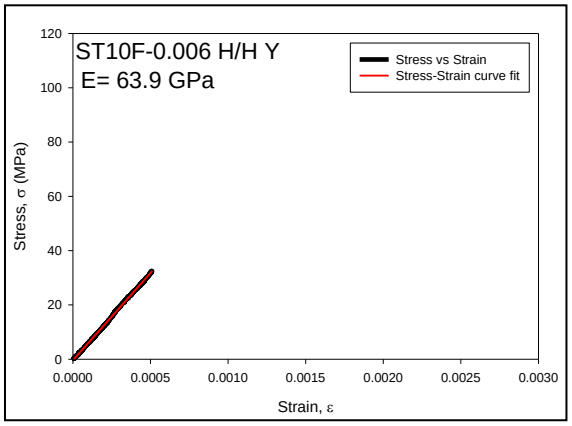

Figure 63. ST10F-0.006 H/H Stress versus Strain (2-direction)

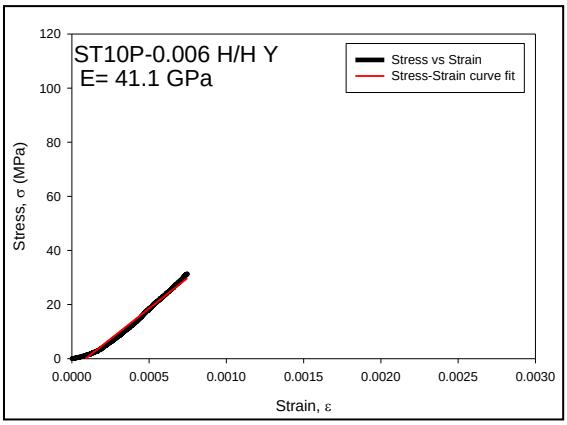

Figure 64. ST10P-0.006 H/H Stress versus Strain (2-direction)

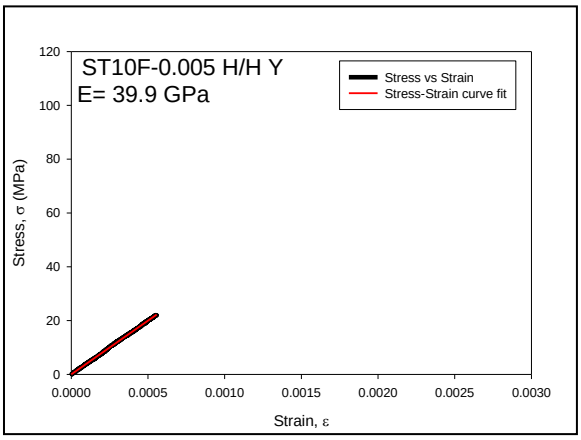

Figure 65. ST10F-0.005 H/H Stress versus Strain (2-direction)

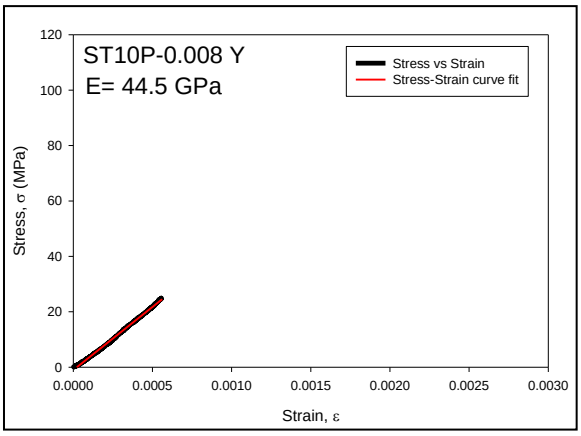

Figure 66. ST10P-0.008 Stress versus Strain (2-direction)

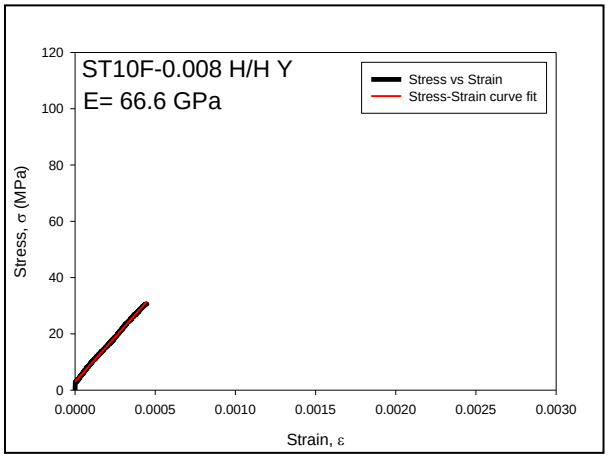

Figure 67. ST10F-0.008 H/H Stress versus Strain (2-direction)

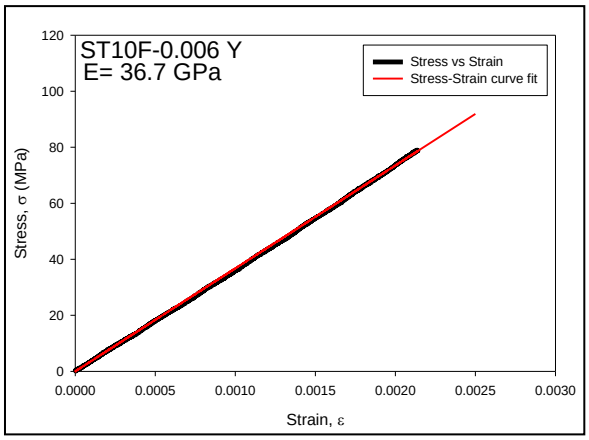

Figure 68. ST10F-0.006 Stress versus Strain (2-direction)

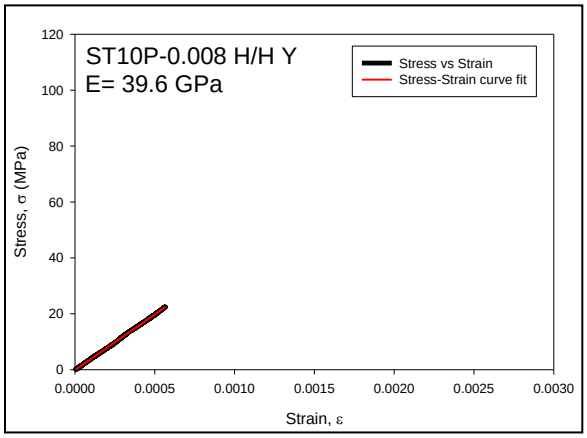

Figure 69. ST10P-0.008 H/H Stress versus Strain (2-direction)

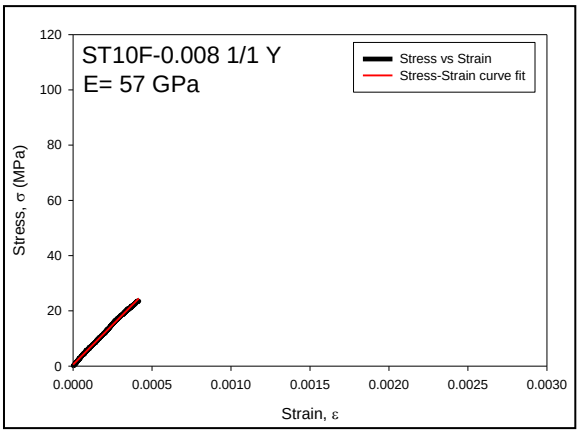

Figure 70. ST10F-0.008 1/1 Stress versus Strain (2-direction)

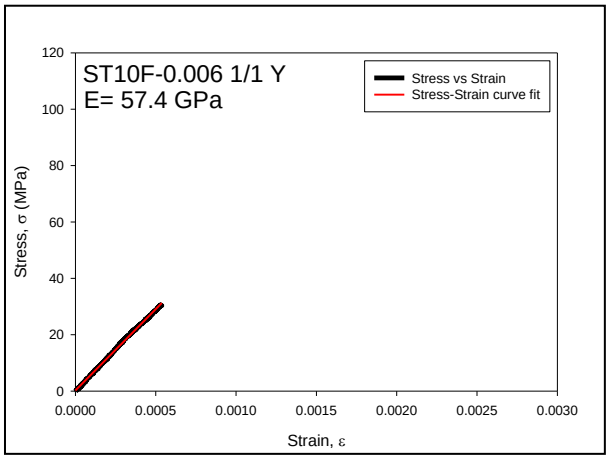

Figure 71. ST10F-0.006 1/1 Stress versus Strain (2-direction)

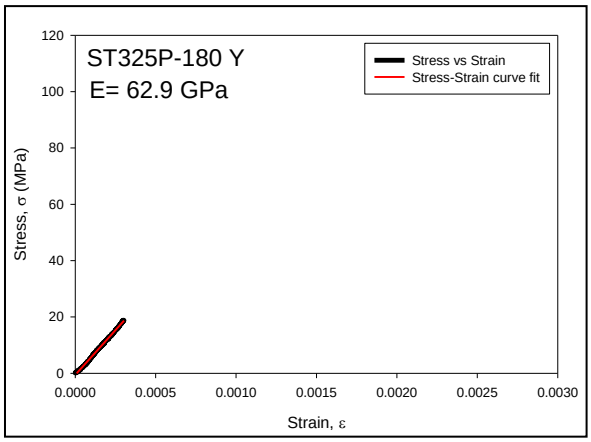

Figure 72. ST325P-180 Stress versus Strain (2-direction)

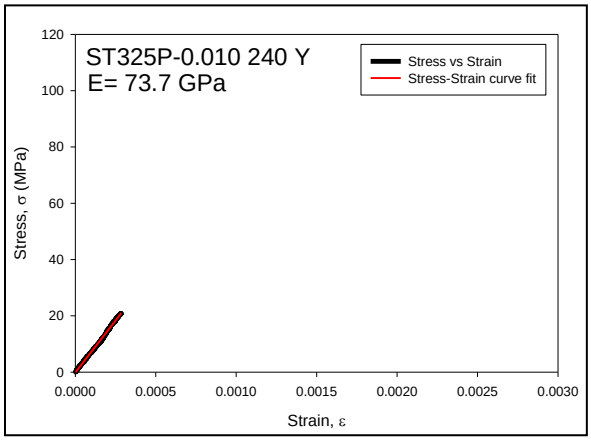

Figure 73. ST325P-0.010 240 Stress versus Strain (2-direction)

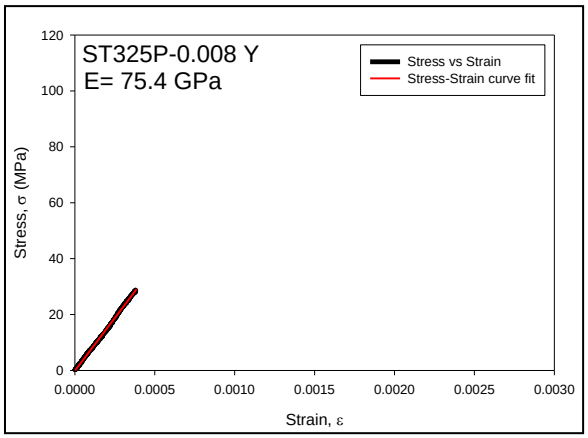

Figure 74. ST325P-0.008 Stress versus Strain (2-direction)

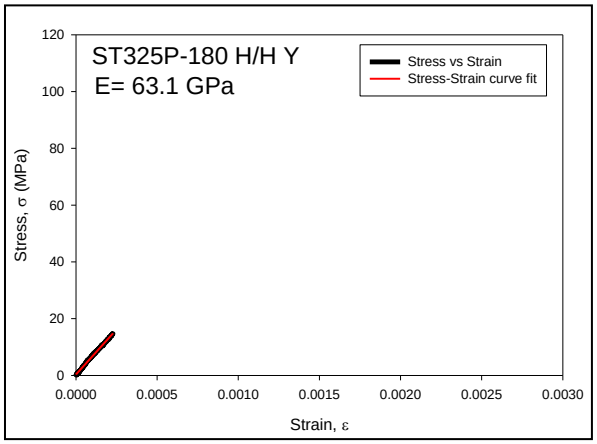

Figure 75. ST325P-180 H/H Stress versus Strain (2-direction)

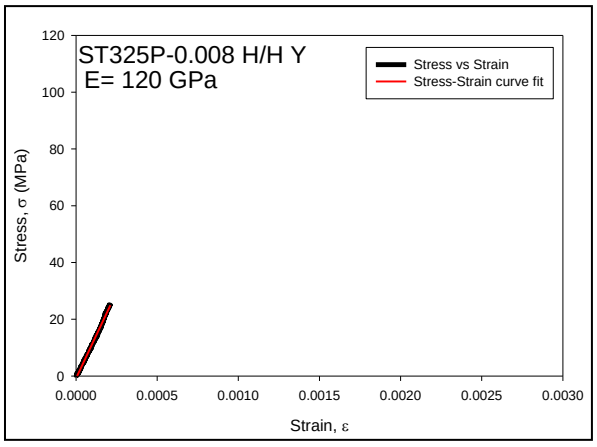

Figure 76. ST325P-0.008 H/H Stress versus Strain (2-direction)

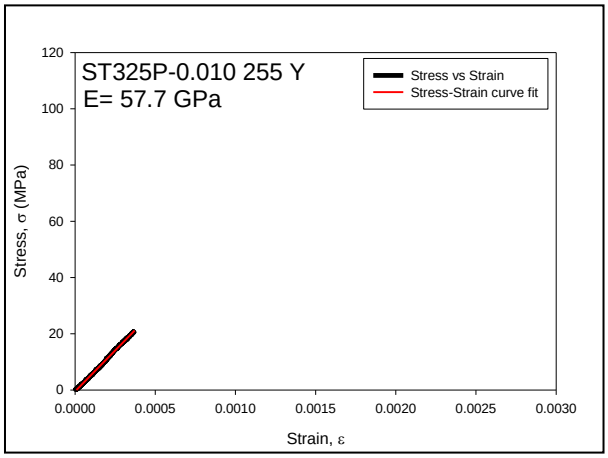

Figure 77. ST325P-0.010 255 Stress versus Strain (2-direction)

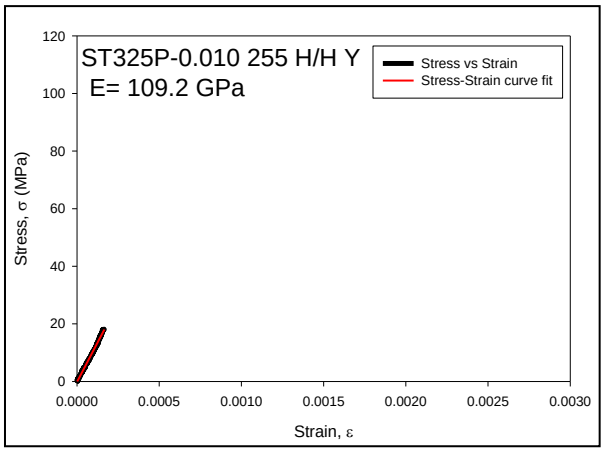

Figure 78. ST325P-0.010 255 H/H Stress versus Strain (2-direction)

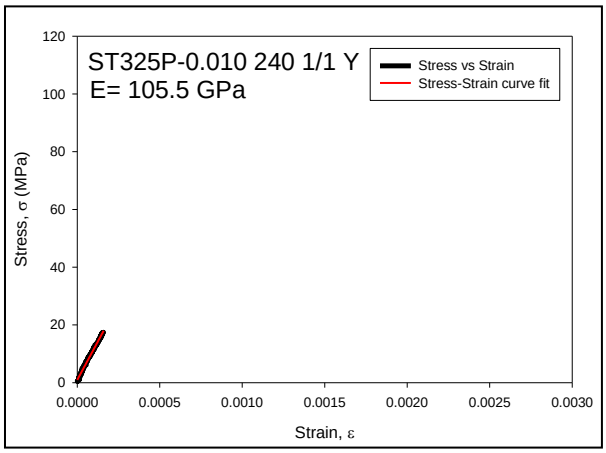

Figure 79. ST325P-0.010 240 1/1 Stress versus Strain (2-direction)

Table 5. Elastic Modulus Results Obtain by Crosshead Displacement

Sample No.	Material Description	E_1 (GPa) Avg (Standard Dev)	E_2 (GPa) Avg (Standard Dev)
1	ST10F-0.006	38.5 (0.7)	36.7 (0.5)
2	ST10P-0.006	42.0 (0.6)	20.4 (0.7)
3	ST10F-0.006 H/H	61.3 (0.7)	63.7 (0.7)
4	ST10F-0.006 1/1	56.3 (0.7)	57.2 (0.8)
5	ST10P-0.006 H/H	46.6 (0.7)	41.3 (0.9)
6	ST10F-0.008	27.7 (0.8)	43.4 (0.7)
7	ST10P-0.008	25.2 (0.5)	44.5 (0.6)
8	ST10F-0.008 H/H	48.1 (0.5)	66.4 (0.8)
9	ST10P-0.008 H/H	49.4 (0.8)	39.6 (0.7)
10	ST10F-0.008 1/1	50.8 (0.8)	57.2 (0.7)
11	ST325P-180	48.2 (0.7)	63 (0.7)
12	ST325P-180 H/H	57.1 (0.8)	63 (0.7)
13	ST325P-0.008	73.2 (0.6)	75.6 (0.6)
14	ST325P-0.008 H/H	83.5 (0.8)	120.4 (1.0)
15	ST325P-0.010 240	71.4 (0.6)	73.4 (0.6)
16	ST325P-0.010 255	77.2 (0.7)	57.6 (0.7)
17	ST325P-0.010 H/H	95.7 (1.0)	109.4 (1.1)
18	ST325P-0.010 1/1	97.2 (0.9)	105.5 (0.9)

Table 6. Elastic Modulus Measurement Comparisons for Stress Evaluated Using Crosshead Displacements and Strain Gages

Sample No.	Material Description	E_1 (GPa) From Crosshead Displacements	E_1 (GPa) From Strain Gage Measurements
1	ST10F-0.006	38.5	35.5
2	ST10P-0.006	42.0	39.6
3	ST10F-0.006 H/H	61.3	60.8
4	ST10F-0.006 1/1	56.3	63.6
5	ST10P-0.006 H/H	46.6	45.5
6	ST10F-0.008	27.7	46.6
7	ST10P-0.008	25.2	34.3
8	ST10F-0.008 H/H	48.1	63.1
9	ST10P-0.008 H/H	49.4	58.8
10	ST10F-0.008 1/1	50.8	60.8
11	ST325P-180	48.2	63.5
12	ST325P-180 H/H	57.1	72.6
13	ST325P-0.008	73.2	71.6
14	ST325P-0.008 H/H	83.5	107.2
15	ST325P-0.010 240	71.4	33.1
16	ST325P-0.010 255	77.2	49.3
17	ST325P-0.010 H/H	95.7	161.4
18	ST325P-0.010 1/1	97.2	76.5

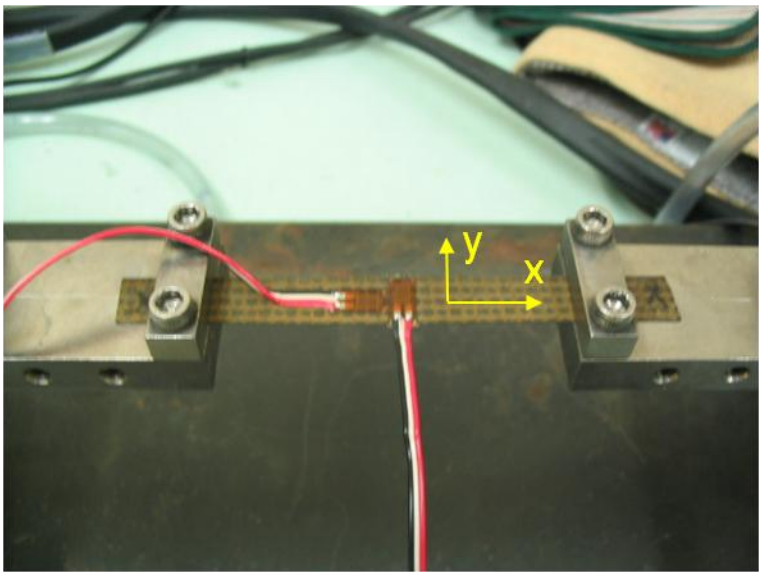

Figure 80. Example of Specimen with Mounted Strain Gages

VI. INDIRECT METHOD FOR EVALUATION OF SHEAR MODULUS AND POISSON'S RATIO

Introduction

In order to apply lamination theory, both the shear modulus G_{12} and Poisson's Ratio ν_{12} of the constituent layers must be known. However, these two material properties are very difficult to obtain directly. As discussed in the previous chapter, it was not possible to obtain accurate strain gage measurements for many of the carbon fiber ply materials because they employed fairly coarse fiber weaving. Thus, Poisson's ratios could not be found using the conventional approach where axial and transverse strains are monitored with strain gages during uniaxial testing. Thus, in this work an indirect method was employed to calculate the shear modulus G_{12} and Poisson's ratio ν_{12} from off-axis elastic modulus measurements.

The theoretical expression for the variation of the in-plane elastic modulus with angle in a fiber-reinforced orthotropic layer is [6]

$$\frac{1}{E_x(\theta)} = \frac{\cos^4\theta}{E_1} + \left[\frac{1}{G_{12}} - \frac{2\nu_{12}}{E_1}\right]\sin^2\theta\cos^2\theta + \frac{\sin^4\theta}{E_2} \qquad (52)$$

where θ is the angle from the fiber direction (see Figure 81), $E_x(\theta)$ is the off-axis elastic modulus, E_1 is the elastic modulus in the first direction of material symmetry (1-direction), E_2 is the elastic modulus in the second direction of material symmetry (2-direction), ν_{12} is the Poisson's ratio, and G_{12} is the shear modulus. Experimentally, the values of $E_x(\theta)$ can be measured for several different angles including $\theta = 0°$ (E_1) and $\theta = 90°$ (E_2). If five or more

angles are tested, an indirect procedure can then be used to calculate G_{12} and ν_{12} via nonlinear regression fitting of eq. (58) to the experimental E_x vs. θ data.

Description of Specimens and Testing Conditions

Off-axis uniaxial samples were cut with dimensions of 3 mm in width and 60 mm in length. The material sheets were first marked with off-axis guide lines and then the specimens were cut by a hand shear as shown in Figures 82-83. Seven different specimen orientations were prepared for each ply material including θ = 0°, 15°, 30°, 45°, 60°, 75°, and 90°. The elastic moduli of the off-axis testing coupons were then obtained using mechanical testing as discussed in the previous chapter. The crosshead speed was again taken to be 0.0006 mm/s, resulting in a strain rate of $\dot{\varepsilon} = 1\times10^{-5}\,\mathrm{sec}^{-1}$. All tests were conducted at 25 °C.

Results and Conclusion

Example off-axis stress-strain curves and elastic modulus data for the ST10F-0.006 H/H ply material are shown in Figures 84 – 85 (θ = 0° and 90°) and Figures 86 – 90 (θ = 15°, 30°, 45°, 60°, and 75°). The seven modulus values were regression fitted using eq. (58) to calculate G_{12} = 13.7 GPa and ν_{12} = 0.27 as shown in Figure 91. The Matlab toolbox was used to perform the regression analysis. The fit of the model to the data is excellent, and an R-Squared value of 0.994 was obtained.

Analogous measurements were made for the ST10P-0.006 material as shown in Figures 92 – 98, and the regression fit is illustrated in Figure 99. In this case, the calculated values were G_{12}= 3.59 GPa and ν_{12}= 0.21, with an R-Squared value of 0.993. Similar procedures were

followed for all 18 different STABLCOR carbon fiber ply materials. The measured G_{12} and ν_{12} data are tabulated in Table 7, and the complete data sets are given in Appendix A.

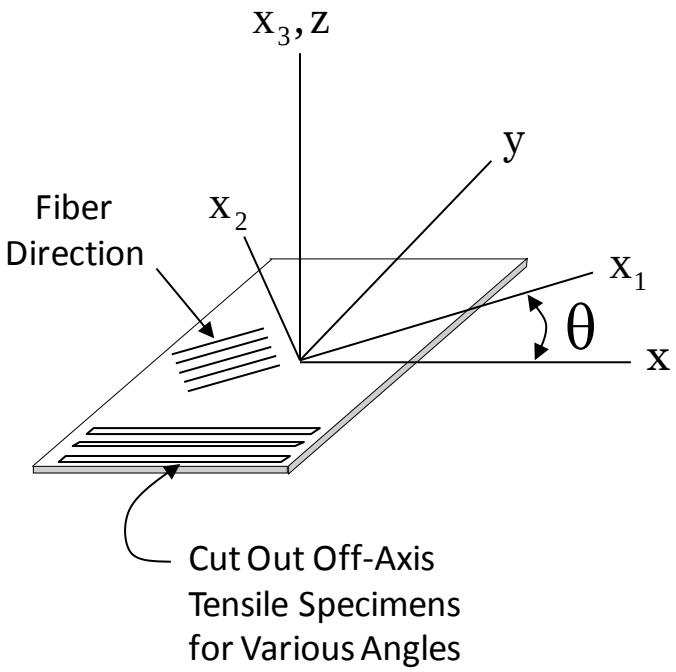

Figure 81. Off-Axis Tensile Specimens

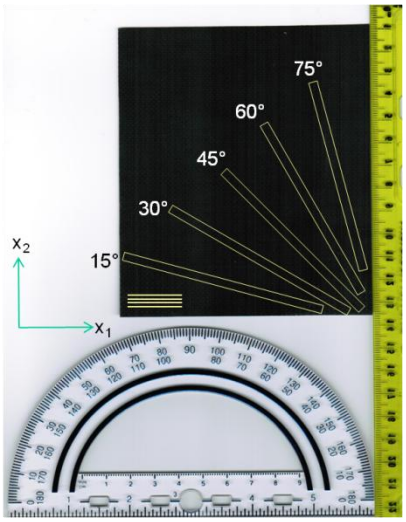

Figure 82. Sample Marked with Off-Axis Guide Lines

Figure 83. Hand Shear Used in Preparing Off-Axis Test Specimens

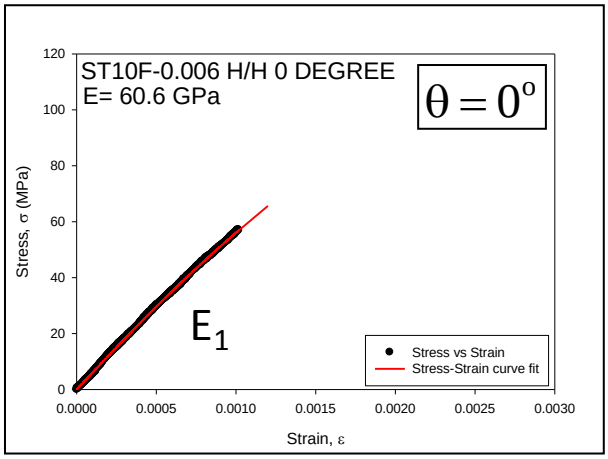

Figure 84. ST10F-0.006 H/H 0-Degree Elastic Modulus

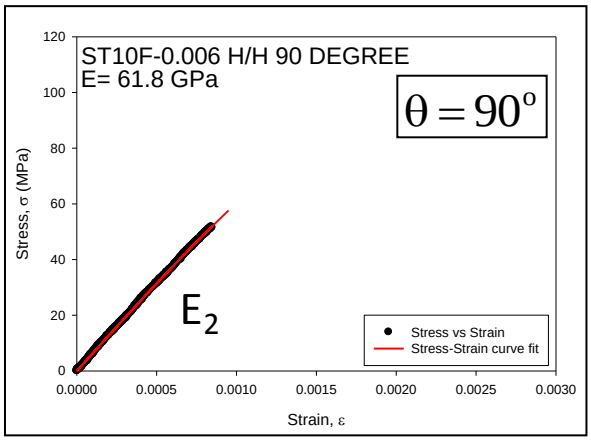

Figure 85. ST10F-0.006 H/H 90-Degree Elastic Modulus

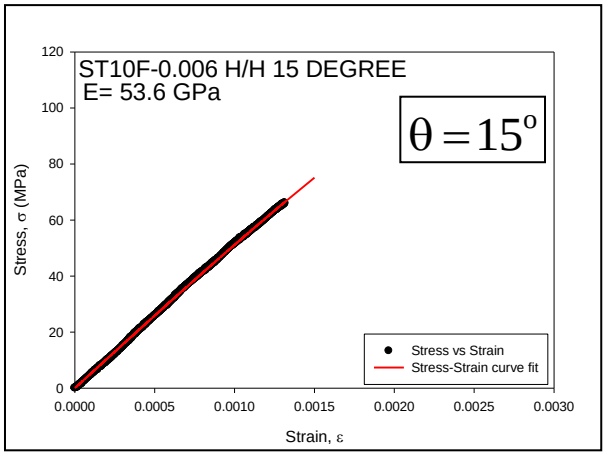

Figure 86. ST10F-0.006 H/H 15-Degree Elastic Modulus

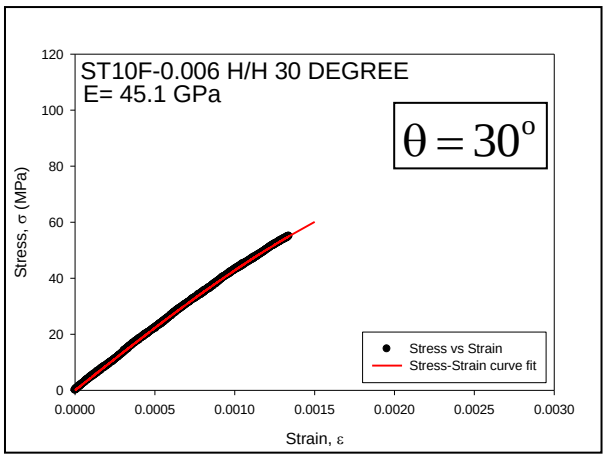

Figure 87. ST10F-0.006 H/H 30-Degree Elastic Modulus

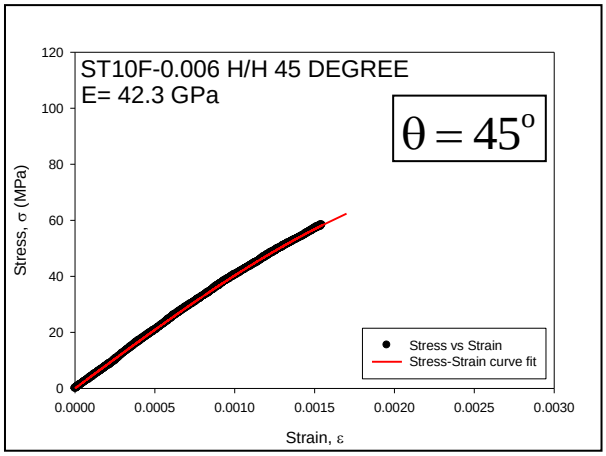

Figure 88. ST10F-0.006 H/H 45-Degree Elastic Modulus

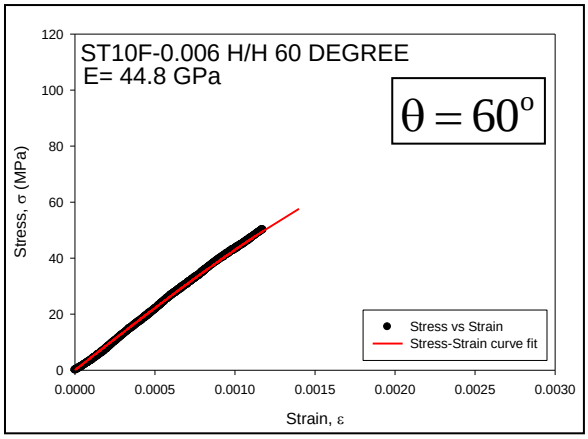

Figure 89. ST10F-0.006 H/H 60-Degree Elastic Modulus

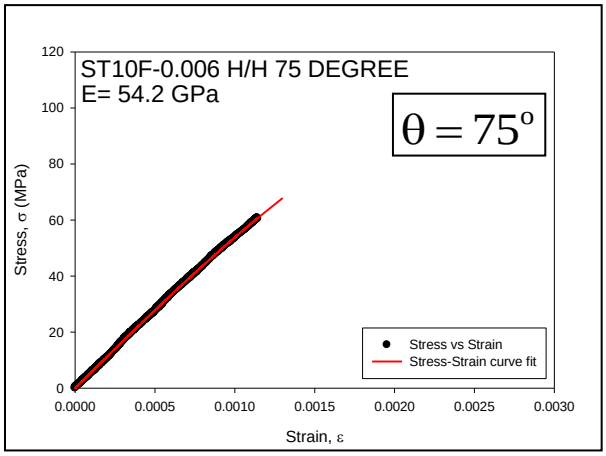

Figure 90. ST10F-0.006 H/H 75-Degree Elastic Modulus

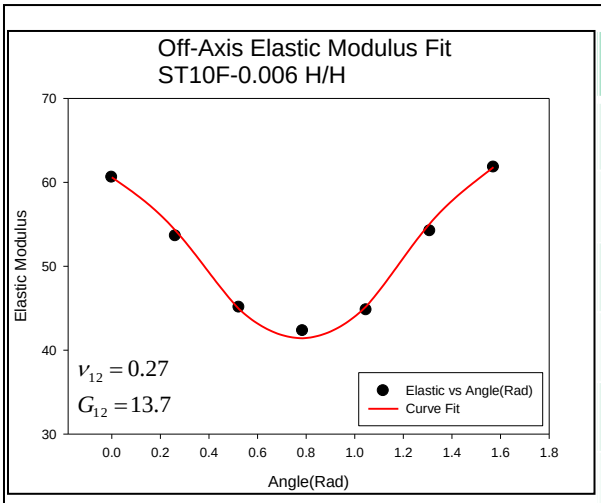

Goodness of fit:
R-squared: 0.994
Adjusted R-squared: 0.992

θ	E (GPa)
0	60.6
15	53.6
30	45.1
45	42.3
60	44.8
75	54.2
90	61.8

Figure 91. ST10F-0.006 H/H Elastic Modulus versus Off-Axis Angle

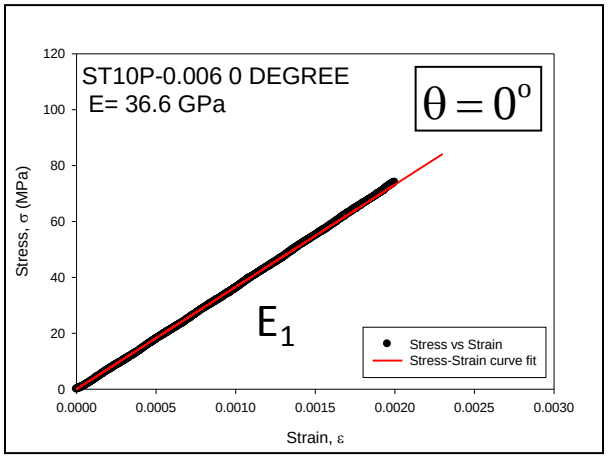

Figure 92. ST10P-0.006 0-Degree Elastic Modulus

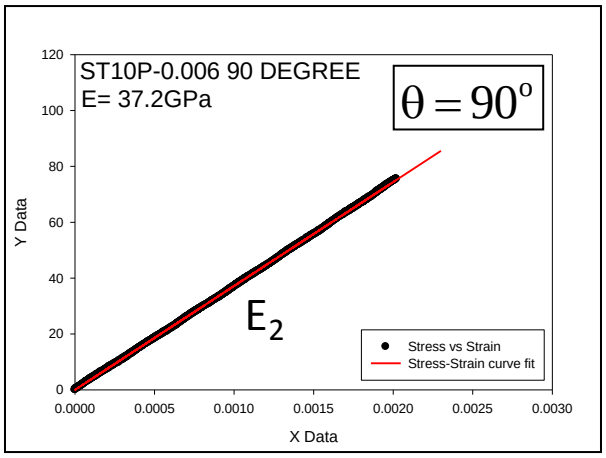

Figure 93. ST10P-0.006 90-Degree Elastic Modulus

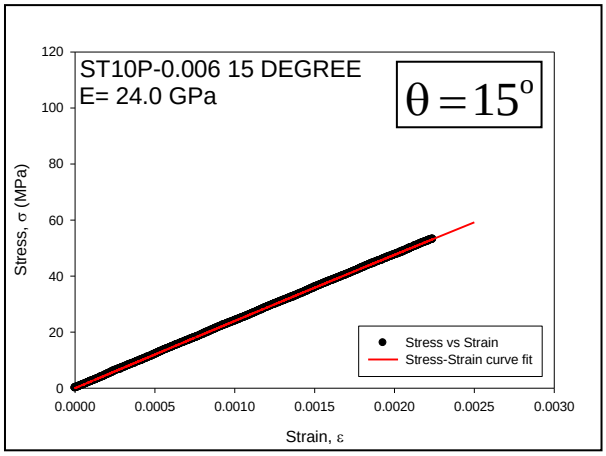

Figure 94. ST10P-0.006 15-Degree Elastic Modulus

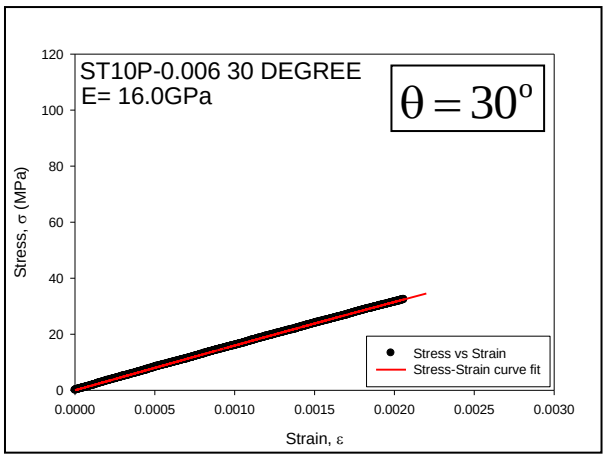

Figure 95. ST10P-0.006 30-Degree Elastic Modulus

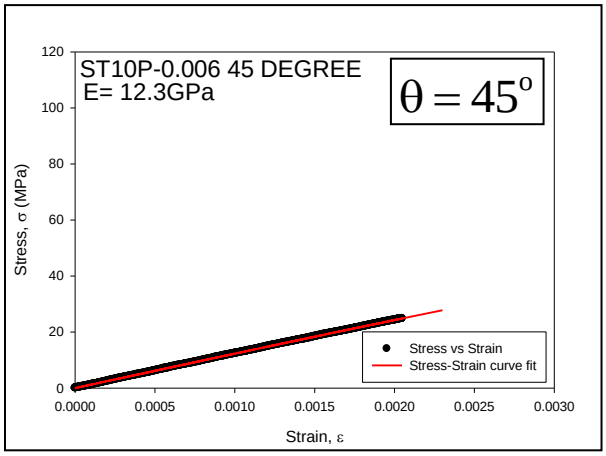

Figure 96. ST10P-0.006 45-Degree Elastic Modulus

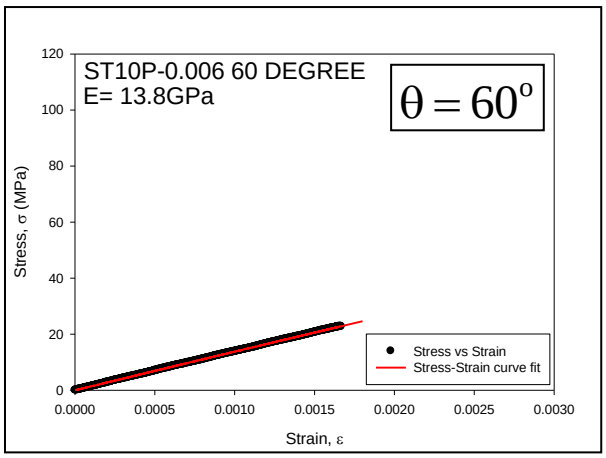

Figure 97. ST10P-0.006 60-Degree Elastic Modulus

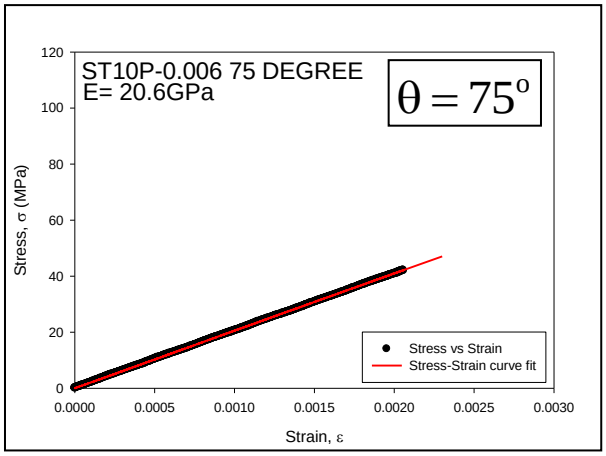

Figure 98. ST10P-0.006 75-Degree Elastic Modulus

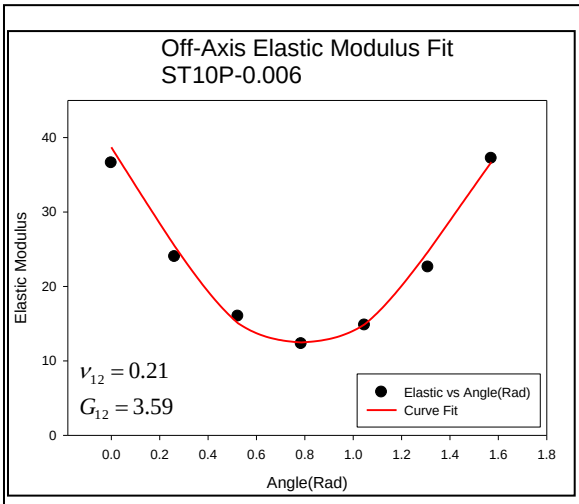

θ	E (GPa)
0	36.6
15	24.0
30	16.0
45	12.3
60	13.8
75	20.6
90	37.2

Goodness of fit:
R-squared: 0.993
Adjusted R-squared: 0.992

Figure 99. ST10P-0.006 Elastic Modulus versus Off-Axis Angle

Table 7. Shear Moduli and Poisson's Ratios for STABLCOR Ply Materials

Sample No.	Material Description	G_{12} (GPa)	Poisson's ratio, ν_{12}
1	ST10F-0.005	9.08	0.30
2	ST10F-0.006	4.31	0.33
3	ST10P-0.006	3.59	0.21
4	ST10F-0.006 H/H	13.70	0.27
5	ST10F-0.006 1/1	15.70	0.30
6	ST10P-0.006 H/H	11.80	0.29
7	ST10F-0.008	5.17	0.22
8	ST10P-0.008	3.93	0.30
9	ST10F-0.008 H/H	9.32	0.30
10	ST10P-0.008 H/H	6.76	0.33
11	ST10F-0.008 1/1	10.29	0.29
12	ST325P-180	2.07	0.30
13	ST325P-180 H/H	3.98	0.30
14	ST325P-0.008	2.51	0.30
15	ST325P-0.008 H/H	7.22	0.29
16	ST325P-0.010 255	2.31	0.29
17	ST325P-0.010 H/H	6.22	0.30
18	ST325P-0.010 1/1	6.48	0.30

VII. APPLICATIONS TO STABLCOR PRINTED CIRCUIT BOARDS

Description of Simulation Conditions

The lamination theory expressions in eq. (49) have been coded into a Matlab program (see Appendix B) with material properties as the input data. The developed Matlab program allows the user to input layer number (k), layer thickness (z_k), individual layer CTEs in the 1-direction (α_1) and 2-direction (α_2), elastic moduli in the 1 and 2 directions of each layer (E_1, E_2), shear modulus (G_{12}), Poisson's ratios (ν_{12}, ν_{21}), and temperature difference (ΔT). Moreover, the program is able to calculate thermally induced normal stress, thermally induced normal strain, and laminate CTE along both axes.

The results from the lamination theory Matlab program were compared to the finite element analysis solutions generated by ANSYS. The ANSYS program is able to create 3-dimensional models with various element attributes. In this work, 20 node solid elements (solid 186) were used, which provided providing non-linear deformation and large displacement simulations. All layers were considered perfectly bonded as a single bulk material.

In this study, analysis was performed using typical FR-4 material properties [29-30]. Furthermore, the material properties of ST325P-0.010 carbon-epoxy plies have been used for the STABLCOR carbon fiber layers in the PCBs. Table 8 shows the material properties which were used in both the lamination theory Matlab calculations as well as in the ANSYS finite element analysis simulations.

Two laminate configurations were analyzed as described in Tables 9 and 10. The first model consisted of a single STABLCOR layer sandwiched between two FR-4 layers. Figure 100 shows the dimensions of the single layer STABLCOR model, and Figure 101 shows the corresponding finite element mesh. The second model consisted of three STABLCOR layers and four FR-4 layers. The dimensions are shown in Figure 102 and the finite element mesh in Figure 103. To simulate free expansion in the finite element models, temperature changes of 25 ^{o}C and 50 ^{o}C were applied as loads. The initial temperature was taken to be 25 ^{o}C (room temperature).

Results and Conclusion

The results from both lamination theory and ANSYS finite element method have shown reasonable agreement. Eq. (49) was used for lamination theory CTE calculation, which was coded in Matlab program shown in Appendix B. Comparism of the lamination theory calculations and FEA predictions for the laminate CTE values are shown in Tables 11 and 12. Correlation is very good with percent differences about 10%. Both lamination theory and the FEA simulations showed that the CTEs in x-direction were lower than in the y-direction.

The differences in results for the 2 analysis methods are mainly due to the thermally induced expansions in the z-direction. The 3-dimension model used by the ANSYS simulation includes z-axis effects, while they are neglected in lamination theory.

Table 8. Lamination Theory and Finite Element Method Model Material Constants

Layer Properties	ST325P-0.010	FR-4 [28]
E_1	77 GPa	12 GPa
E_2	57.7 GPa	12 GPa
E_3	7.7 GPa	1.2 GPa
G_{12}	2.31 GPa	3.1 GPa
ν_{12}	0.29	0.27
ν_{21}	0.29	0.27
CTE (α_1)	4.1 (ppm/ ^{o}C)	12 (ppm/ ^{o}C)
CTE (α_2)	6.04 (ppm/ ^{o}C)	12 (ppm/ ^{o}C)
Thickness	0.255 mm	1.0 mm

Table 9. Laminate Layup – Single Layer STABLCOR Model

Layer	Material	Orientation Angle of 1-direction with x-direction
1	FR-4	0^{o}
2	ST325P-0.010 255	0^{o}
3	FR-4	0^{o}

Table 10. Laminate Layup – Three Layer STABLCOR Model

Layer	Material	Orientation Angle of 1-direction with x-direction
1	FR-4	0^{o}
2	ST325P-0.010 255	0^{o}
3	FR-4	0^{o}
4	ST325P-0.010 255	0^{o}
5	FR-4	0^{o}
6	ST325P-0.010 255	0^{o}
7	FR-4	0^{o}

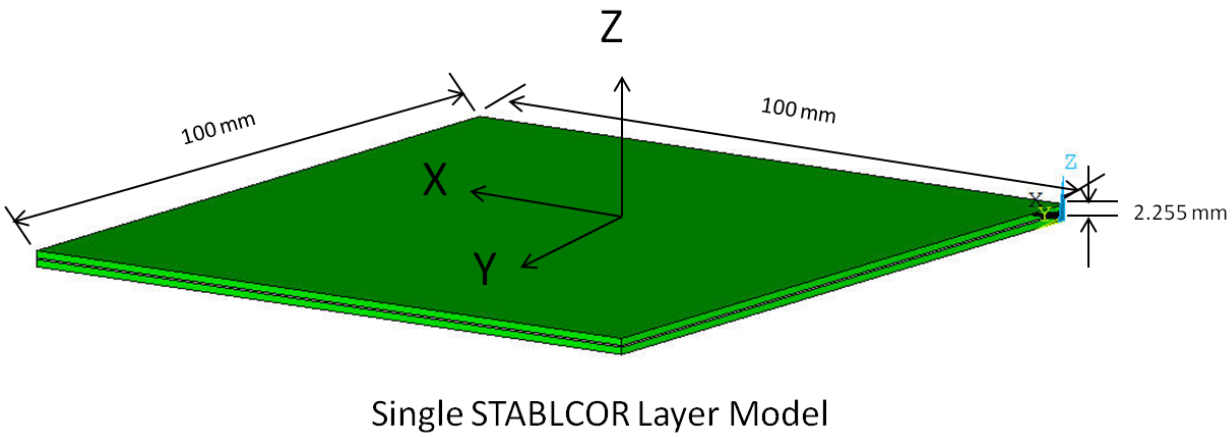

Figure 100. Single STABLCOR Layer PCB Model

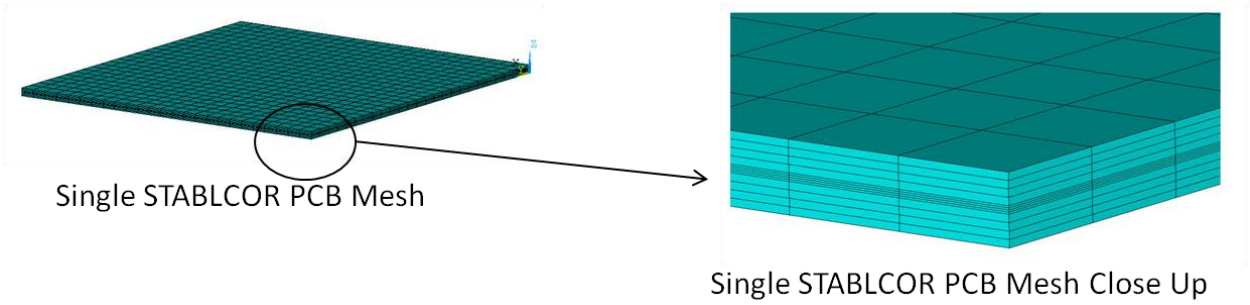

Figure 101. Single STABLCOR Layer Model Mesh with Solid Elements

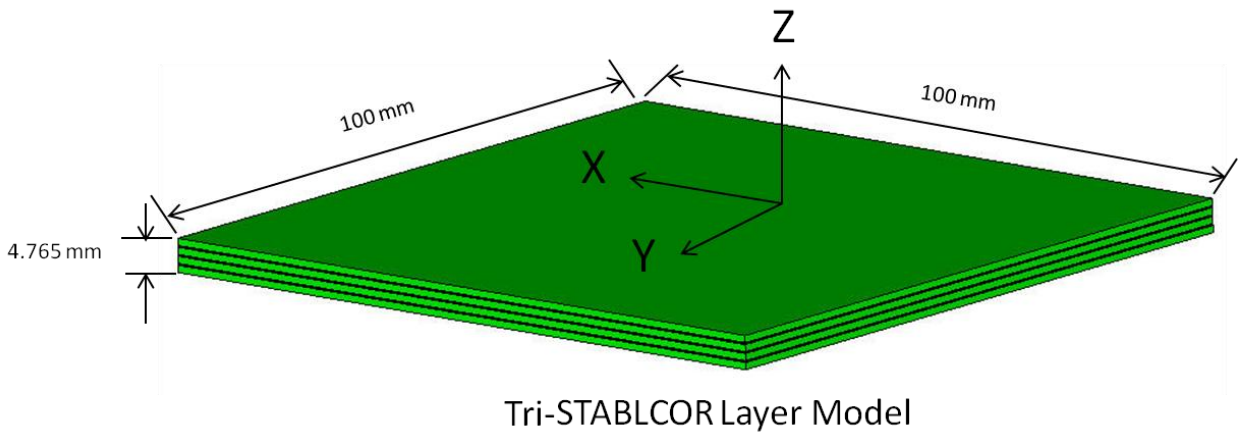

Figure 102. Three STABLCOR Layer PCB Model

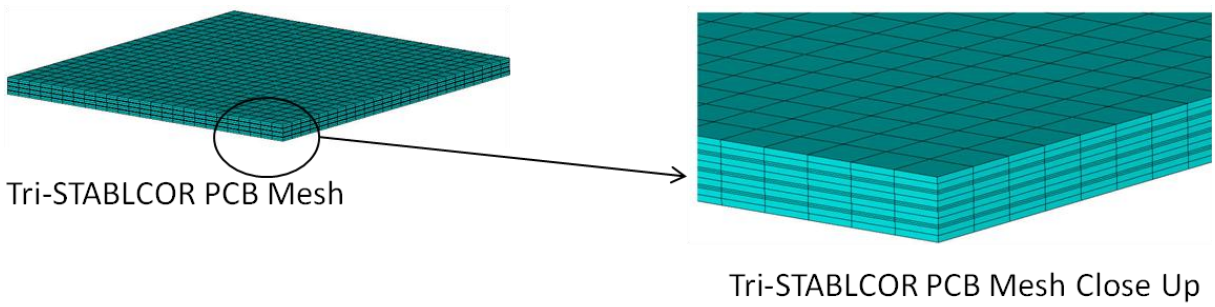

Figure 103. Three STABLCOR Layer Model Mesh with Solid Elements

Table 11. Single STABLCOR Layer Model CTE

	Lamination Theory [eq. (49)]	ANSYS FEM Simulation
α_x^0	8.62 ppm/^{o}C	8.15 ppm/^{o}C
α_y^0	10.83 ppm/^{o}C	9.76 ppm/^{o}C

Table 12. Three STABLCOR Layer Model CTE

	Lamination Theory [eq. (49)]	ANSYS FEM Simulation
α_x^0	7.86 ppm/^{o}C	7.20 ppm/^{o}C
α_y^0	10.46 ppm/^{o}C	9.14 ppm/^{o}C

VIII. SUMMARY AND CONCLUSIONS

Lamination theory is able to calculate the overall CTEs of the designed PCB. Lamination theory is able to calculate the mechanical properties of the PCB with different layer configuration. The CTEs of each STABLCOR layer can be measured by strain gages with correct procedures. The On-axis and off-axis elastic modulie can be measured by crosshead displacement. STABLCOR laminates could be edited into off-axis testing coupons for elastic modulus measurements. Off-axis elastic modulus regression fit can be used to calculate the shear modulus and Poisson's ratio of STABLCOR layer. The calculation results show the carbon fiber laminates were able to lower the overall CTEs of the PCB. However, the stack-up ratios between STABLCOR and FR-4 layers have critical effects to the overall CTEs. Since the silicon chip has an extremely low CTE, the ideal PCB needs to have a CTE range from 3 ppm/^{o}C to 4 ppm/^{o}C. The calculated PCB CTEs were still not preferable with the stack-up configurations used in this study. Moreover, to set the CTE even lower than current models, higher ratio of STABLCOR to FR-4 may be needed. The calculated CTEs from lamination theory have good correspond with the simulation results from finite element method.

REFERENCES

1. Andrews, J. A., "Flip Chip Package and Method of Making," *Patent number: 5352926*, 1993.
2. Dally, J. W., Lall, P., and Suhling, J. C., *Mechanical Design of Electronic Systems*, College House Enterprises, 2008.
3. Engelmaier, W., and Attarwala, A. I., "Surface-mount Attachment Reliability of Clip-leaded Ceramic Chip Carriers on FR-4 Circuit Boards," *IEEE Transactions on Components, Hybrids, and Manufacturing Technology*, Vol. 12(2), pp. 284-296, 1989.
4. Powell, D. O., and Trivedi, A. K., "Flip-chip on FR-4 Integrated Circuit Packaging," *Proceedings of the 43rd Electronic Components and Technology Conference*, pp. 182-186, 1993.
5. Qi, H., Ganesan, S., Wu, J., and Pecht M., "Effects of Printed Circuit Board Materials on Lead-free Interconnect Durability," *5th International Conference on Polymers and Adhesives in Microelectronics and Photonics*, pp. 140-144, 2005.
6. Jones R. M., *Mechanics of Composite Materials*, Taylor & Francis Inc. 1999.
7. Dally, J. W., and Riley, W. F., *Experimental Stress Analysis*, Fourth Ed., College House Enterprises, 2005.
8. Nakagawa, Y., and Yokoyama, R., "Optimum Design of Printed Circuit Board to Reduce Deformation in Reflow Process by a Global Optimization Method," *Journal of Material and Design*, Vol. 33, pp. 164-174, 2012.
9. Tan, W., Ume, I. C., "Application of Lamination Theory to Study Warpage Across PWB and PWBA During Convective Reflow Process," *IEEE Transactions on Components, Packaging and Manufacturing Technology*, Vol. 2(2), pp. 217-223, 2012.
10. Tseng, T., Lee, C., Liu, W., and Yu, C., "Circuit Board," Patent Number:12/944275, 2012.
11. Vasoya, K. K., Mangrolia, B. M., and Davis, W. E., "Lightweight Circuit Board with Conductive Constraining Cores, United States Patent," Patent Number: 7,667,142 B2, 2010.
12. Jensen, W. M., "Printed Wiring Board Substrates for Ceramic Chip Carriers," Patent Number: 4,318,954, 1981.
13. Leibowitz, J. D., "Multilayer Printed Circuit Board Structure," Patent Number: 4,591,659, 1983.
14. Burch, C., and Vasoya, K., "Carbon Composite for Tough PCB Design Specifications," *OnBoard Technology*, pp. 10-12, Oct. 2006.
15. Vasoya, K., and Burch, C., "Key Benefits of Carbon Fibers in a Printed Circuit Board and Integrated Circuit Substrate," *Society for the Advancement of Material and Process Engineering*, 2006.
16. *STABLCOR TECHNOLOGY, Inc. (2011).* Retrieved July 2011, from http://www.stablcor.com/Technology.html
17. Burch, C., and Vasoya , K., "STABLCOR Groundbreaking PCB and Substrate Material," *VMEbus Systems Magazine*, pp. 56-59, 2005.

18. *STABLCOR TECHNOLOGY, Inc. (2011).* Retrieved July 2011, from http://www.stablcor.com/applications.html
19. Ratanawilai, T. B., Hunter, B., Subbarayan, G., and Rose, D., "A Study on the Variation of Effective CTE of Printed Circuit Boards Through a Validated Comparison Between Strain Gages and Moiré Interferometry," *IEEE Transactions on Components and Packaging Technologies*, Vol. 26(4), pp. 712-718, 2003.
20. "General Purpose Strain Gage – Linear Pattern," *Measurement Group Vishay, Inc.*, Document No: 11508, 2003.
21. "Measurement of Thermal Expansion Coefficient Using Strain Gages," *Tech Note TN-513-1*, Vishay Measurement Group, Document Number: 11063
22. "Strain Gage Selection – Criteria Procedures, Recommendations," *Tech Note TN-505-4*, Vishay Measurement Group, Document Number: 11055
23. Lang, E. J., and Chou, T. W., "The Effect of Strain Gage Size on Measurement Errors In Textile Composite Materials," *Composites Science and Technology*, Vol. 58, pp. 539-549, 1998.
24. Mujika, F., Mondragon, I., Berglund, L. A., and Varna, J., "45^{o} Flexure Test for Measurement of In-Plane Shear Modulus," *Journal of Composite Materials*, Vol. 36, pp. 2313-2337, 2002.
25. Mujika, F., Valea, A., Ganan, P., and Mondragon, I., "Off-Axis Flexure Test: A New Method for Obtaining In-Plane Shear Properties," *Journal of Composite Materials*, Vol. 39, pp. 953-980, 2005.
26. Vargas, G., and Mujika, F., "Determination of In-plane Shear Strength of Unidirectional Composite Materials Using the Off-axis Three-point Flexure and Off-Axis Tensile Tests," *Journal of Composite Materials*, Vol. 44, pp. 2487-2507, 2010.
27. Chamis, C.C., and Sinclair J.H., "Ten-deg Off-Axis Test for Shear Properties in Fiber Composites," *Experimental Mechanics*, Vol. 17(9), pp. 339-346, 1977.
28. Saliklis, E. P., and Falk, R. H., "Correlating Off-Axis Tension Tests to Shear Modulus of Wood-Based Panels," *Journal of Structural Engineering*, Vol. 126(5), pp. 621-625, 2000.
29. Kim, Y. K., "Viscoelastic Effect of FR-4 Material on Packaging Stress Development," *IEEE Transactions on Advanced Packaging*, Vol. 30(3), pp. 411-420, 2007.
30. Lau, J. H., and Lee, R. S. W., "Effects of Build-Up Printed Circuit Board Thickness on the Solder Joint Reliability of a Wafer Level Chip Scale Package," *IEEE Transactions on Components and Packaging Technologies*, Vol. 25(1), pp. 3-14, 2002.

APPENDIX A - ELASTIC MODULUS VERSUS OFF-AXIS ANGLE

Table 13. Curve Fit Shear Moduli and Poisson's Ratios

Sample No.	Material Description	G_{12} (GPa)	Poisson's ratio, ν_{12}	Graph Page No.
1	ST10F-0.005	9.08	0.30	105-108
2	ST10F-0.005 H/H	17.76	0.30	109-112
3	ST10F-0.006	4.31	0.33	113-116
4	ST10P-0.006	3.59	0.21	85-88
5	ST10F-0.006 H/H	13.70	0.27	89-92
6	ST10F-0.006 1/1	15.70	0.30	117-120
7	ST10P-0.006 H/H	11.80	0.29	121-124
8	ST10F-0.008	5.17	0.22	125-128
9	ST10P-0.008	3.93	0.30	129-132
10	ST10F-0.008 H/H	9.32	0.30	133-136
11	ST10P-0.008 H/H	6.76	0.33	137-140
12	ST10F-0.008 1/1	10.29	0.29	141-144
13	ST325P-180	2.07	0.30	145-148
14	ST325P-180 H/H	3.98	0.30	149-152
15	ST325P-0.008	2.51	0.30	153-156
16	ST325P-0.008 H/H	7.22	0.29	157-160
17	ST325P-0.010 240	2.67	0.23	161-164
18	ST325P-0.010 255	2.31	0.29	165-168
19	ST325P-0.010 H/H	6.22	0.30	169-172
20	ST325P-0.010 1/1	6.48	0.30	173-176

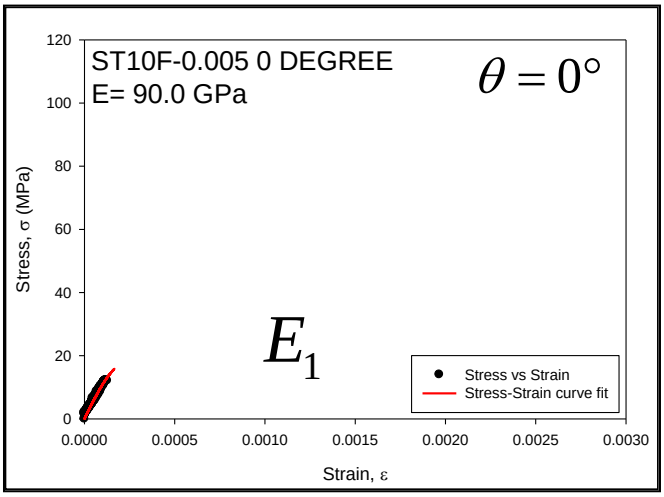

Figure 104. ST10F-0.005 0-Degree Elastic Modulus

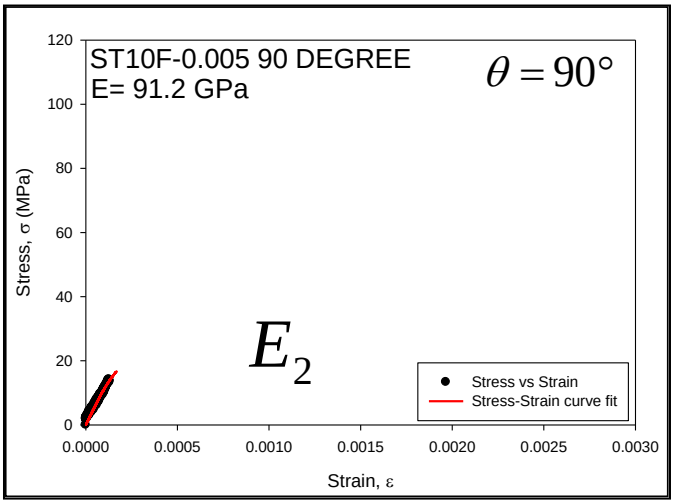

Figure 105. ST10F-0.005 90-Degree Elastic Modulus

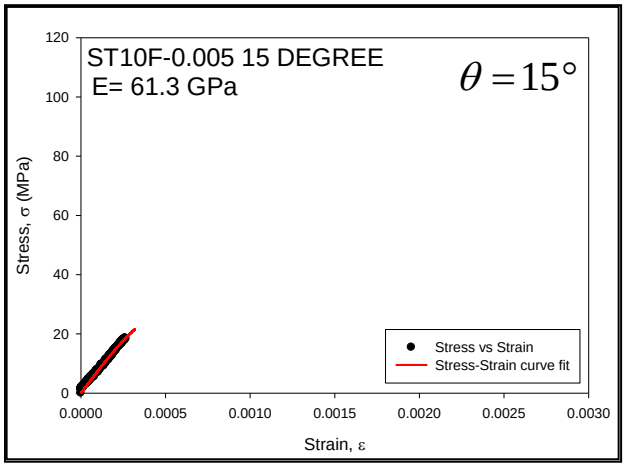

Figure 106. ST10F-0.005 15-Degree Elastic Modulus

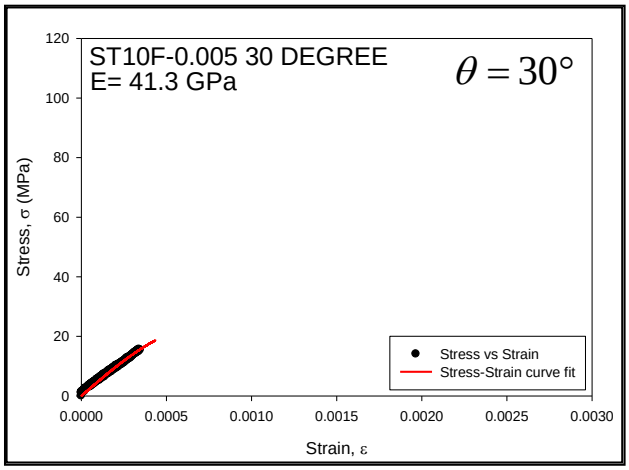

Figure 107. ST10F-0.005 30-Degree Elastic Modulus

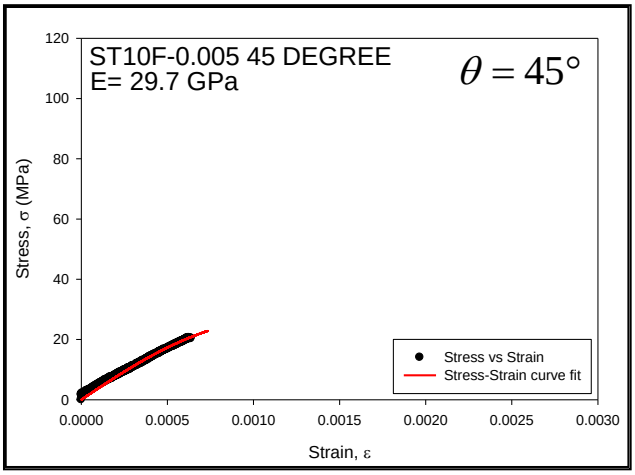

Figure 108. ST10F-0.005 45-Degree Elastic Modulus

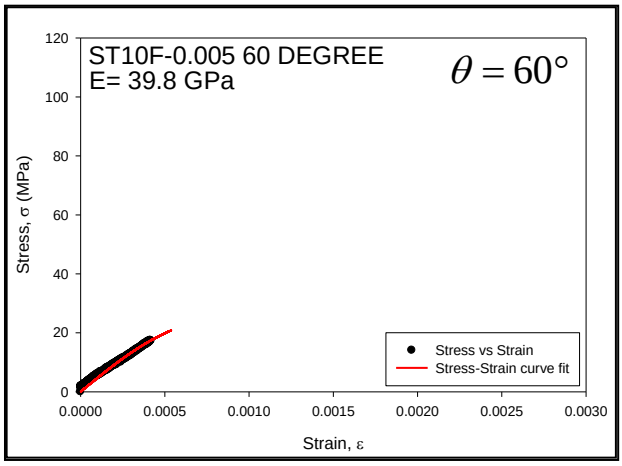

Figure 109. ST10F-0.005 60-Degree Elastic Modulus

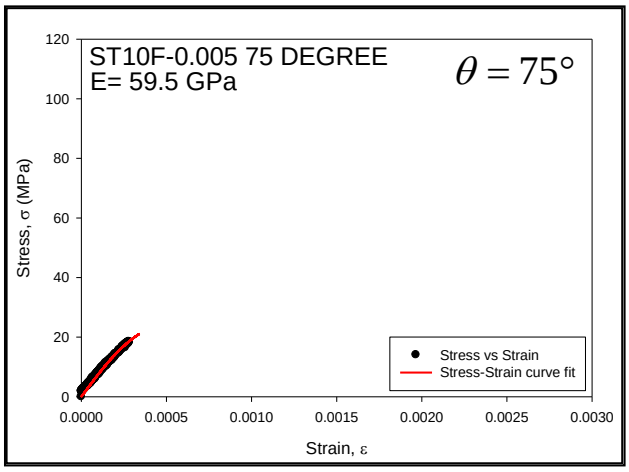

Figure 110. ST10F-0.005 75-Degree Elastic Modulus

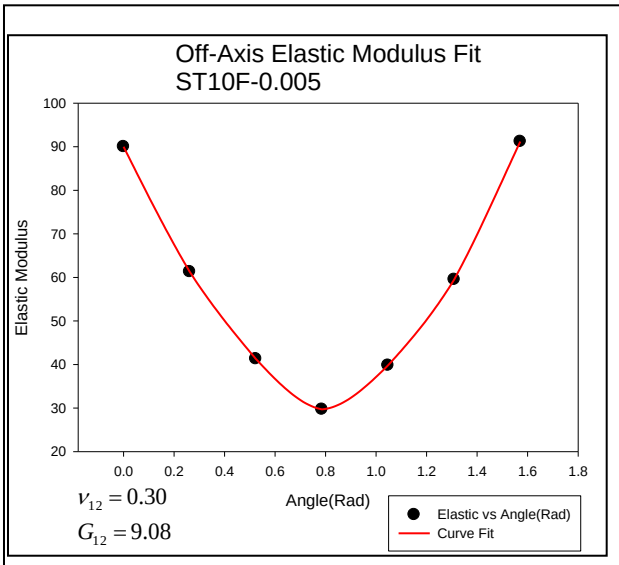

θ	E (GPa)
0	90.0
15	61.3
30	41.3
45	29.7
60	39.8
75	59.5
90	91.2

Goodness of fit:
R-squared: 0.9925
Adjusted R-squared: 0.991

Figure 111. ST10F-0.005 Elastic Modulus versus Off-Axis Angle Curve Fitting Plot

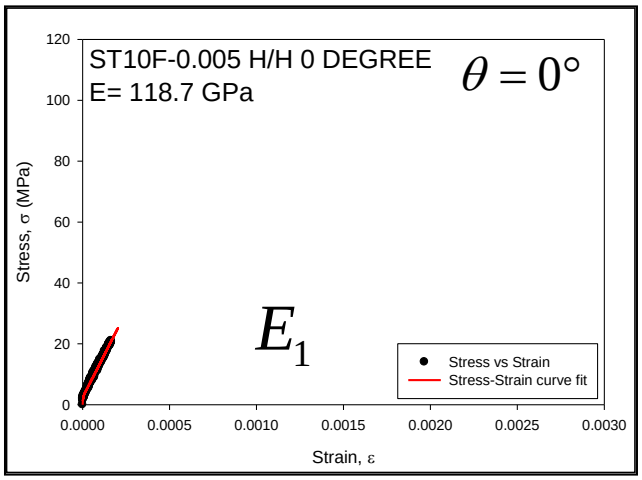

Figure 112. ST10F-0.005 H/H 0-Degree Elastic Modulus

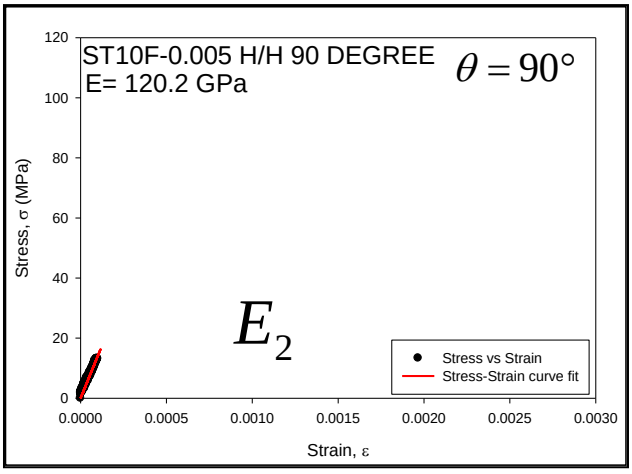

Figure 113. ST10F-0.005 H/H 90-Degree Elastic Modulus

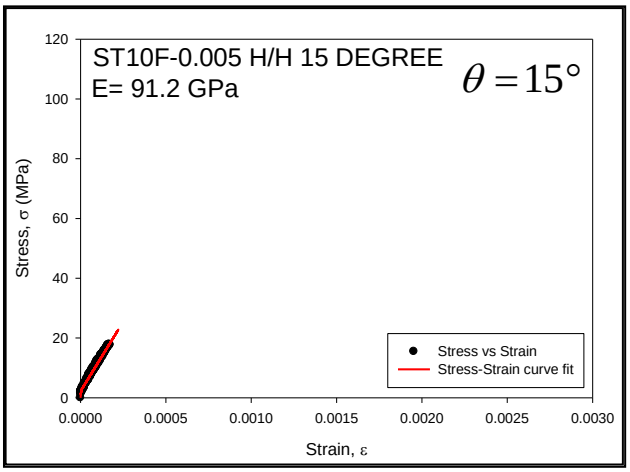

Figure 114. ST10F-0.005 H/H 15-Degree Elastic Modulus

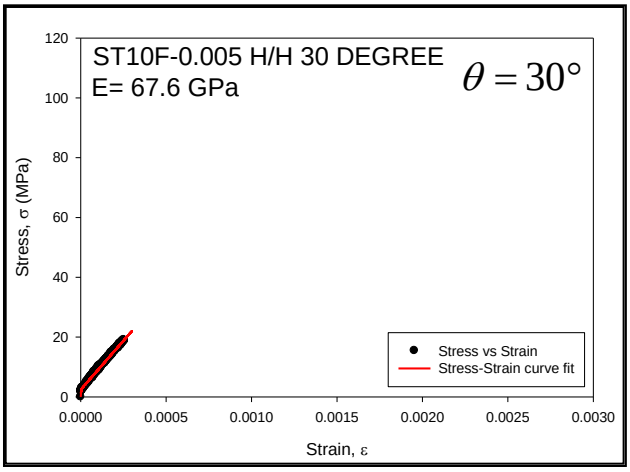

Figure 115. ST10F-0.005 H/H 30-Degree Elastic Modulus

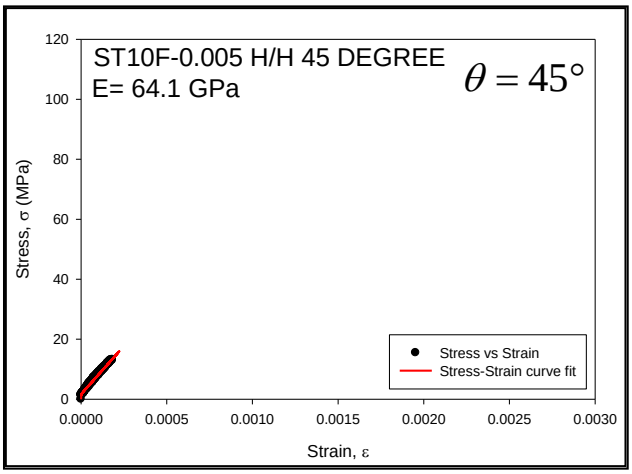

Figure 116. ST10F-0.005 H/H 45-Degree Elastic Modulus

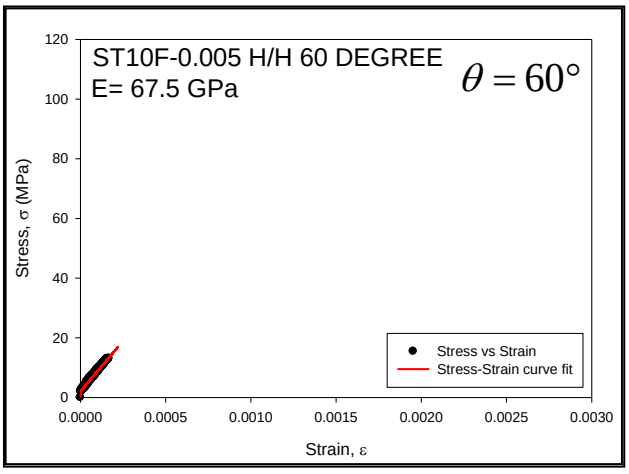

Figure 117. ST10F-0.005 H/H 60-Degree Elastic Modulus

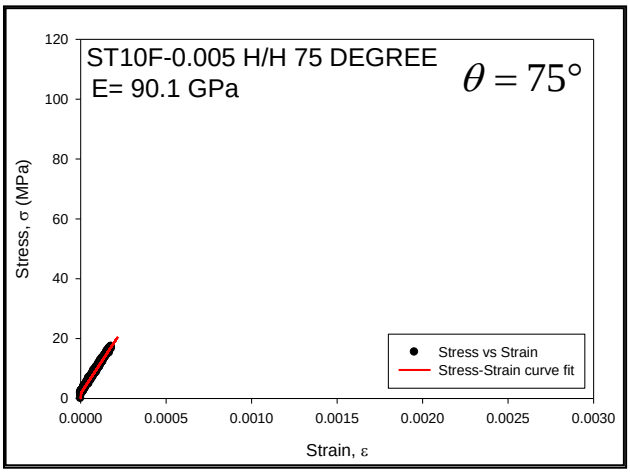

Figure 118. ST10F-0.005 H/H 75-Degree Elastic Modulus

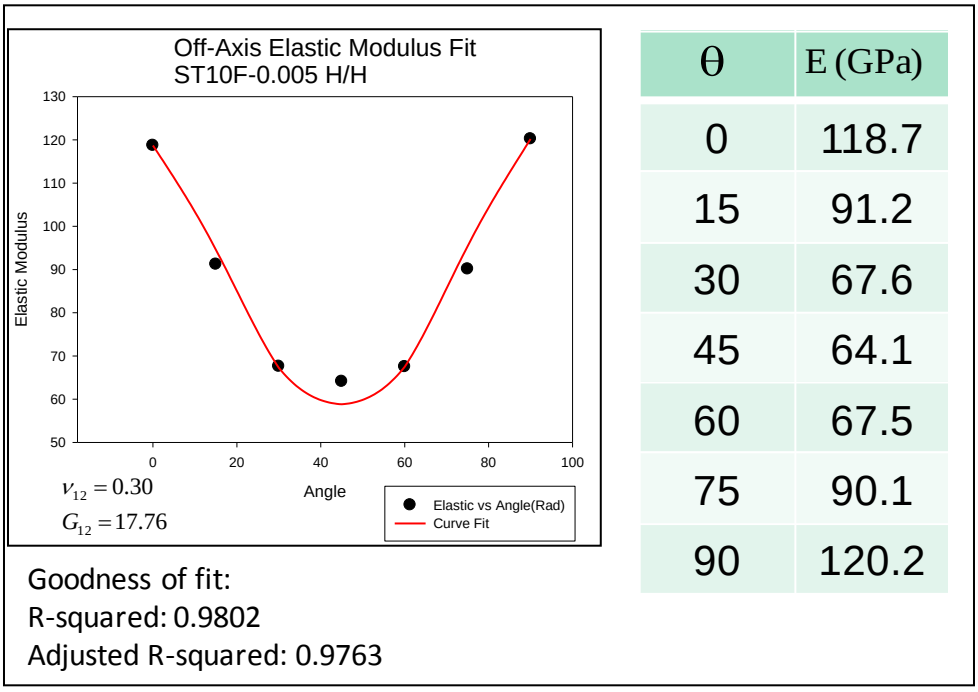

θ	E (GPa)
0	118.7
15	91.2
30	67.6
45	64.1
60	67.5
75	90.1
90	120.2

Goodness of fit:
R-squared: 0.9802
Adjusted R-squared: 0.9763

Figure 119. ST10F-0.005 H/H Elastic Modulus versus Off-Axis Angle Curve Fitting Plot

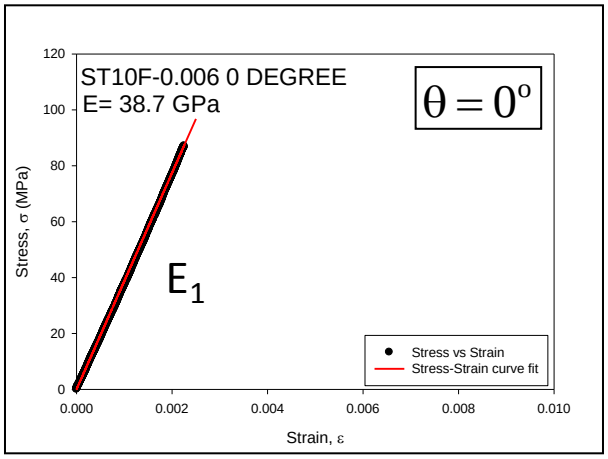

Figure 120. ST10F-0.006 0-Degree Elastic Modulus

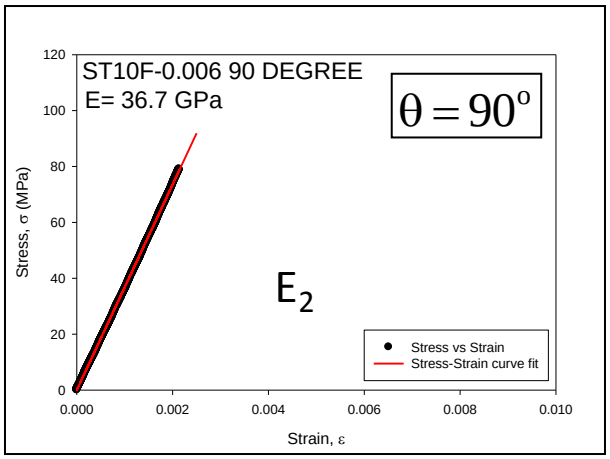

Figure 121. ST10F-0.006 90-Degree Elastic Modulus

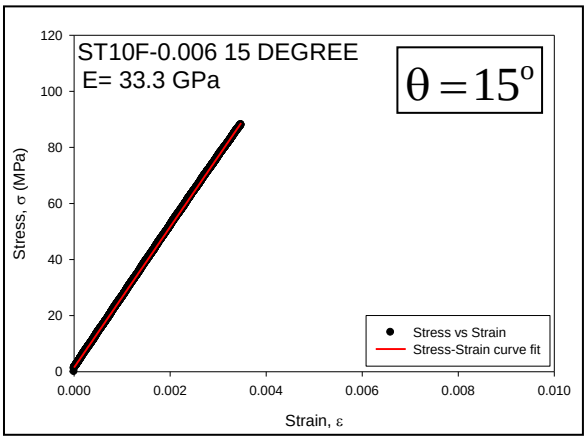

Figure 122. ST10F-0.006 15-Degree Elastic Modulus

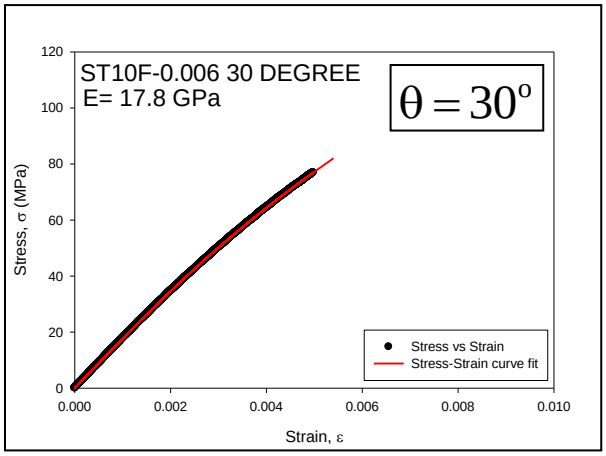

Figure 123. ST10F-0.006 30-Degree Elastic Modulus

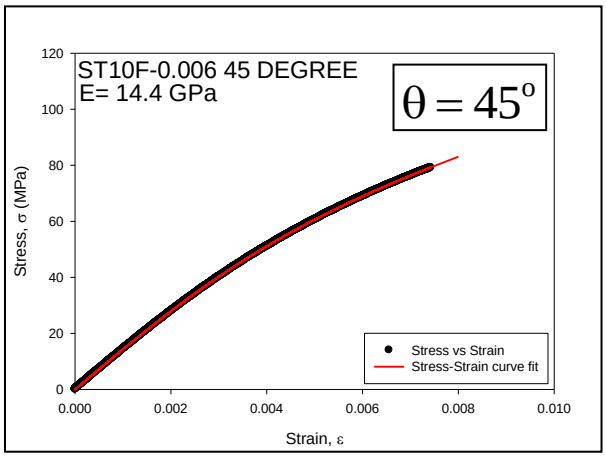

Figure 124. ST10F-0.006 45-Degree Elastic Modulus

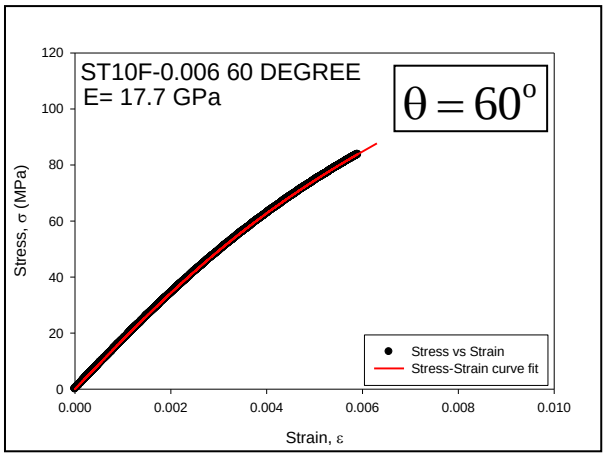

Figure 125. ST10F-0.006 60-Degree Elastic Modulus

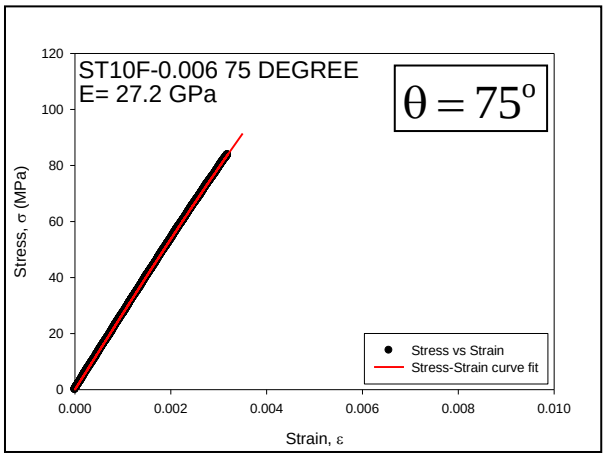

Figure 126. ST10F-0.006 75-Degree Elastic Modulus

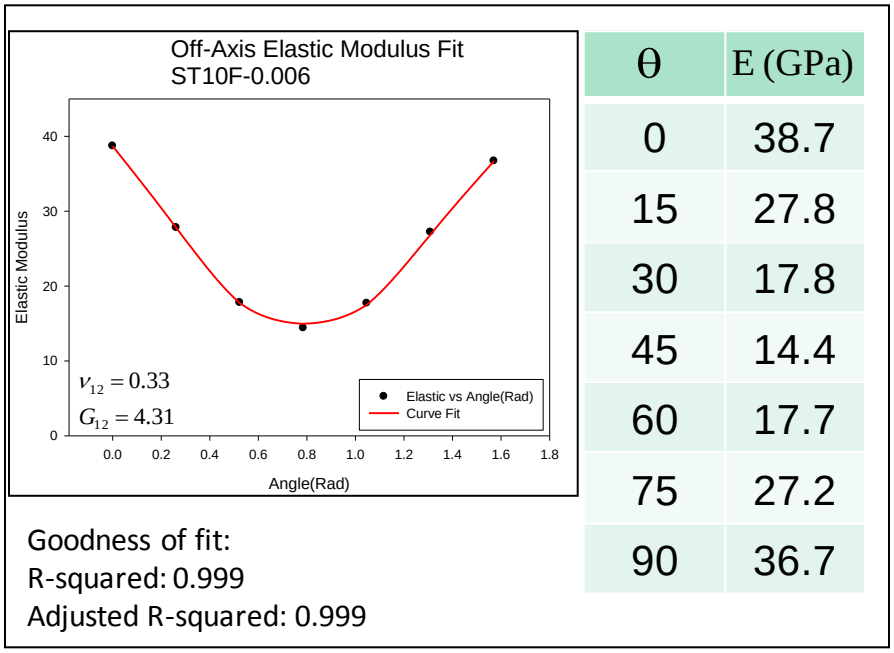

θ	E (GPa)
0	38.7
15	27.8
30	17.8
45	14.4
60	17.7
75	27.2
90	36.7

Figure 127. ST10F-0.006 Elastic Modulus versus Off-Axis Angle Curve Fitting Plot

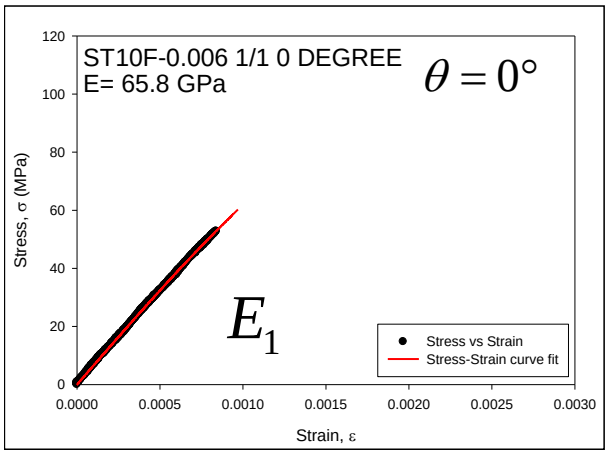

Figure 128. ST10F-0.006 1/1 0-Degree Elastic Modulus

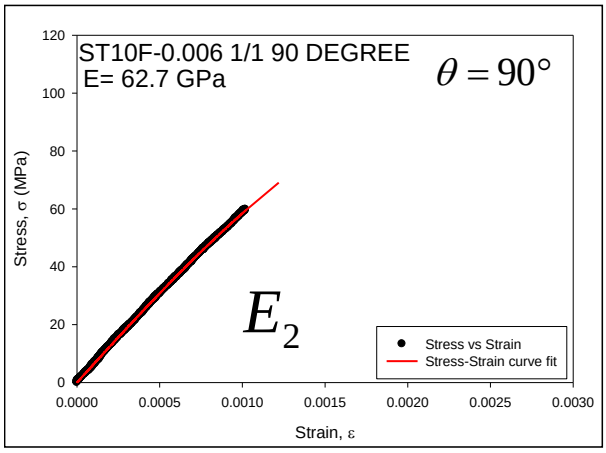

Figure 129. ST10F-0.006 1/1 90-Degree Elastic Modulus

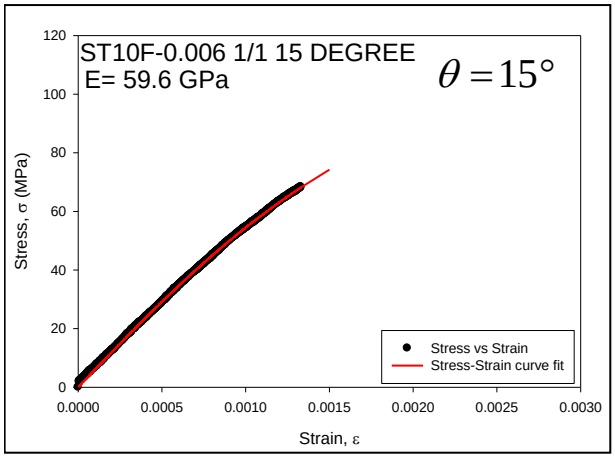

Figure 130. ST10F-0.006 1/1 15-Degree Elastic Modulus

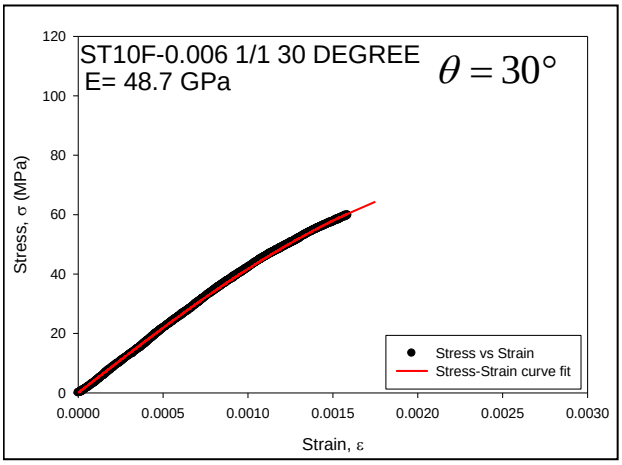

Figure 131. ST10F-0.006 1/1 30-Degree Elastic Modulus

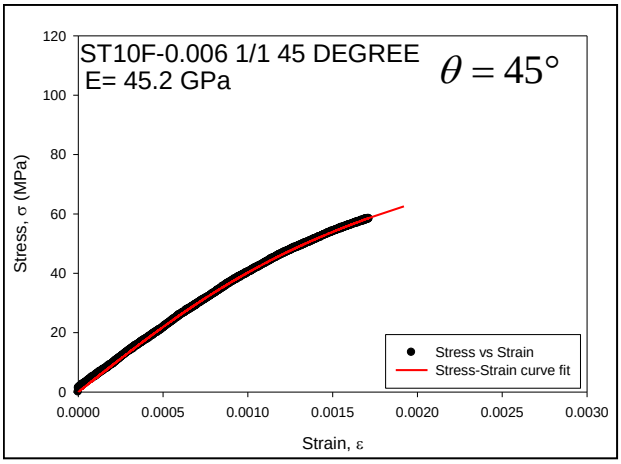

Figure 132. ST10F-0.006 1/1 45-Degree Elastic Modulus

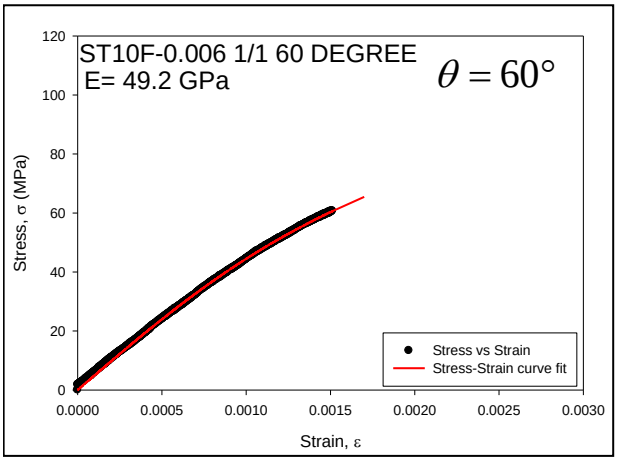

Figure 133. ST10F-0.006 1/1 60-Degree Elastic Modulus

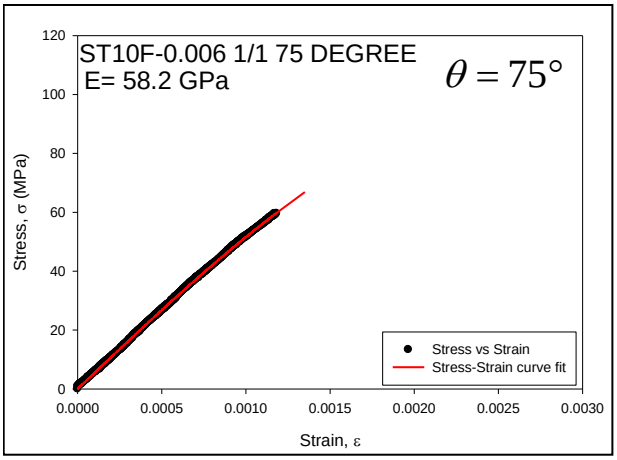

Figure 134. ST10F-0.006 1/1 75-Degree Elastic Modulus

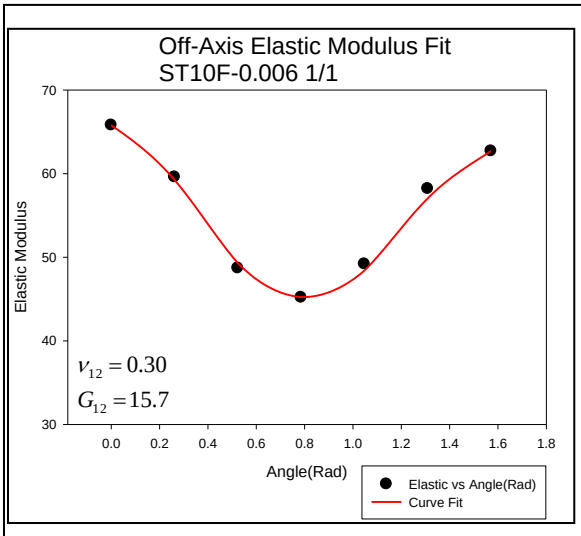

θ	E (GPa)
0	65.8
15	59.6
30	48.7
45	45.2
60	49.2
75	58.2
90	62.7

Goodness of fit:
R-squared: 0.9939
Adjusted R-squared: 0.9927

Figure 135. ST10F-0.006 1/1 Elastic Modulus versus Off-Axis Angle Curve Fitting Plot

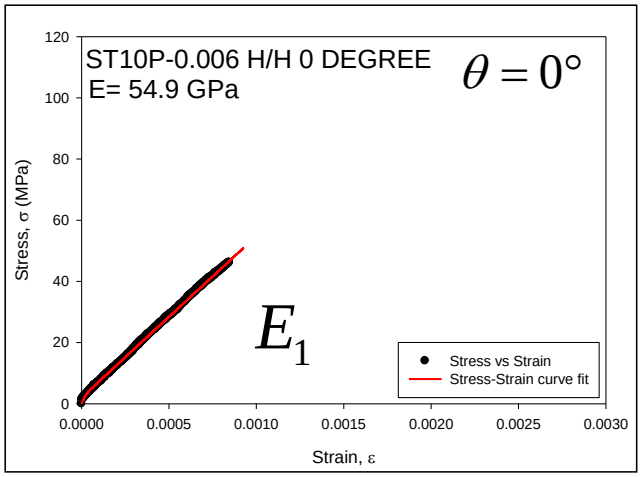

Figure 136. ST10P-0.006 H/H 0-Degree Elastic Modulus

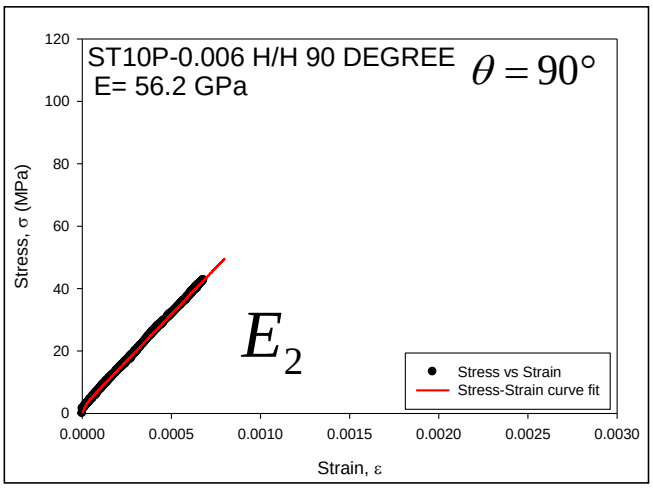

Figure 137. ST10P-0.006 H/H 90-Degree Elastic Modulus

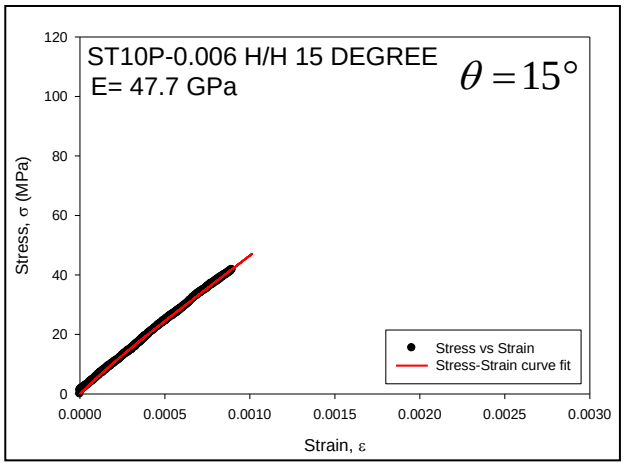

Figure 138. ST10P-0.006 H/H 15-Degree Elastic Modulus

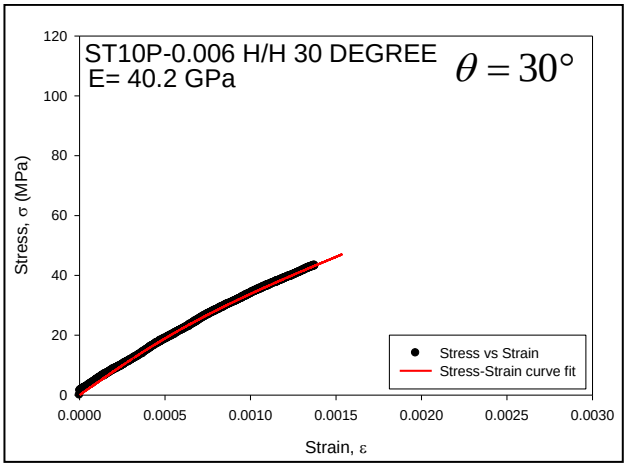

Figure 139. ST10P-0.006 H/H 30-Degree Elastic Modulus

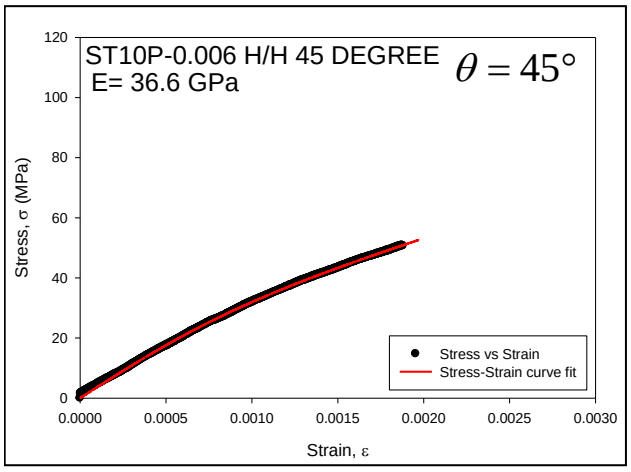

Figure 140. ST10P-0.006 H/H 45-Degree Elastic Modulus

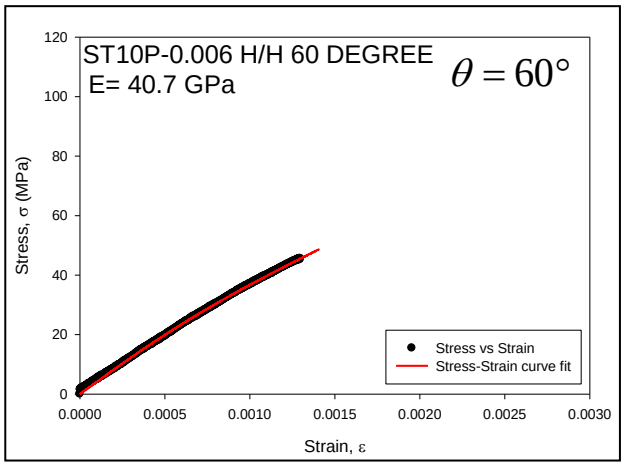

Figure 141. ST10P-0.006 H/H 60-Degree Elastic Modulus

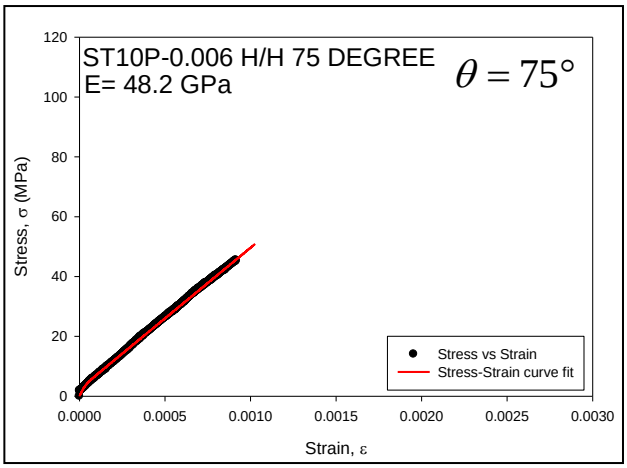

Figure 142. ST10P-0.006 H/H 75-Degree Elastic Modulus

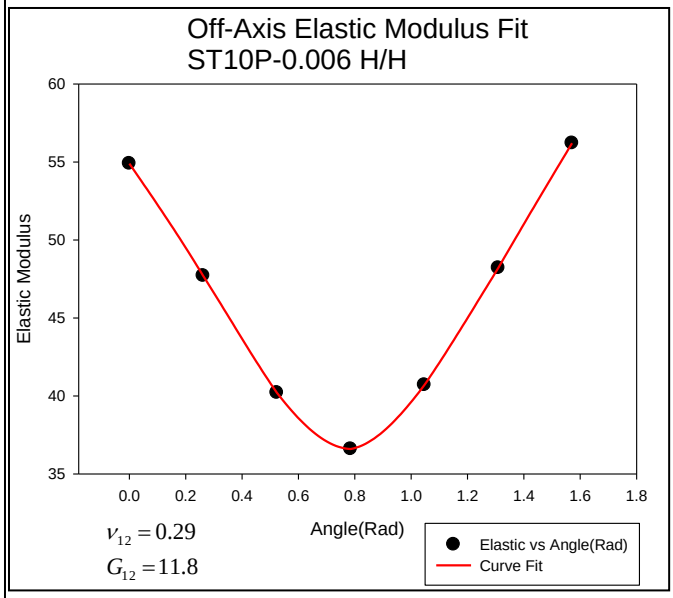

θ	E (GPa)
0	54.9
15	47.7
30	40.2
45	36.6
60	40.7
75	48.2
90	56.2

Goodness of fit:
R-squared: 0.989
Adjusted R-squared: 0.987

Figure 143. ST10P-0.006 H/H Elastic Modulus versus Off-Axis Angle Curve Fitting Plot

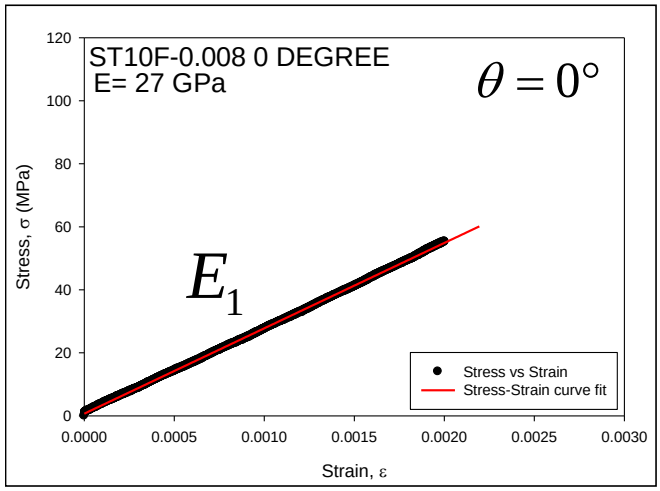

Figure 144. ST10F-0.008 0-Degree Elastic Modulus

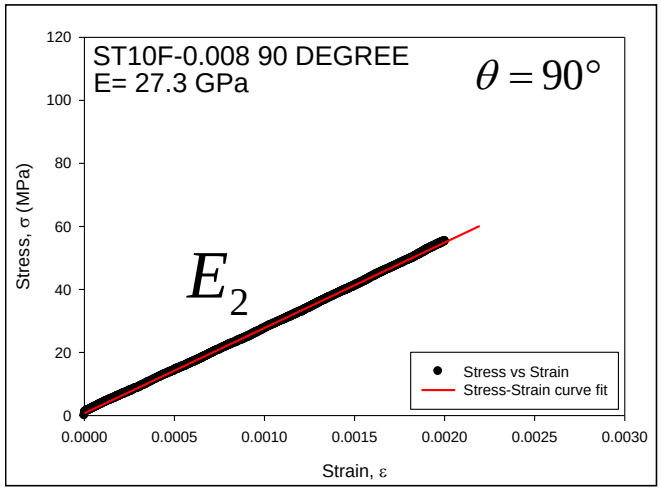

Figure 145. ST10F-0.008 90-Degree Elastic Modulus

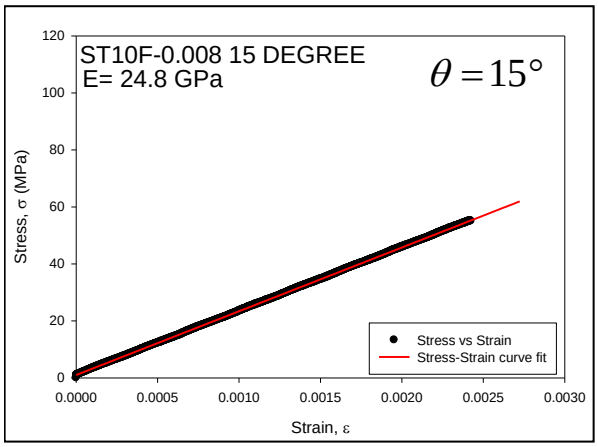

Figure 146. ST10F-0.008 15-Degree Elastic Modulus

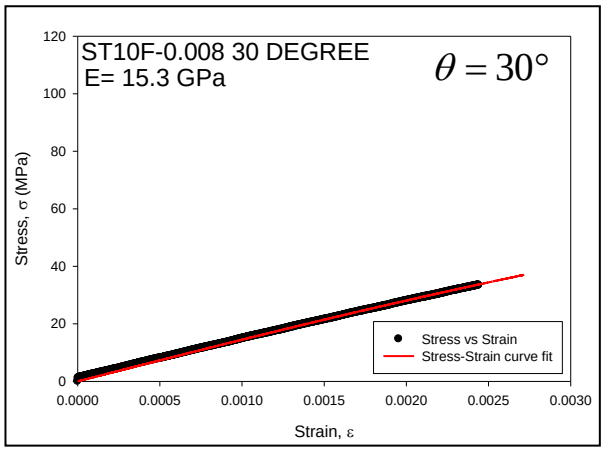

Figure 147. ST10F-0.008 30-Degree Elastic Modulus

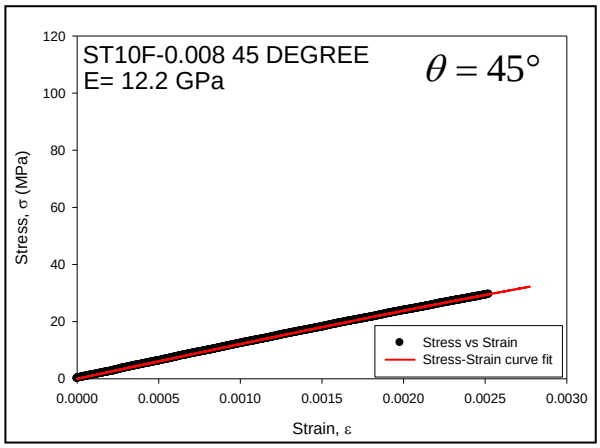

Figure 148. ST10F-0.008 45-Degree Elastic Modulus

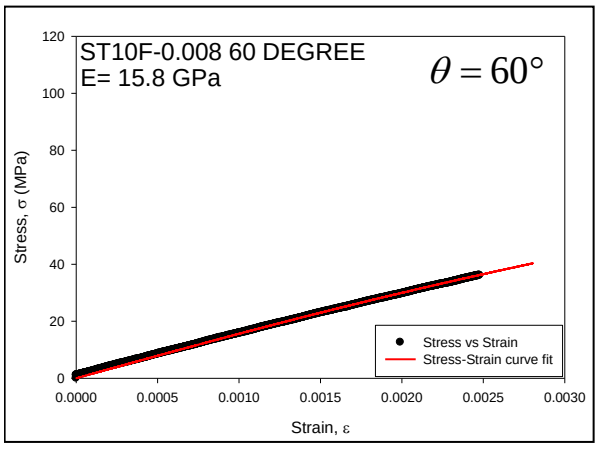

Figure 149. ST10F-0.008 60-Degree Elastic Modulus

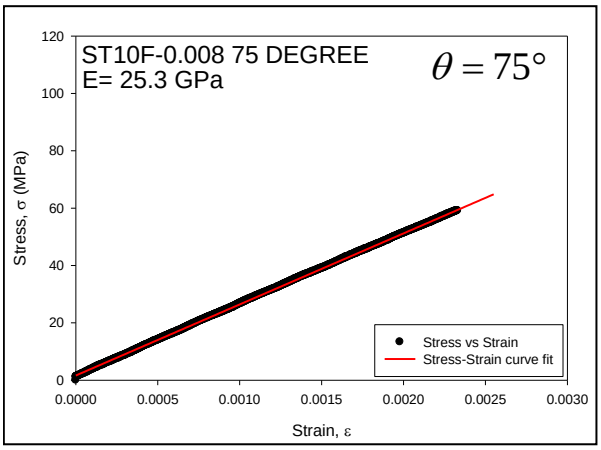

Figure 150. ST10F-0.008 75-Degree Elastic Modulus

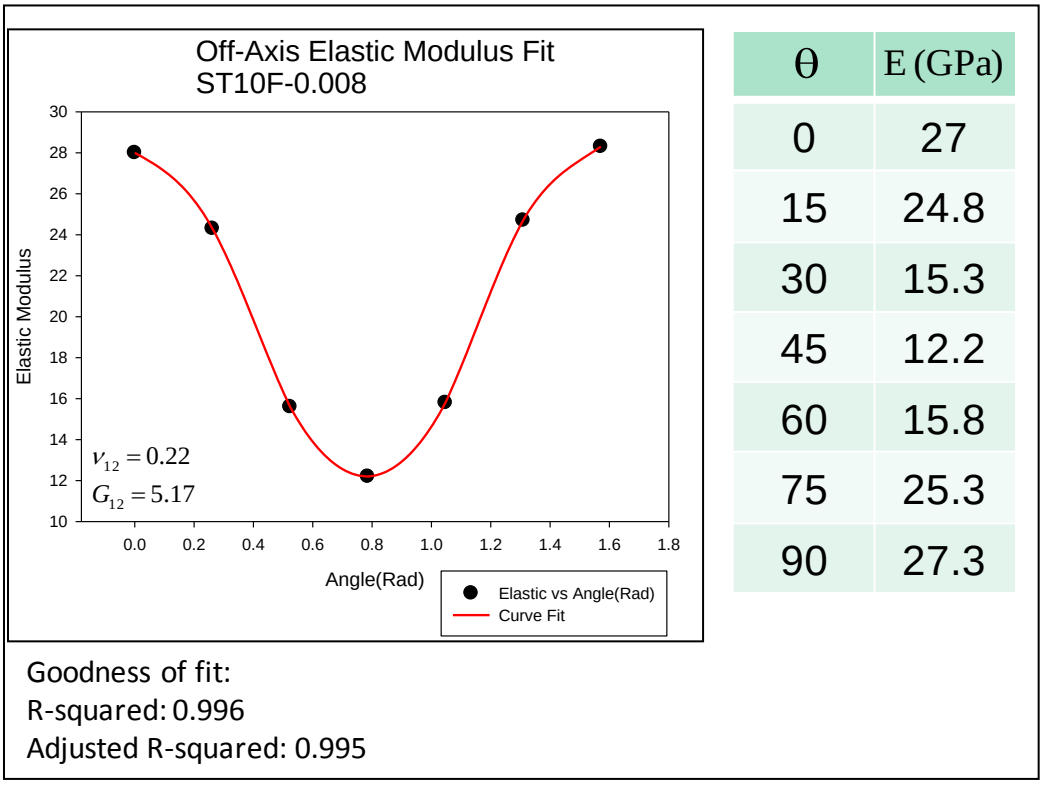

θ	E (GPa)
0	27
15	24.8
30	15.3
45	12.2
60	15.8
75	25.3
90	27.3

Goodness of fit:
R-squared: 0.996
Adjusted R-squared: 0.995

Figure 151. ST10F-0.008 Elastic Modulus versus Off-Axis Angle Curve Fitting Plot

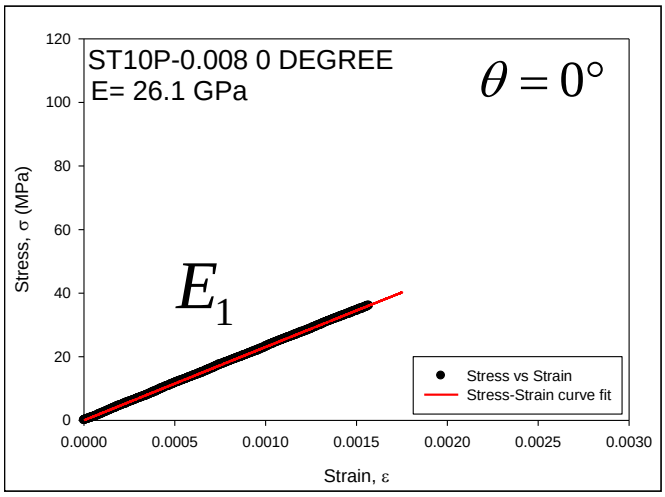

Figure 152. ST10P-0.008 0-Degree Elastic Modulus

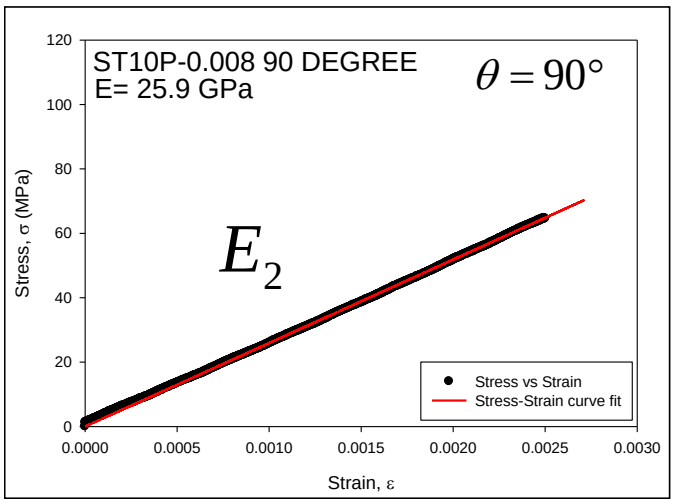

Figure 153. ST10P-0.008 90-Degree Elastic Modulus

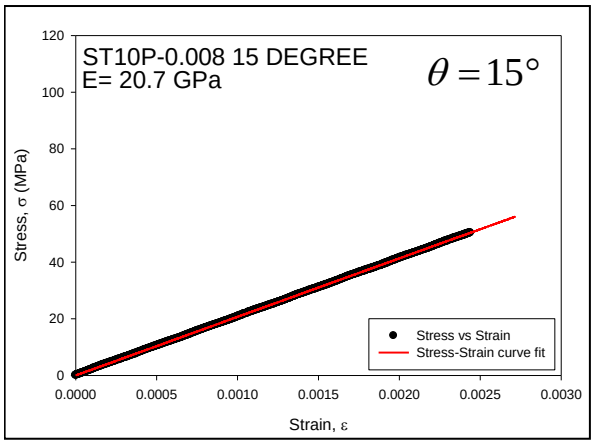

Figure 154. ST10P-0.008 15-Degree Elastic Modulus

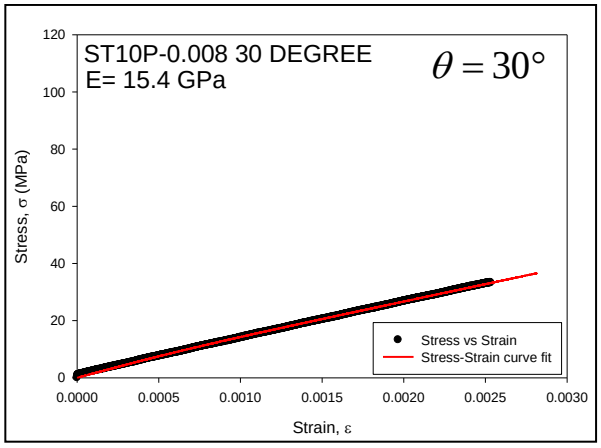

Figure 155. ST10P-0.008 30-Degree Elastic Modulus

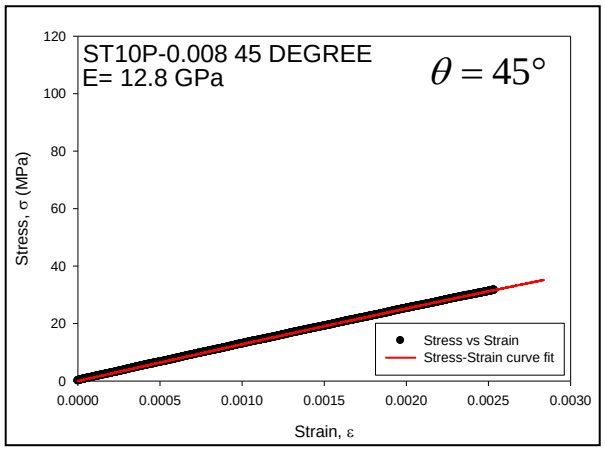

Figure 156. ST10P-0.008 45-Degree Elastic Modulus

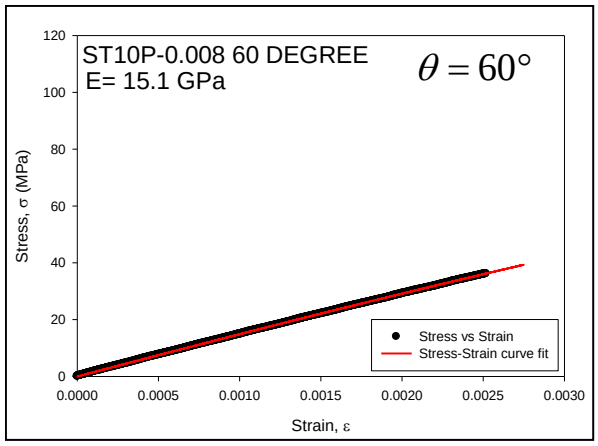

Figure 157. ST10P-0.008 60-Degree Elastic Modulus

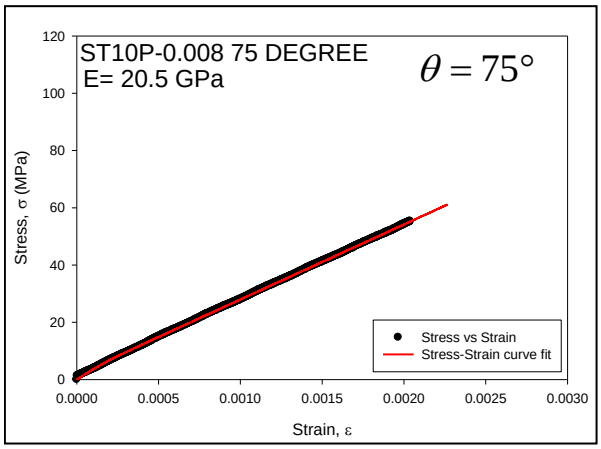

Figure 158. ST10P-0.008 75-Degree Elastic Modulus

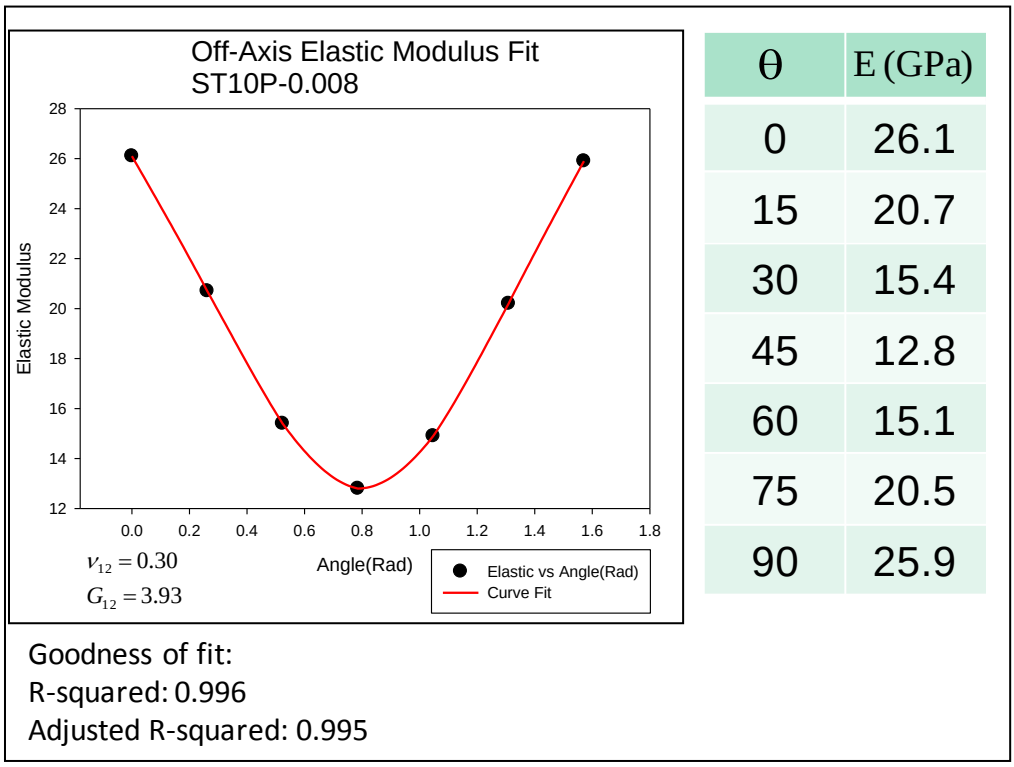

θ	E (GPa)
0	26.1
15	20.7
30	15.4
45	12.8
60	15.1
75	20.5
90	25.9

Goodness of fit:
R-squared: 0.996
Adjusted R-squared: 0.995

Figure 159. ST10P-0.008 Elastic Modulus versus Off-Axis Angle Curve Fitting Plot

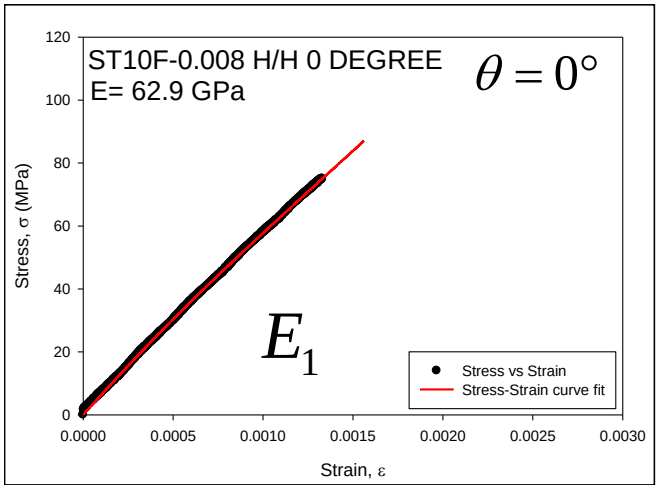

Figure 160. ST10F-0.008 H/H 0-Degree Elastic Modulus

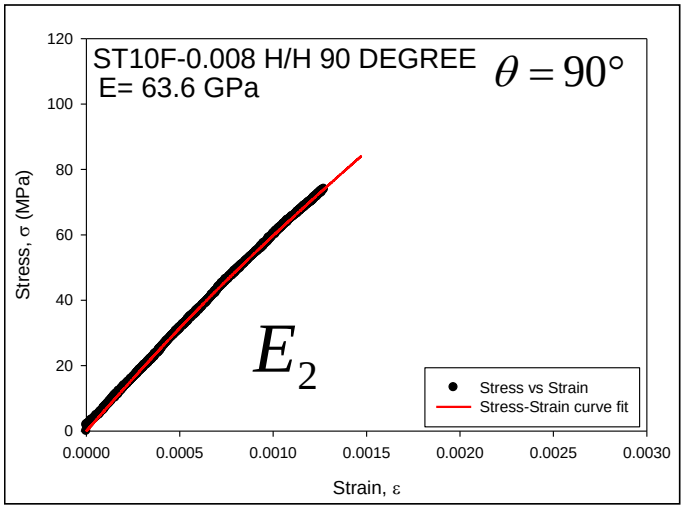

Figure 161. ST10F-0.008 H/H 90-Degree Elastic Modulus

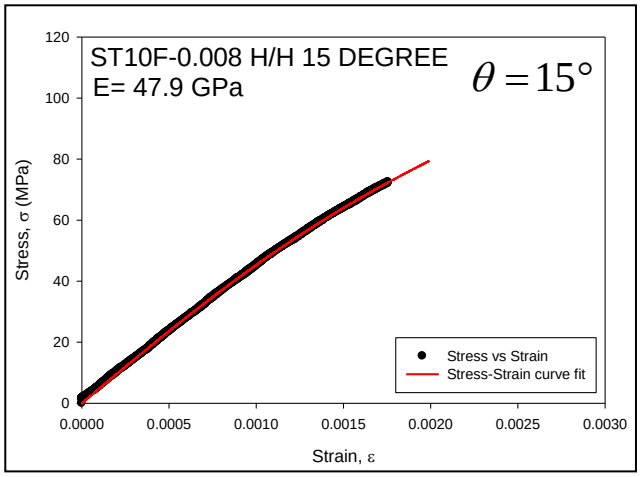

Figure 162. ST10F-0.008 H/H 15-Degree Elastic Modulus

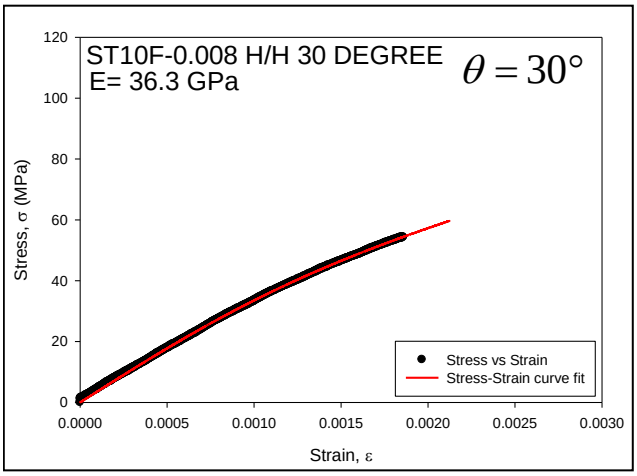

Figure 163. ST10F-0.008 H/H 30-Degree Elastic Modulus

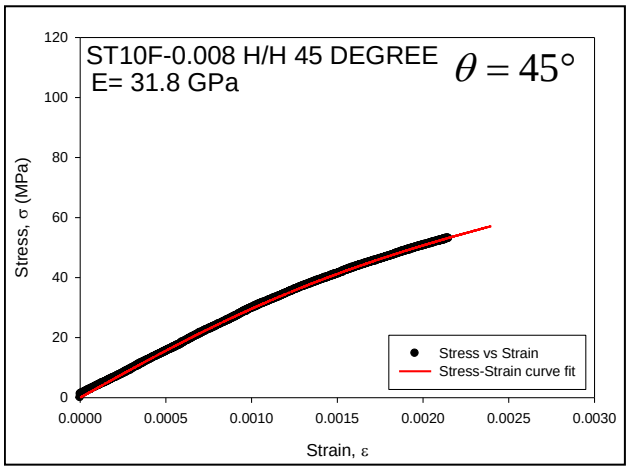

Figure 164. ST10F-0.008 H/H 45-Degree Elastic Modulus

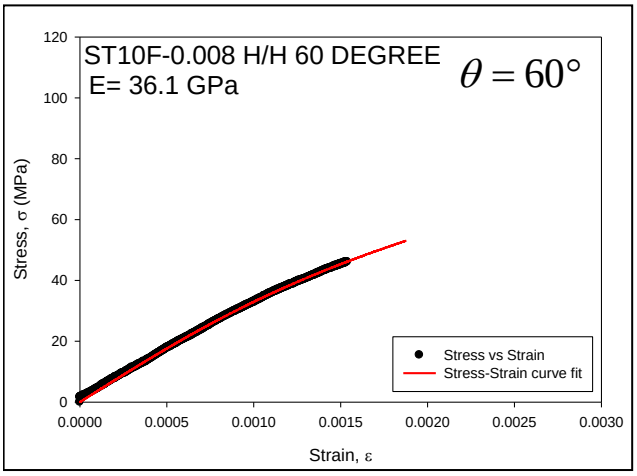

Figure 165. ST10F-0.008 H/H 60-Degree Elastic Modulus

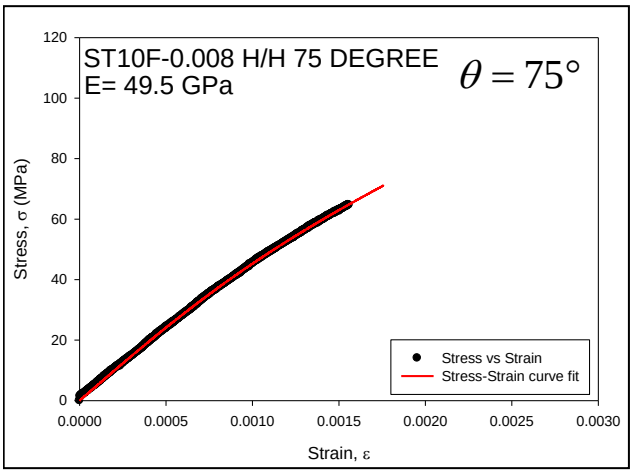

Figure 166. ST10F-0.008 H/H 75-Degree Elastic Modulus

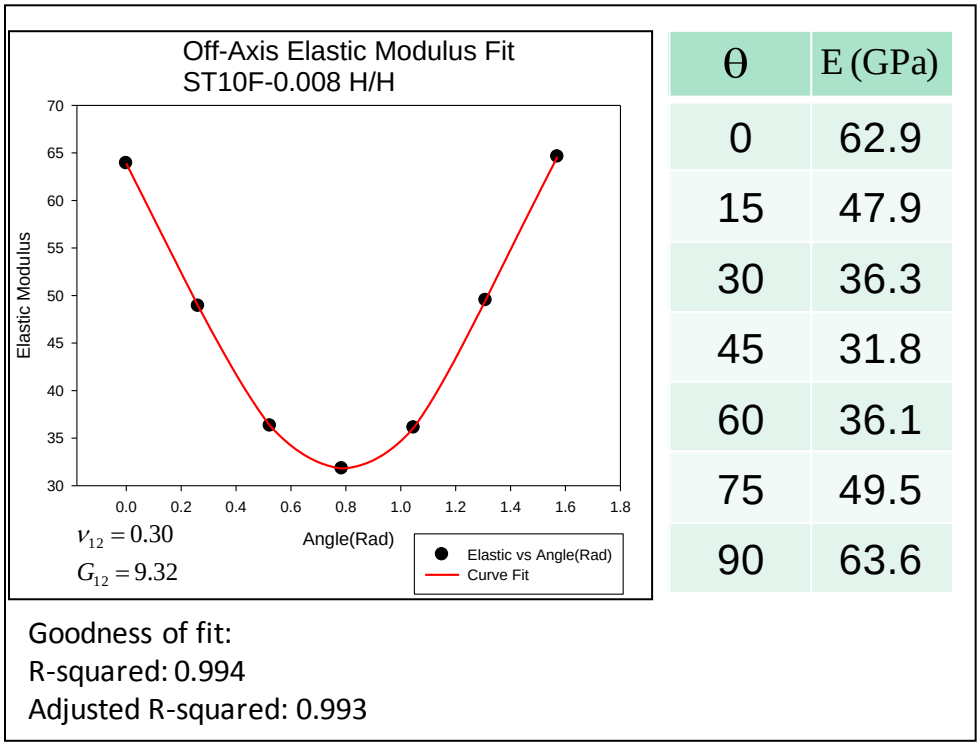

θ	E (GPa)
0	62.9
15	47.9
30	36.3
45	31.8
60	36.1
75	49.5
90	63.6

Figure 167. ST10F-0.008 H/H Elastic Modulus versus Off-Axis Angle Curve Fitting Plot

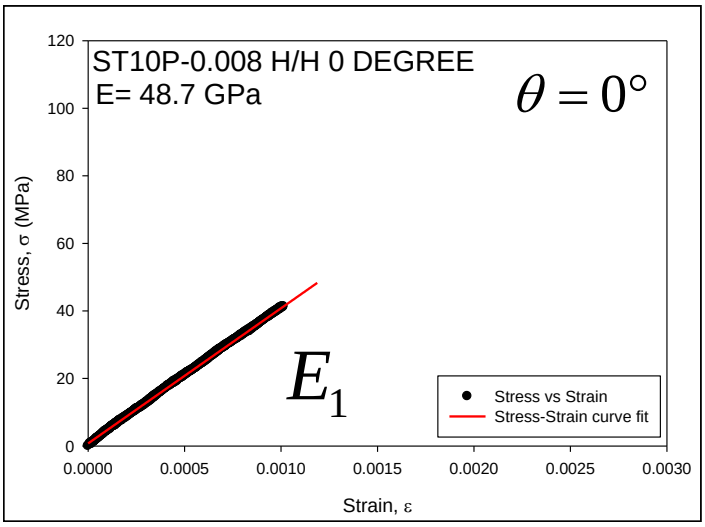

Figure 168. ST10P-0.008 H/H 0-Degree Elastic Modulus

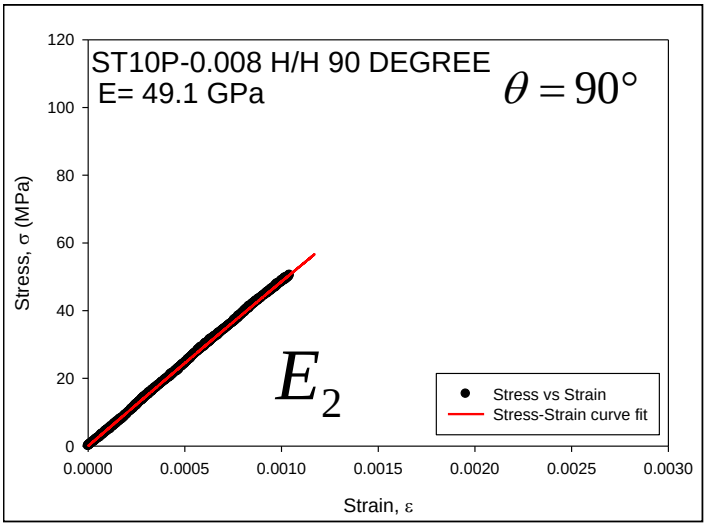

Figure 169. ST10P-0.008 H/H 90-Degree Elastic Modulus

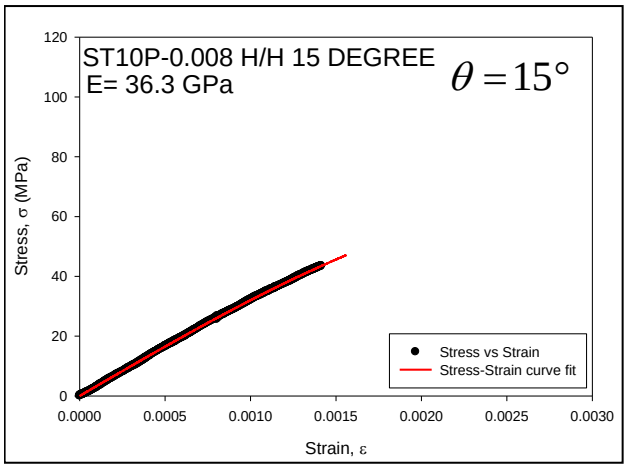

Figure 170. ST10P-0.008 H/H 15-Degree Elastic Modulus

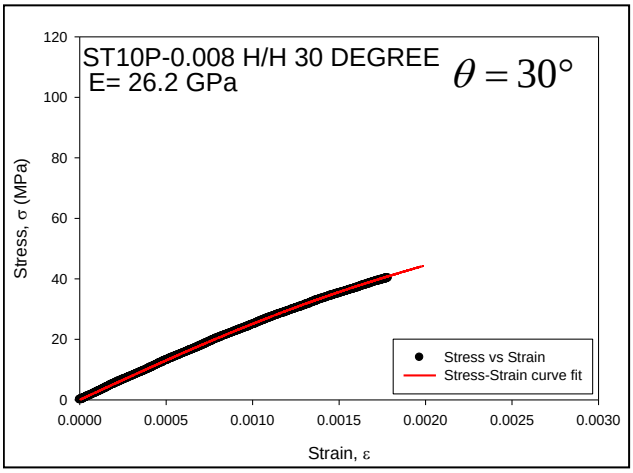

Figure 171. ST10P-0.008 H/H 30-Degree Elastic Modulus

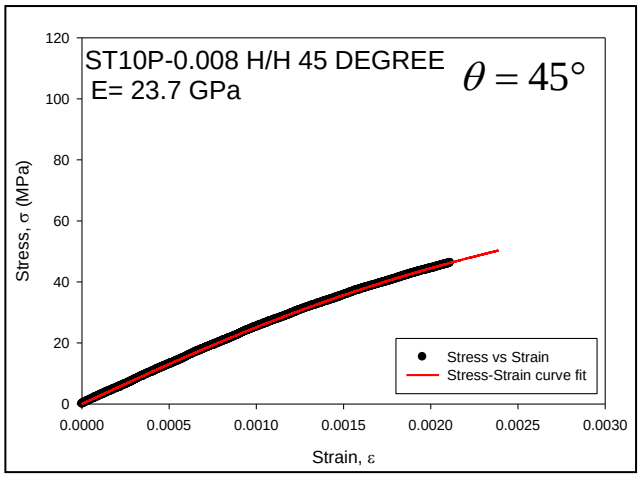

Figure 172. ST10P-0.008 H/H 45-Degree Elastic Modulus

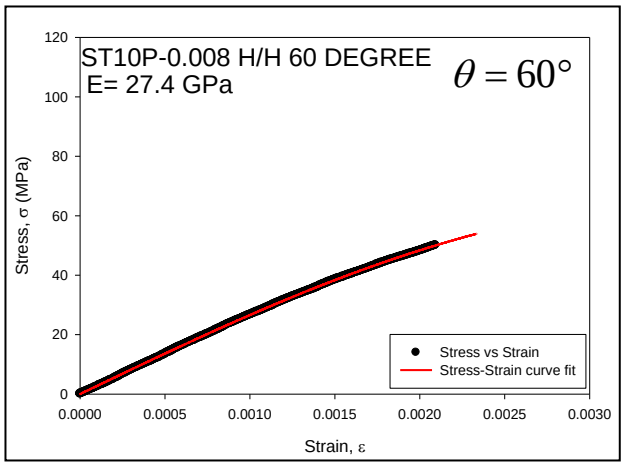

Figure 173. ST10P-0.008 H/H 60-Degree Elastic Modulus

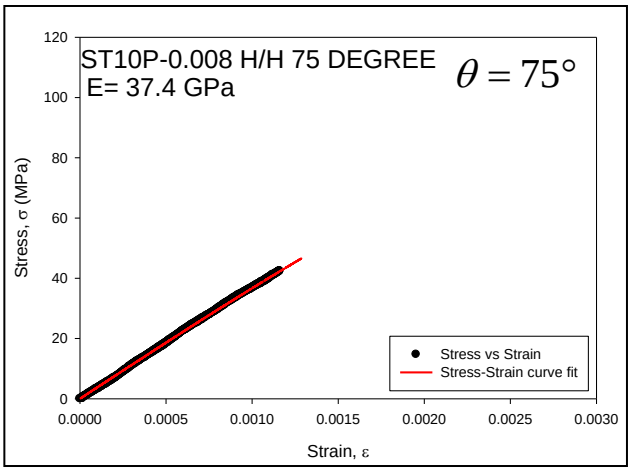

Figure 174. ST10P-0.008 H/H 75-Degree Elastic Modulus

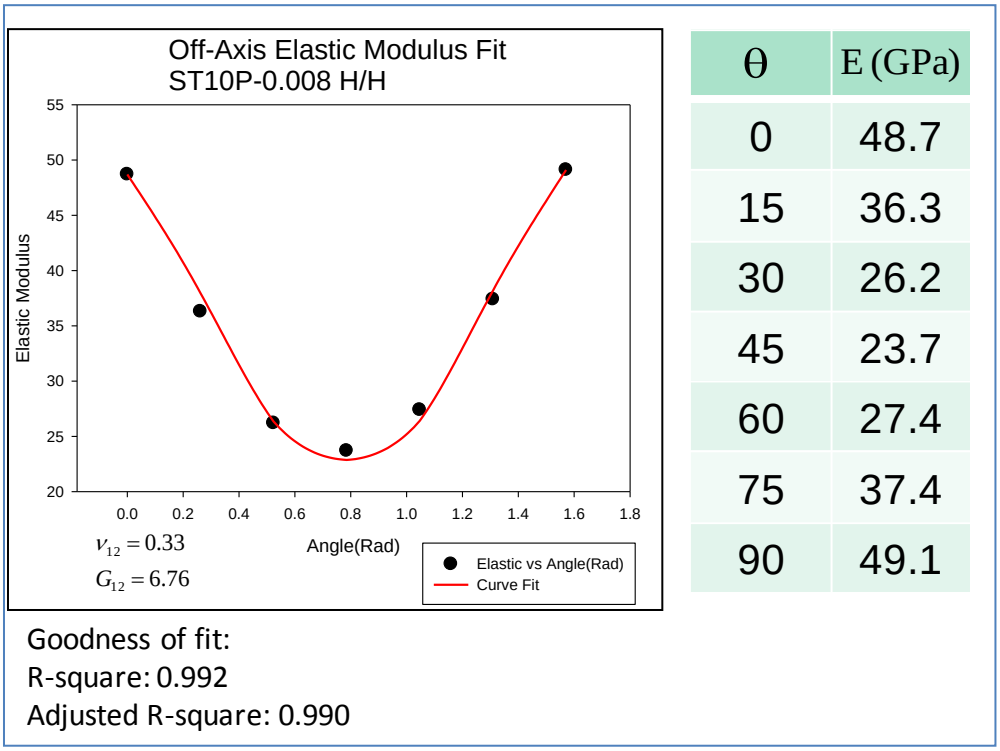

θ	E (GPa)
0	48.7
15	36.3
30	26.2
45	23.7
60	27.4
75	37.4
90	49.1

Goodness of fit:
R-square: 0.992
Adjusted R-square: 0.990

Figure 175. ST10P-0.008 H/H Elastic Modulus versus Off-Axis Angle Curve Fitting Plot

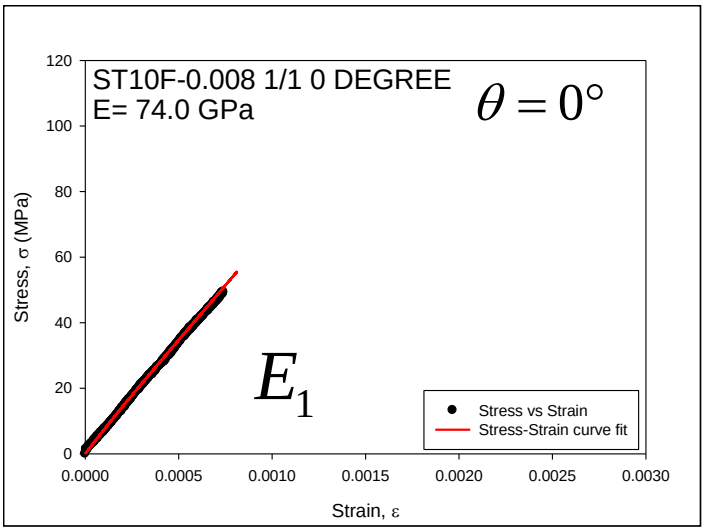

Figure 176. ST10F-0.008 1/1 0-Degree Elastic Modulus

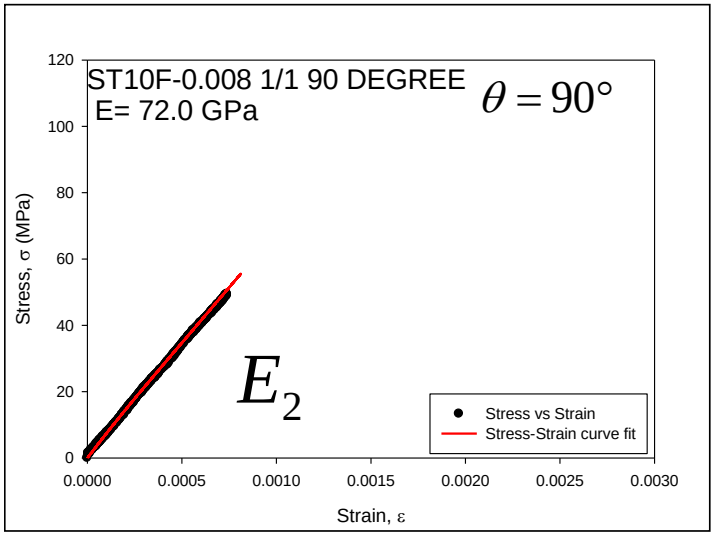

Figure 177. ST10F-0.008 1/1 90-Degree Elastic Modulus

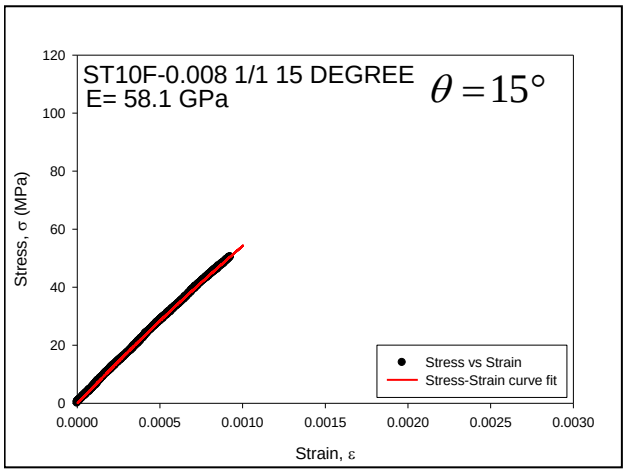

Figure 178. ST10F-0.008 1/1 15-Degree Elastic Modulus

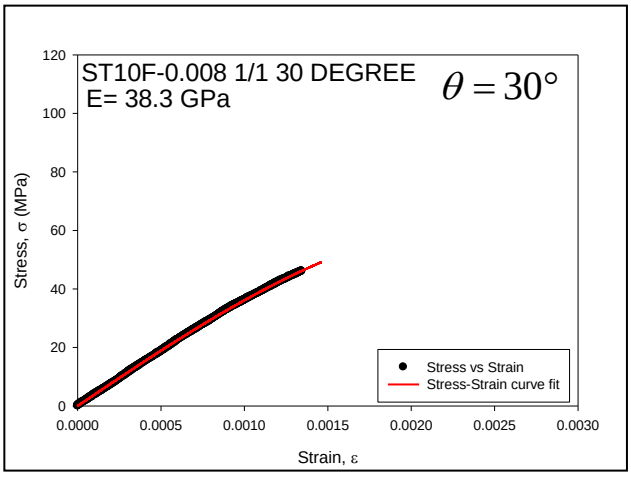

Figure 179. ST10F-0.008 1/1 30-Degree Elastic Modulus

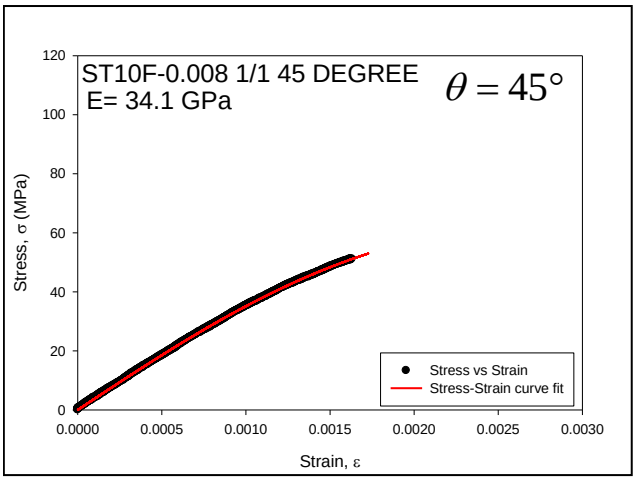

Figure 180. ST10F-0.008 1/1 45-Degree Elastic Modulus

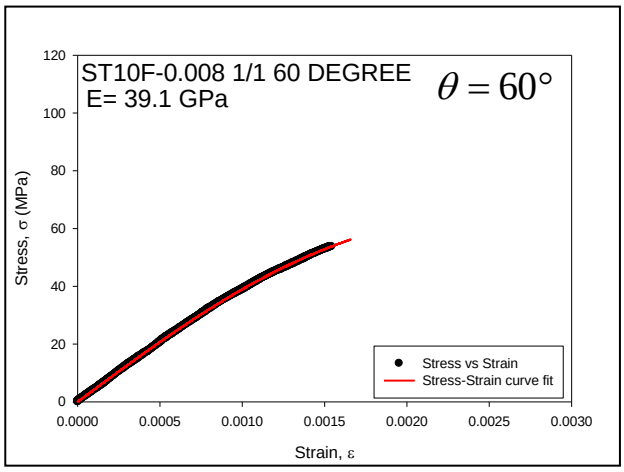

Figure 181. ST10F-0.008 1/1 60-Degree Elastic Modulus

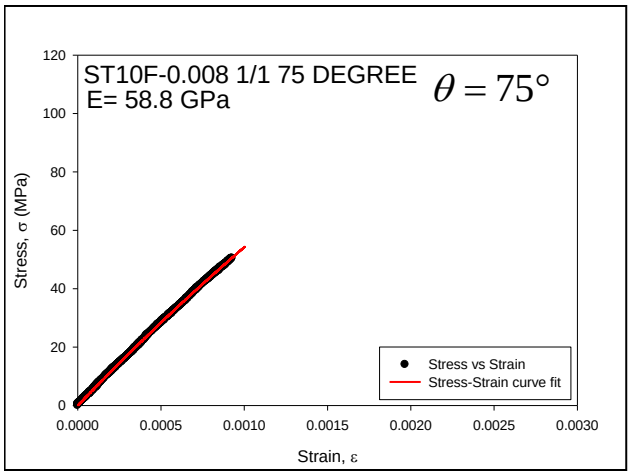

Figure 182. ST10F-0.008 1/1 75-Degree Elastic Modulus

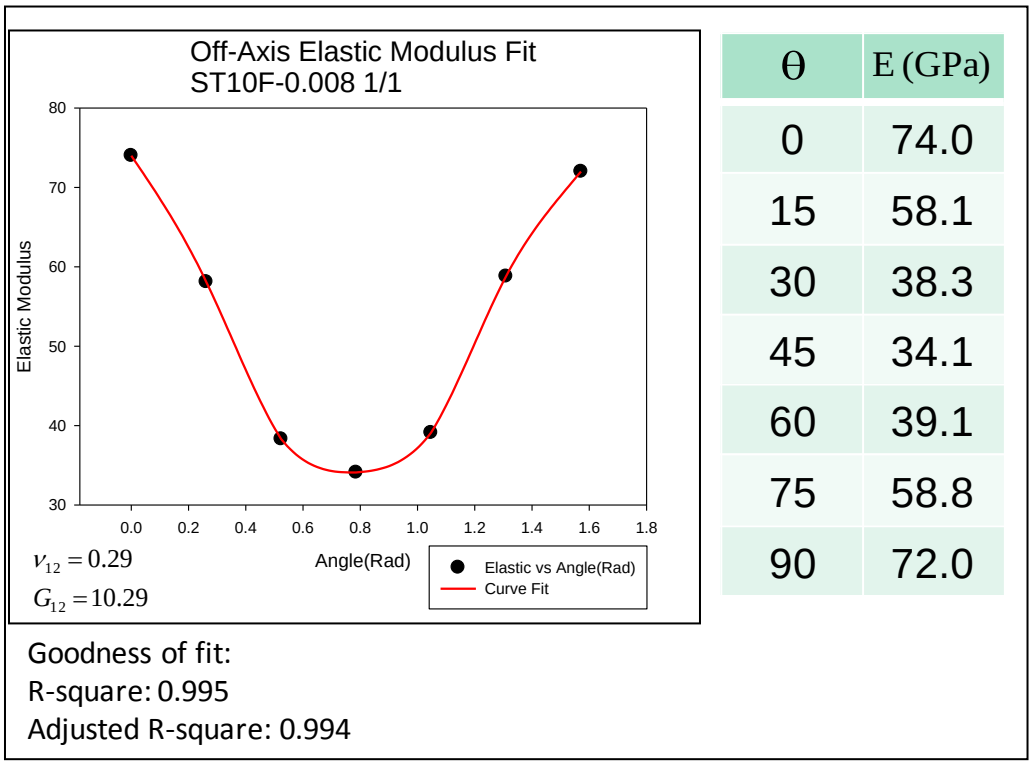

θ	E (GPa)
0	74.0
15	58.1
30	38.3
45	34.1
60	39.1
75	58.8
90	72.0

Goodness of fit:
R-square: 0.995
Adjusted R-square: 0.994

Figure 183. ST10F-0.008 1/1 Elastic Modulus versus Off-Axis Angle Curve Fitting Plot

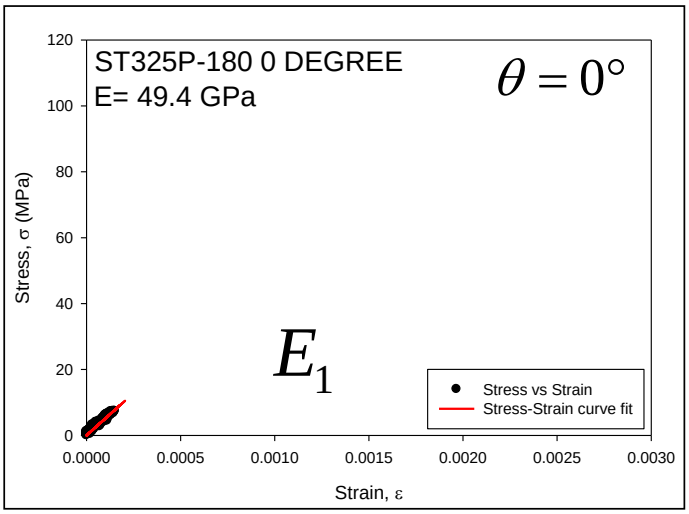

Figure 184. ST325P-180 0-Degree Elastic Modulus

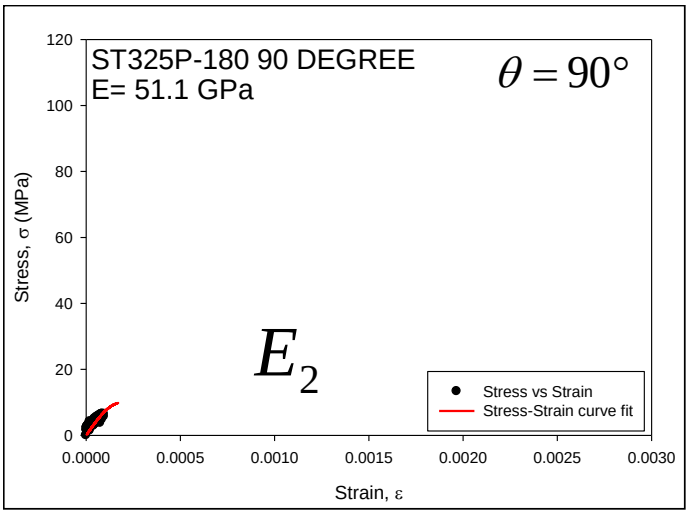

Figure 185. ST325P-180 90-Degree Elastic Modulus

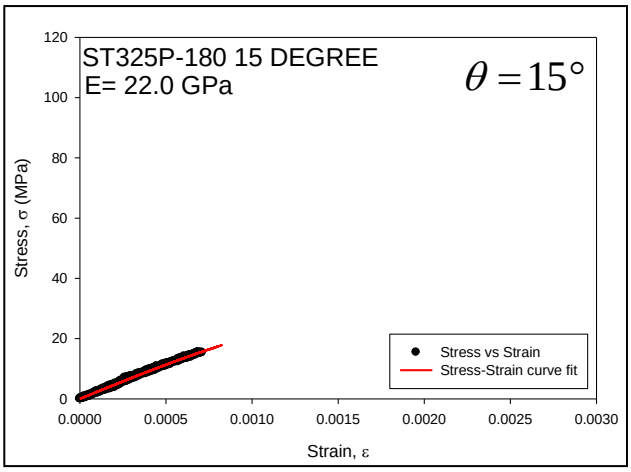

Figure 186. ST325P-180 15-Degree Elastic Modulus

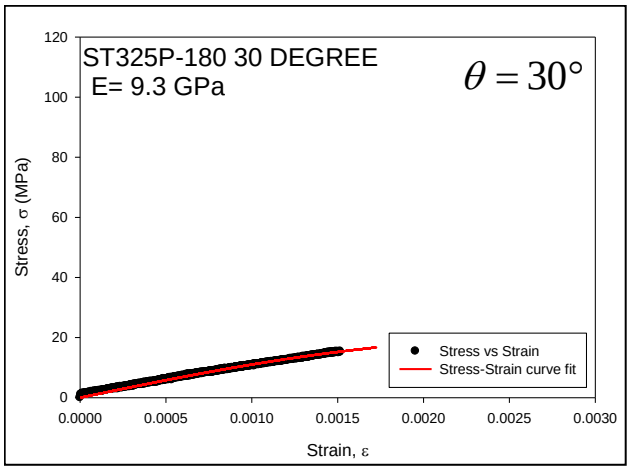

Figure 187. ST325P-180 30-Degree Elastic Modulus

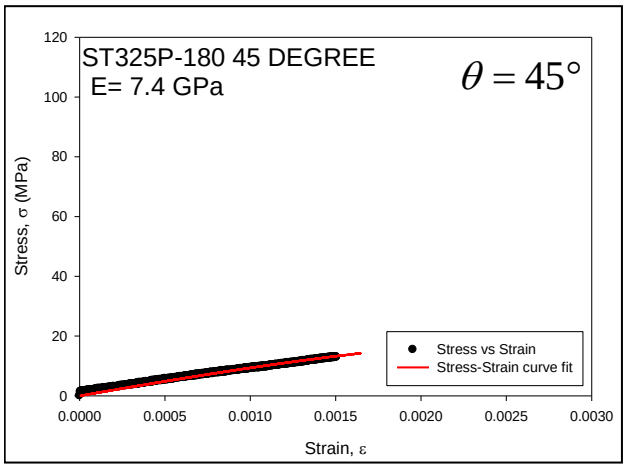

Figure 188. ST325P-180 45-Degree Elastic Modulus

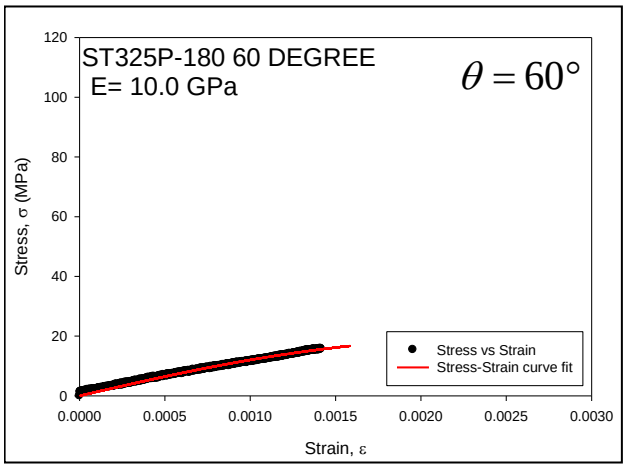

Figure 189. ST325P-180 60-Degree Elastic Modulus

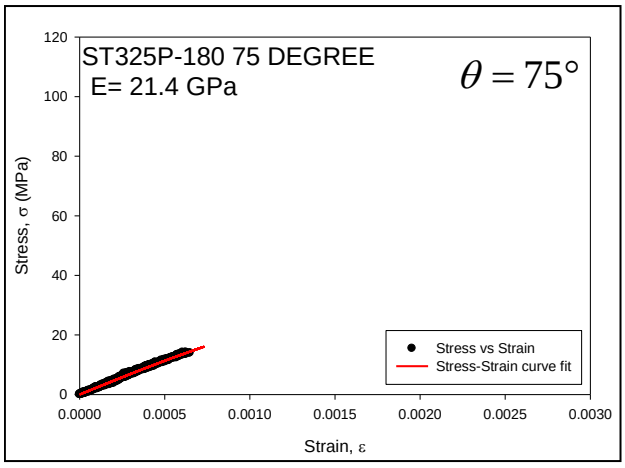

Figure 190. ST325P-180 75-Degree Elastic Modulus

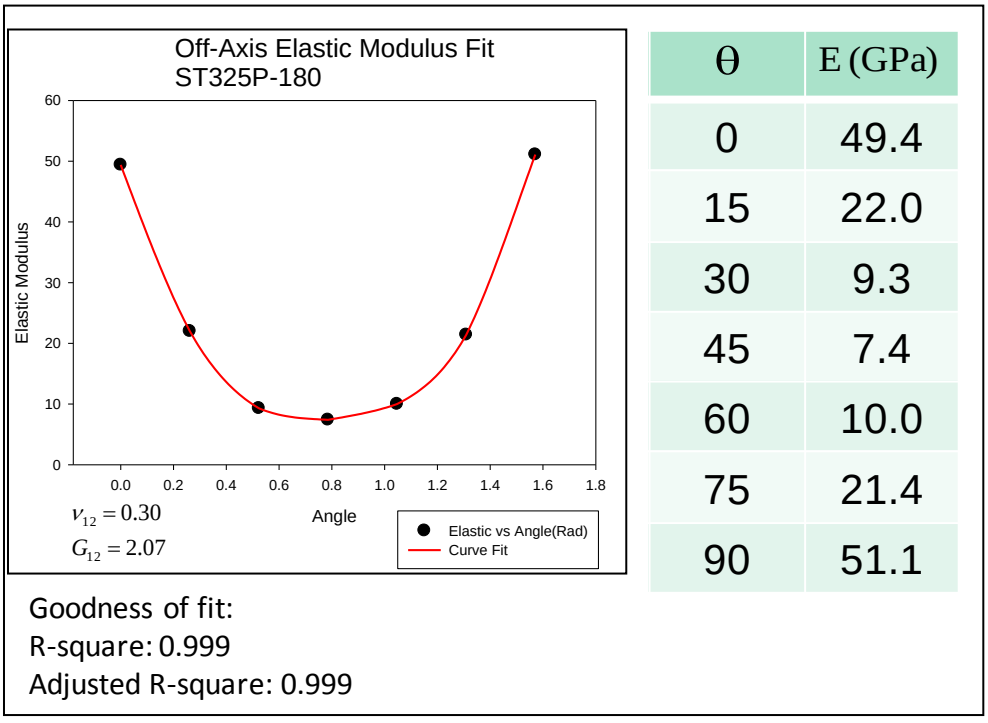

θ	E (GPa)
0	49.4
15	22.0
30	9.3
45	7.4
60	10.0
75	21.4
90	51.1

Goodness of fit:
R-square: 0.999
Adjusted R-square: 0.999

Figure 191. ST325P-180 Elastic Modulus versus Off-Axis Angle Curve Fitting Plot

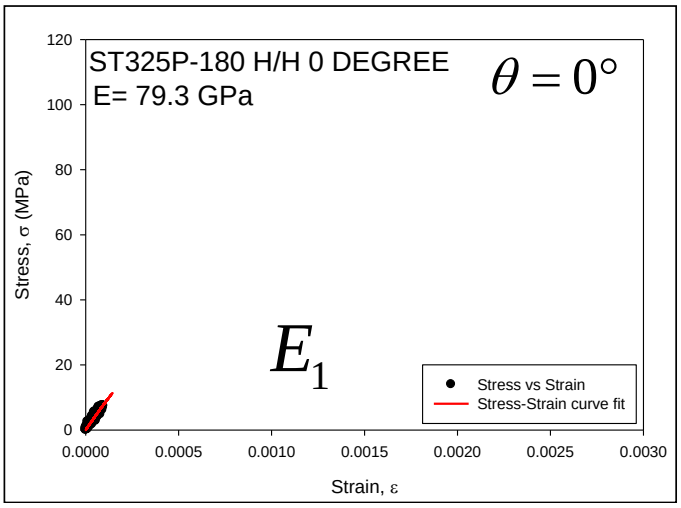

Figure 192. ST325P-180 H/H 0-Degree Elastic Modulus

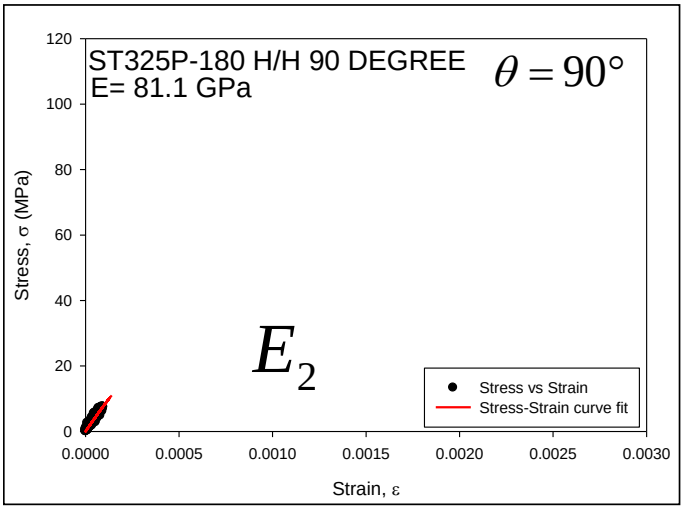

Figure 193. ST325P-180 H/H 90-Degree Elastic Modulus

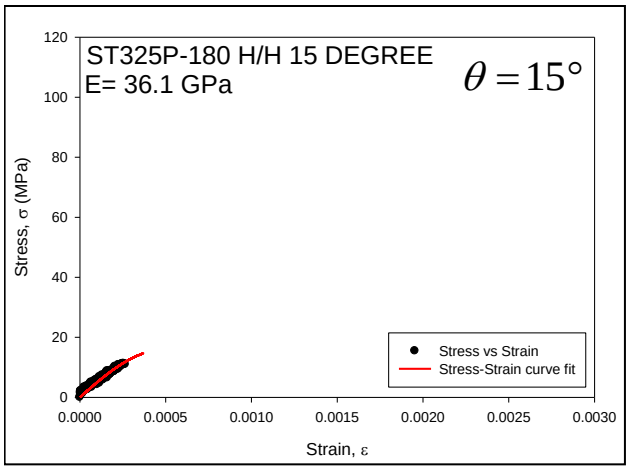

Figure 194. ST325P-180 H/H 15-Degree Elastic Modulus

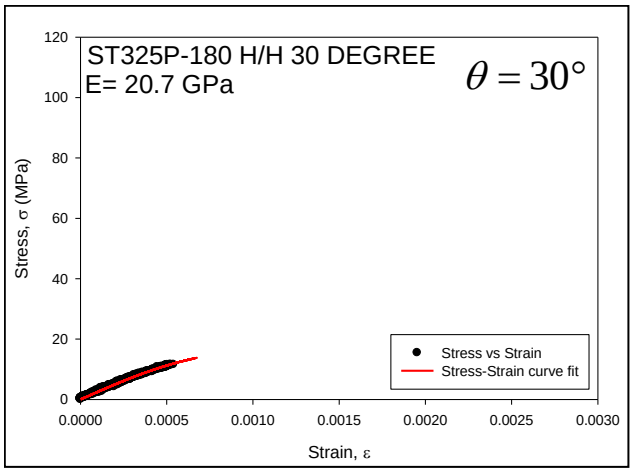

Figure 195. ST325P-180 H/H 30-Degree Elastic Modulus

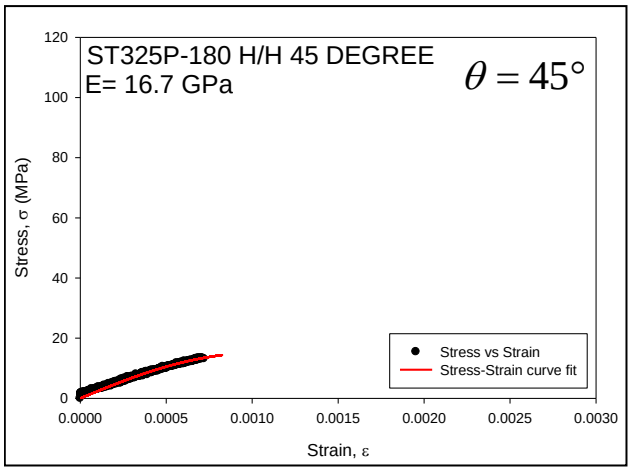

Figure 196. ST325P-180 H/H 45-Degree Elastic Modulus

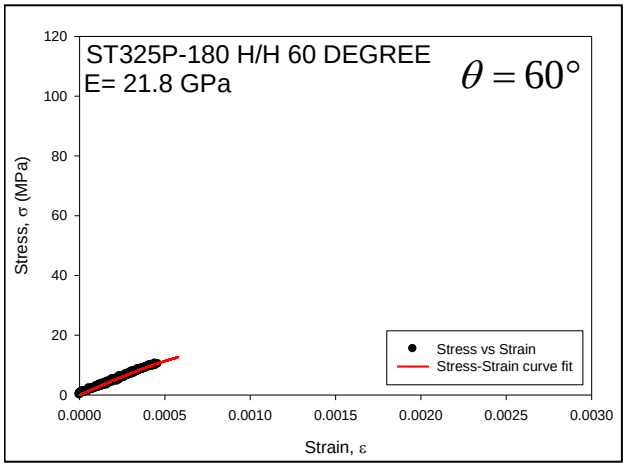

Figure 197. ST325P-180 H/H 60-Degree Elastic Modulus

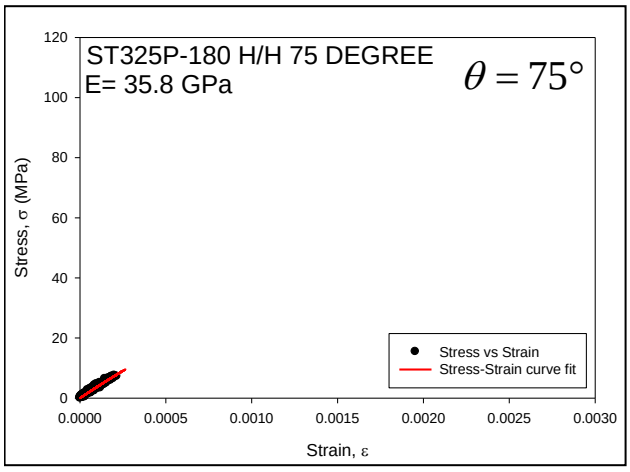

Figure 198. ST325P-180 H/H 75-Degree Elastic Modulus

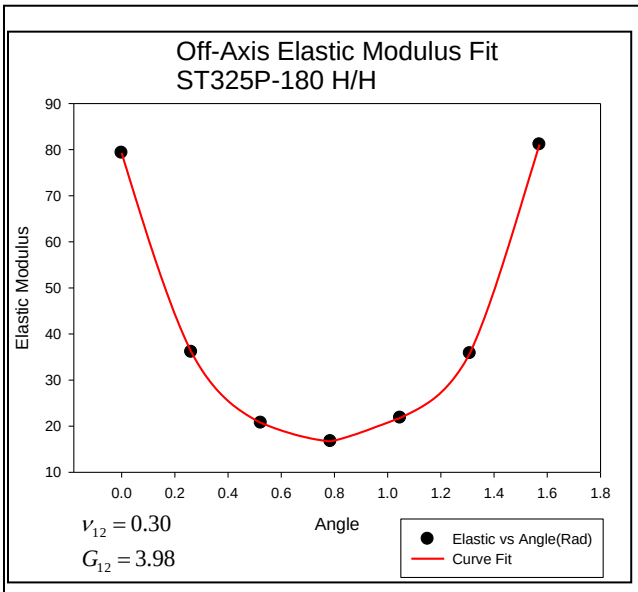

θ	E (GPa)
0	79.3
15	36.1
30	20.7
45	16.7
60	21.8
75	35.8
90	81.1

Goodness of fit:
R-square: 0.9938
Adjusted R-square: 0.9926

Figure 199. ST325P-180 H/H Elastic Modulus versus Off-Axis Angle Curve Fitting Plot

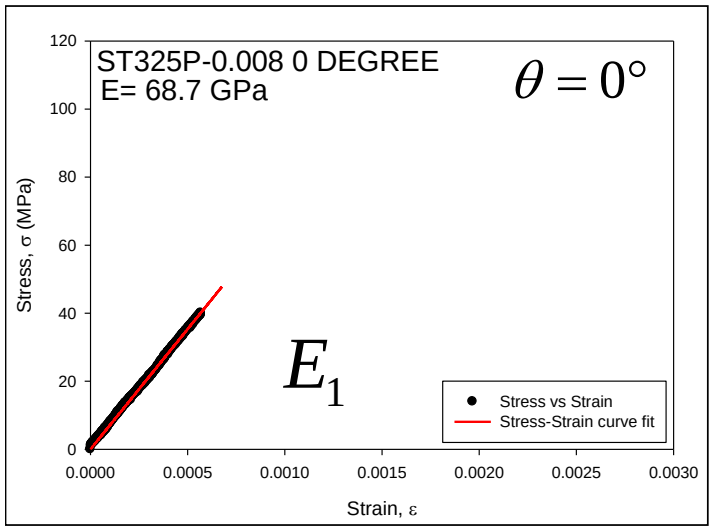

Figure 200. ST325P-0.008 0-Degree Elastic Modulus

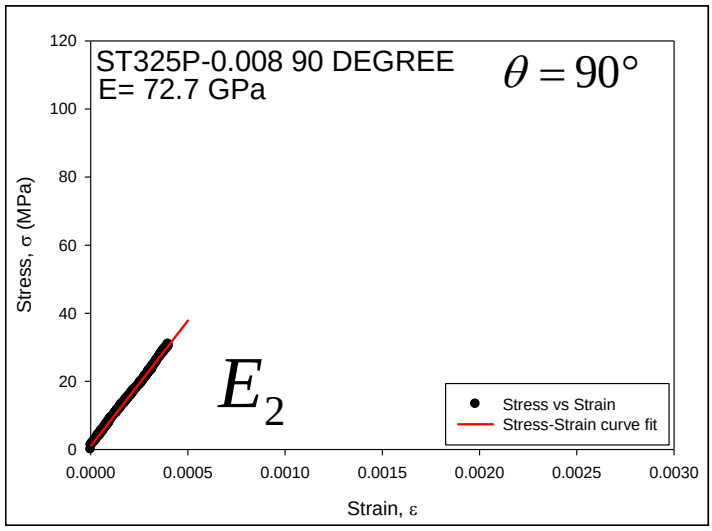

Figure 201. ST325P-0.008 90-Degree Elastic Modulus

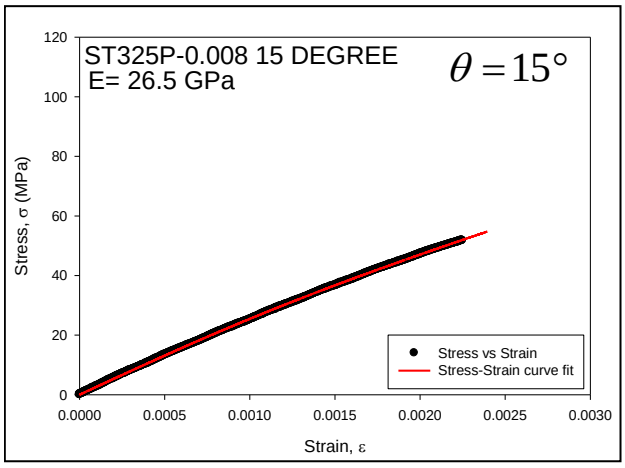

Figure 202. ST325P-0.008 15-Degree Elastic Modulus

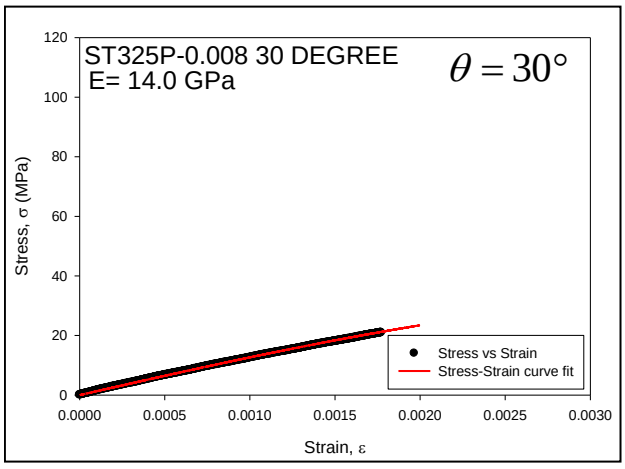

Figure 203. ST325P-0.008 30-Degree Elastic Modulus

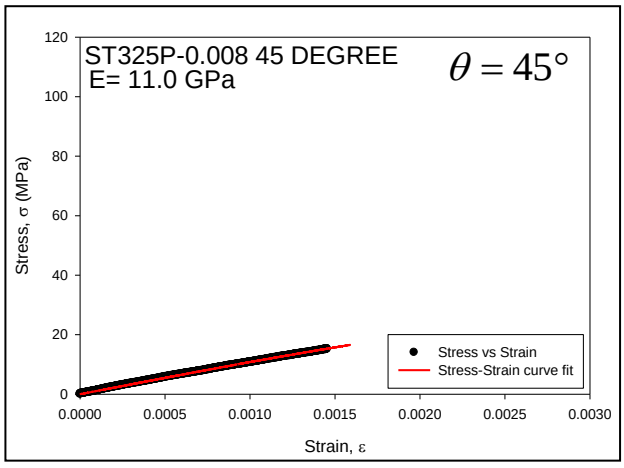

Figure 204. ST325P-0.008 45-Degree Elastic Modulus

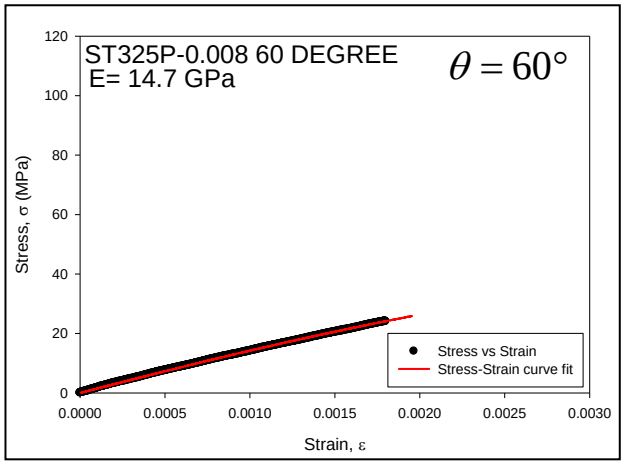

Figure 205. ST325P-0.008 60-Degree Elastic Modulus

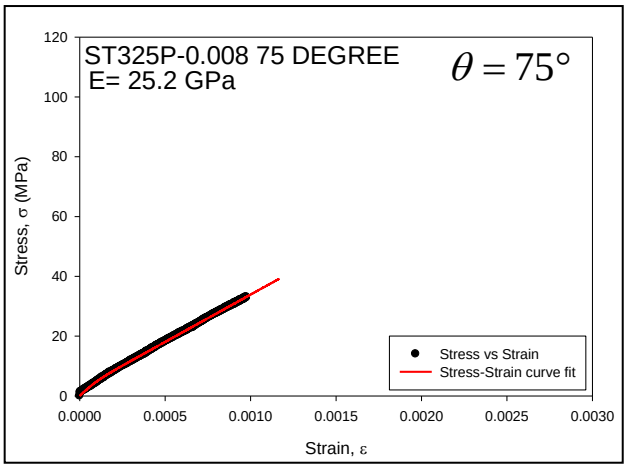

Figure 206. ST325P-0.008 75-Degree Elastic Modulus

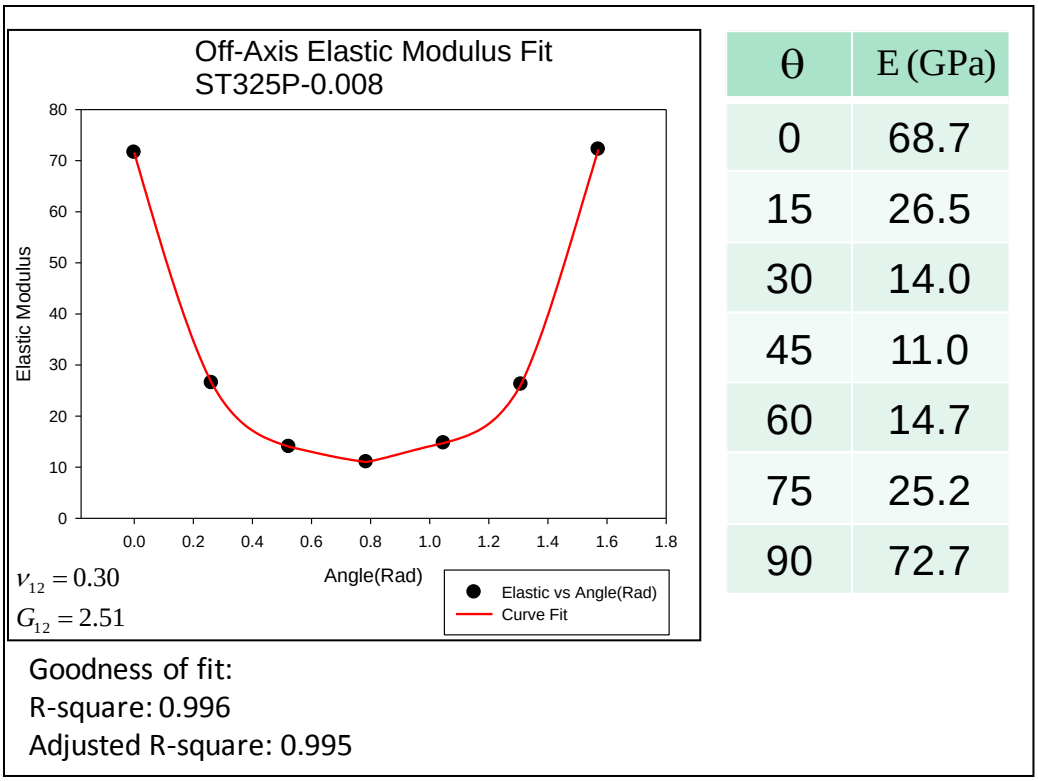

θ	E (GPa)
0	68.7
15	26.5
30	14.0
45	11.0
60	14.7
75	25.2
90	72.7

Figure 207. ST325P-0.008 Elastic Modulus versus Off-Axis Angle Curve Fitting Plot

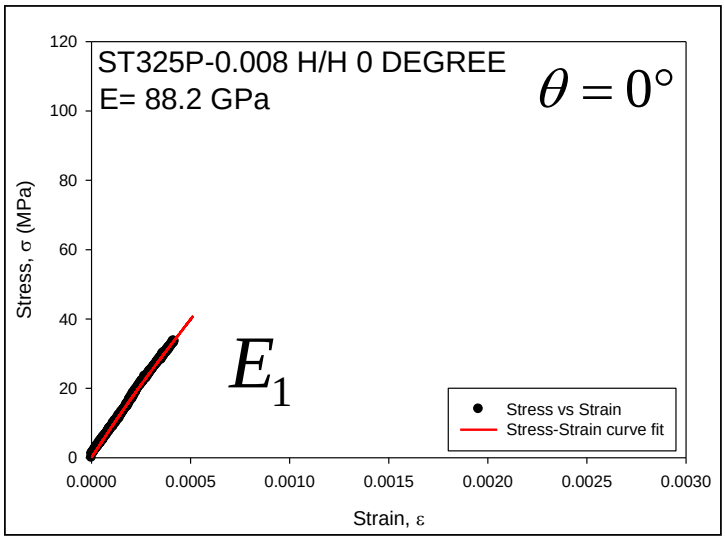

Figure 208. ST325P-0.008 H/H 0-Degree Elastic Modulus

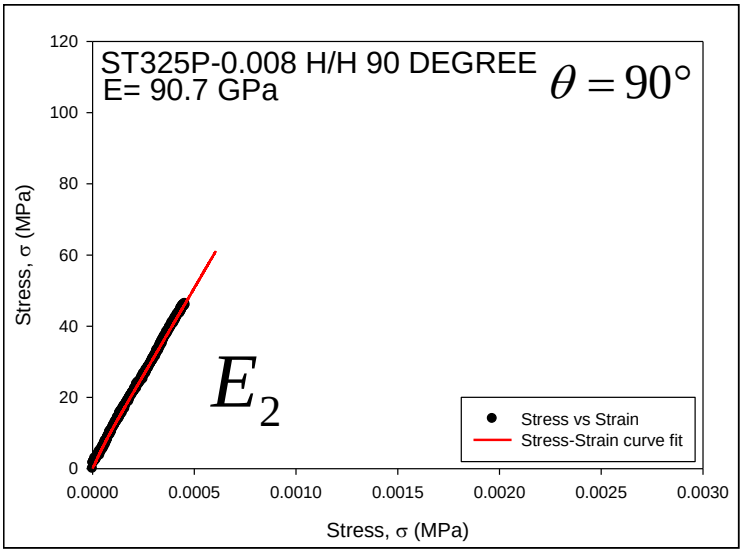

Figure 209. ST325P-0.008 H/H 90-Degree Elastic Modulus

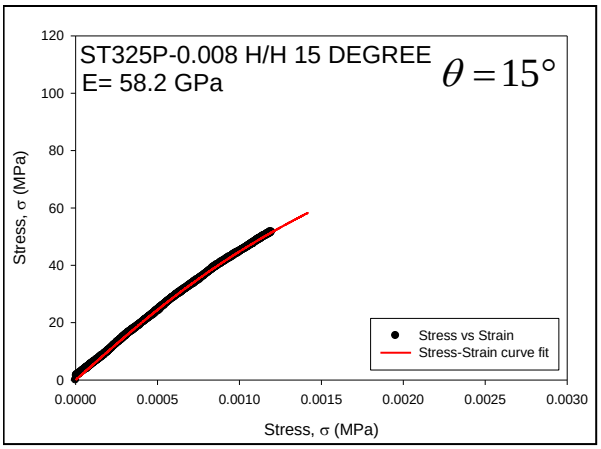

Figure 210. ST325P-0.008 H/H 15-Degree Elastic Modulus

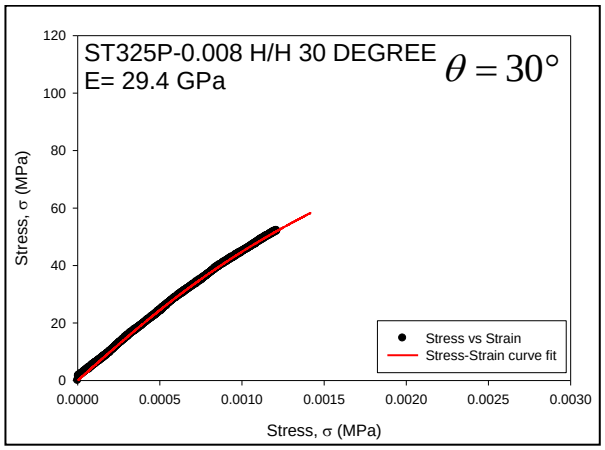

Figure 211. ST325P-0.008 H/H 30-Degree Elastic Modulus

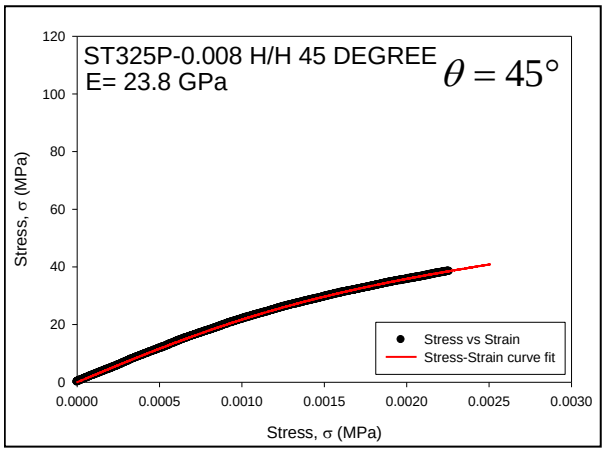

Figure 212. ST325P-0.008 H/H 45-Degree Elastic Modulus

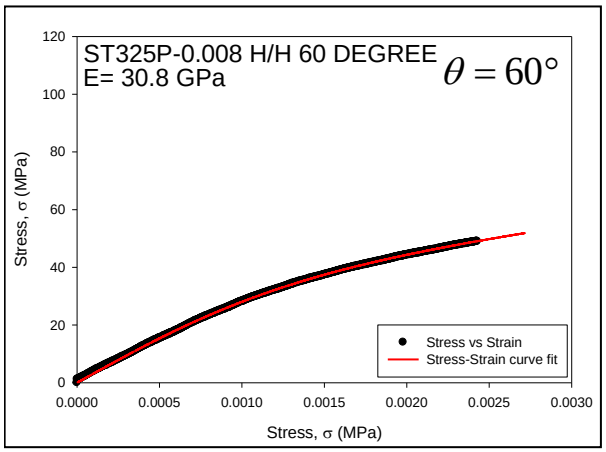

Figure 213. ST325P-0.008 H/H 60-Degree Elastic Modulus

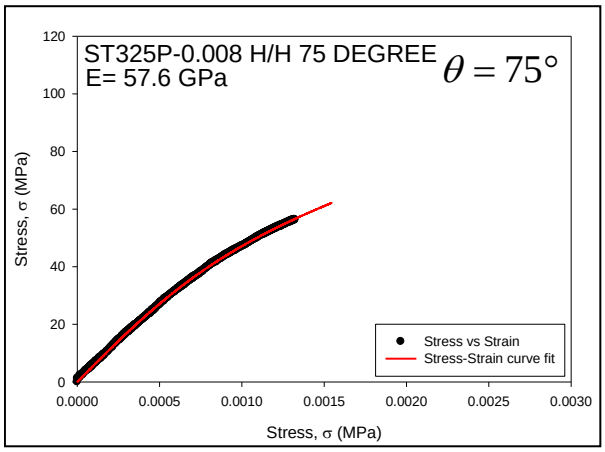

Figure 214. ST325P-0.008 H/H 75-Degree Elastic Modulus

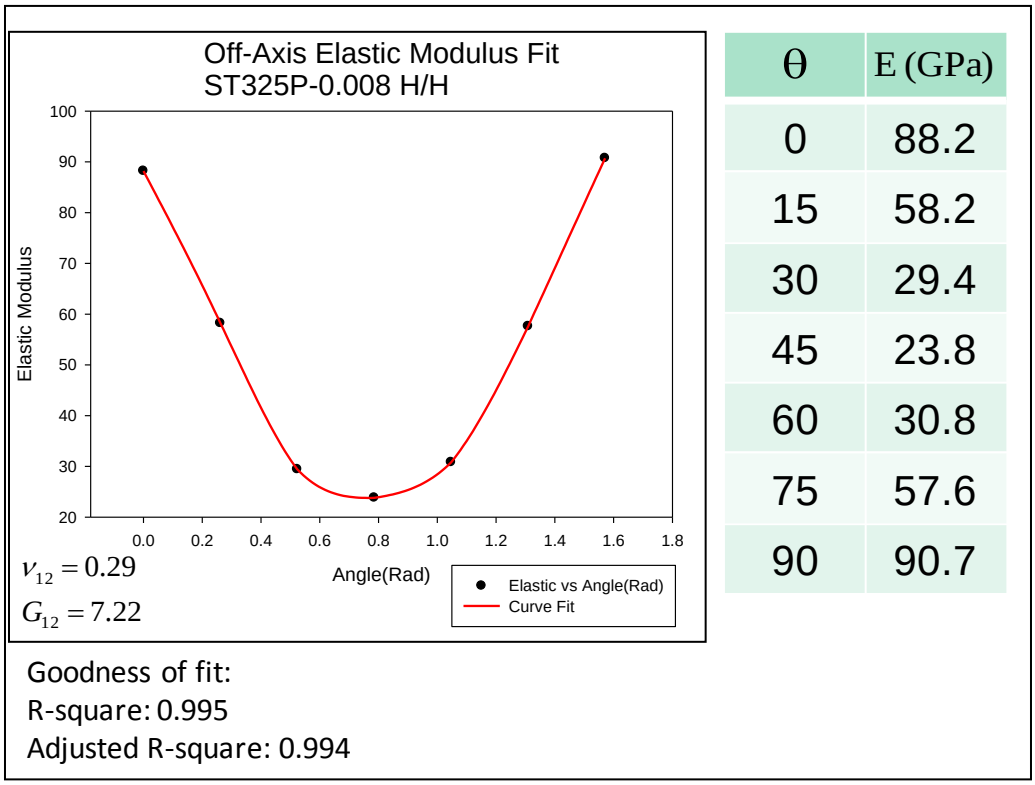

θ	E (GPa)
0	88.2
15	58.2
30	29.4
45	23.8
60	30.8
75	57.6
90	90.7

Figure 215. ST325P-0.008 H/H Elastic Modulus versus Off-Axis Angle Curve Fitting Plot

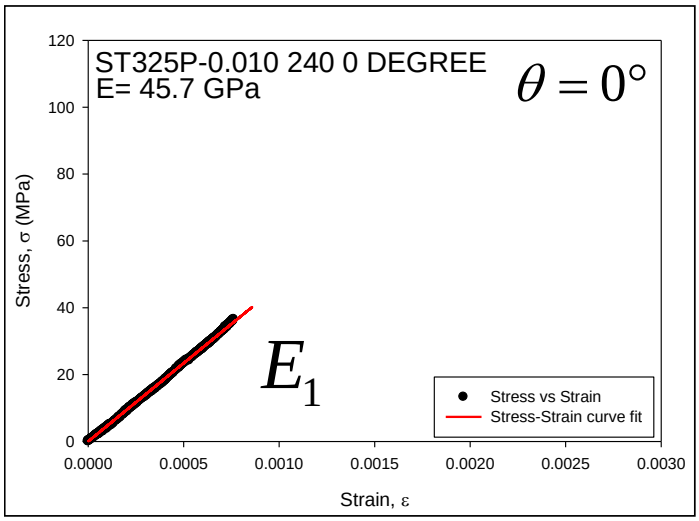

Figure 216. ST325P-0.010 240 0-Degree Elastic Modulus

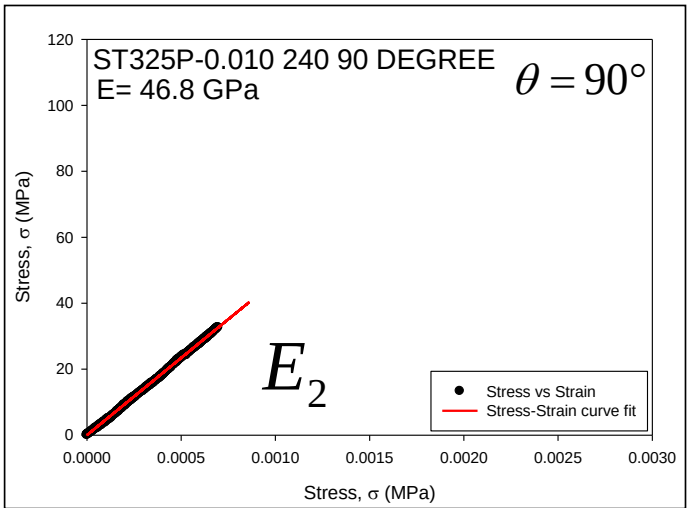

Figure 217. ST325P-0.010 240 90-Degree Elastic Modulus

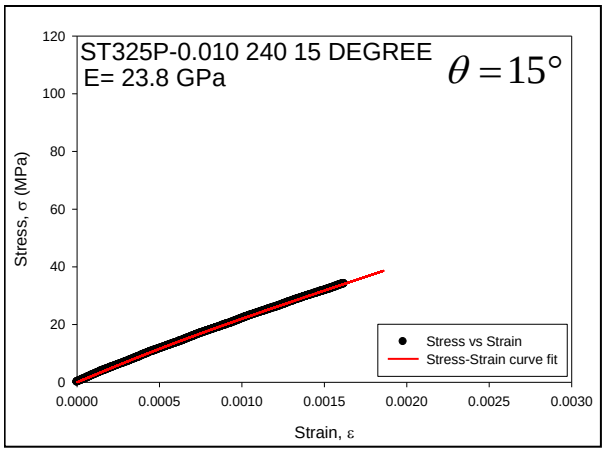

Figure 218. ST325P-0.010 240 15-Degree Elastic Modulus

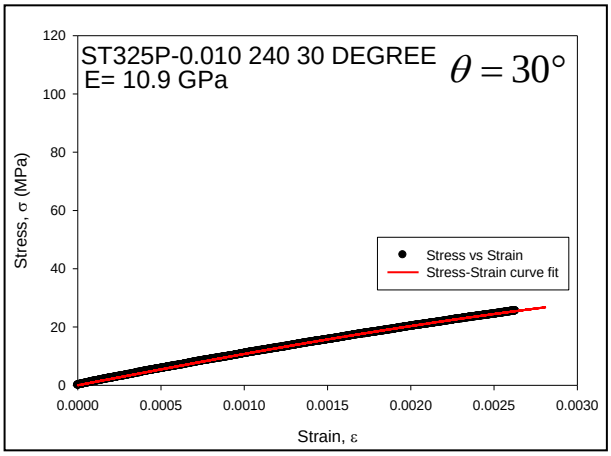

Figure 219. ST325P-0.010 240 30-Degree Elastic Modulus

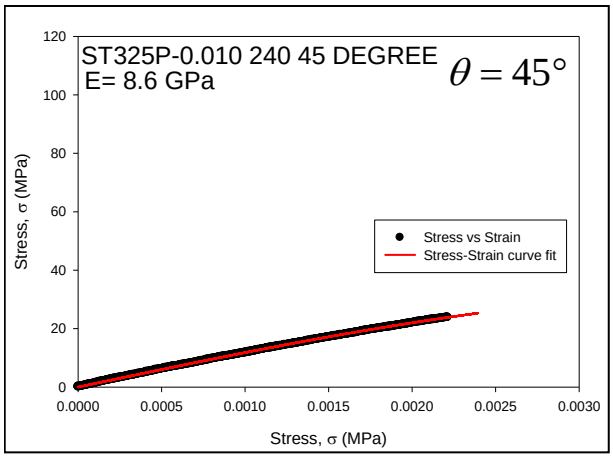

Figure 220. ST325P-0.010 240 45-Degree Elastic Modulus

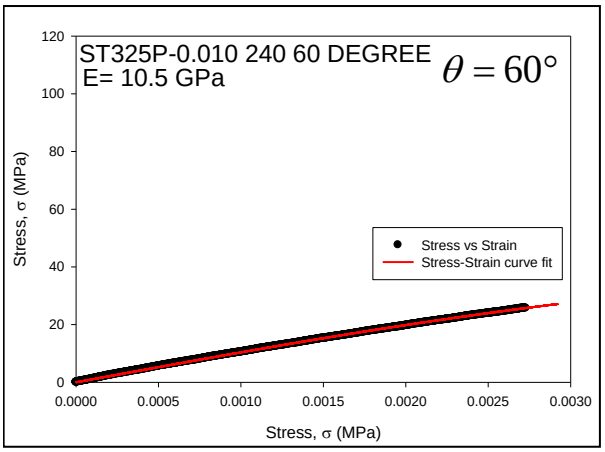

Figure 221. ST325P-0.010 240 60-Degree Elastic Modulus

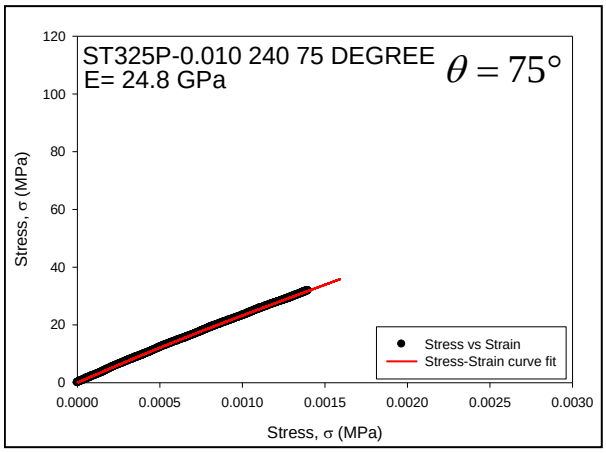

Figure 222. ST325P-0.010 240 75-Degree Elastic Modulus

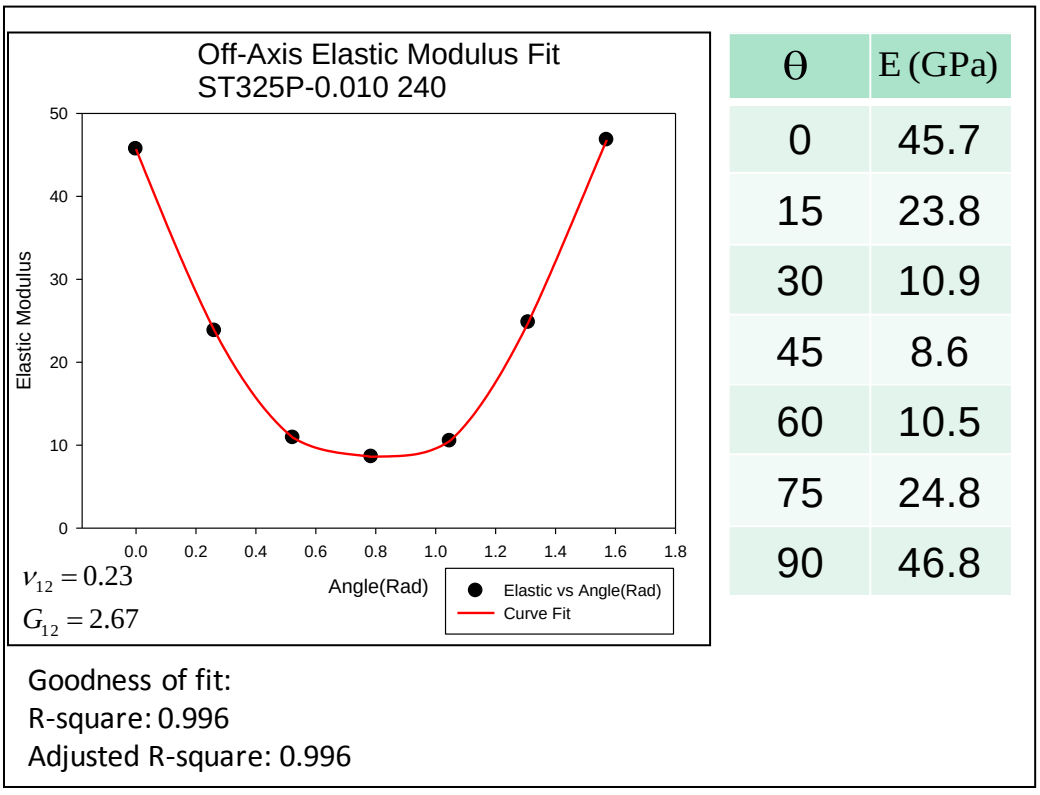

θ	E (GPa)
0	45.7
15	23.8
30	10.9
45	8.6
60	10.5
75	24.8
90	46.8

Figure 223. ST325P-0.010 240 Elastic Modulus versus Off-Axis Angle Curve Fitting Plot

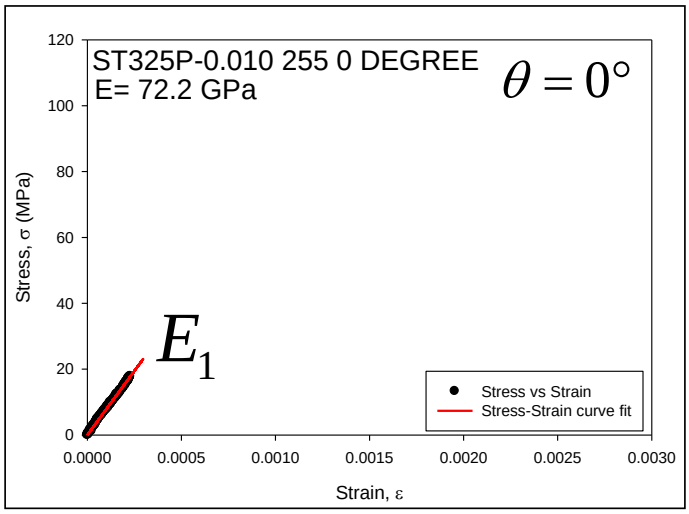

Figure 224. ST325P-0.010 255 0-Degree Elastic Modulus

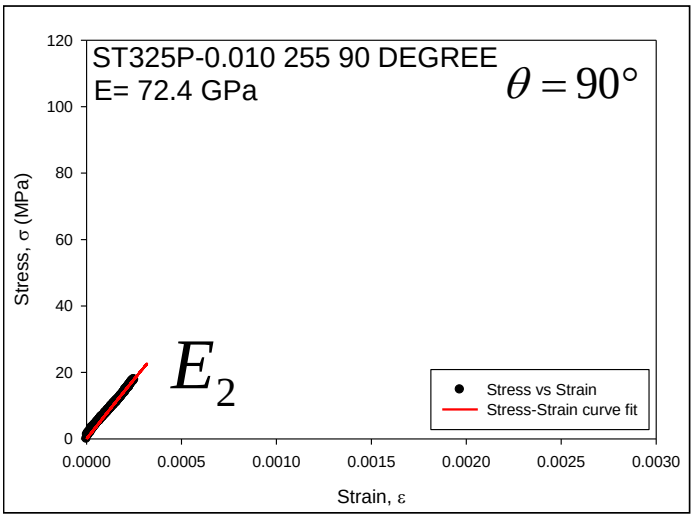

Figure 225. ST325P-0.010 255 90-Degree Elastic Modulus

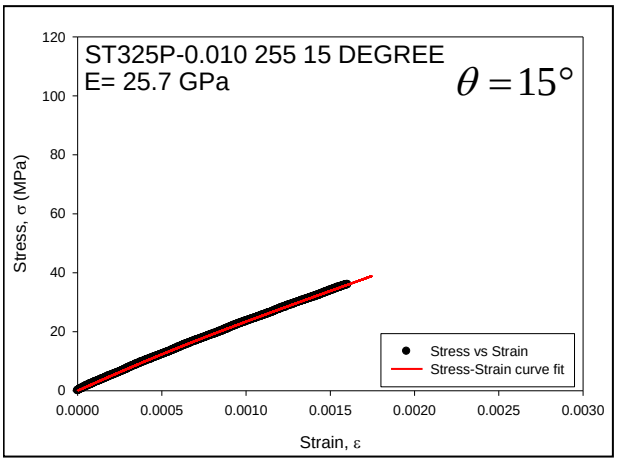

Figure 226. ST325P-0.010 255 15-Degree Elastic Modulus

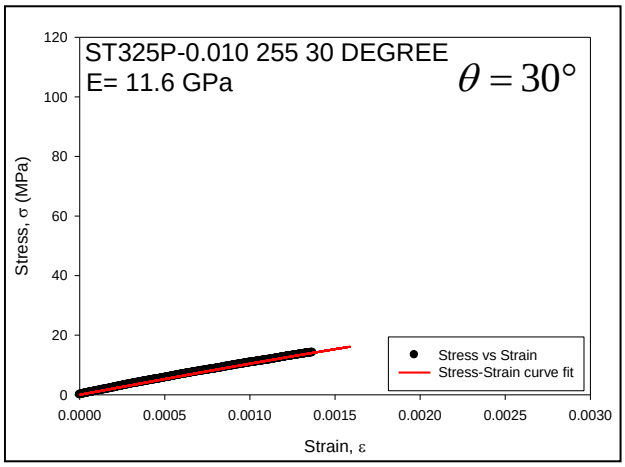

Figure 227. ST325P-0.010 255 30-Degree Elastic Modulus

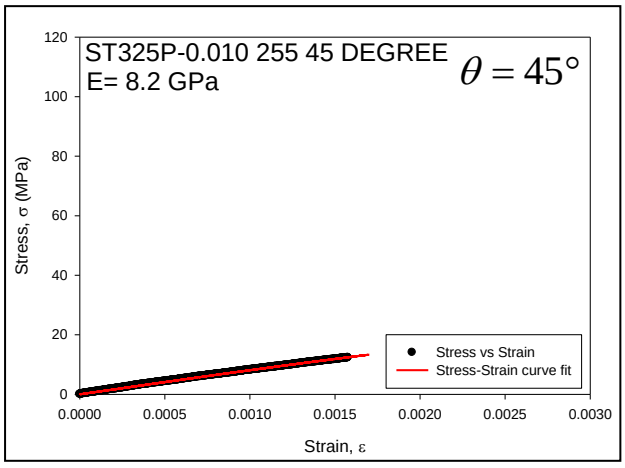

Figure 228. ST325P-0.010 255 45-Degree Elastic Modulus

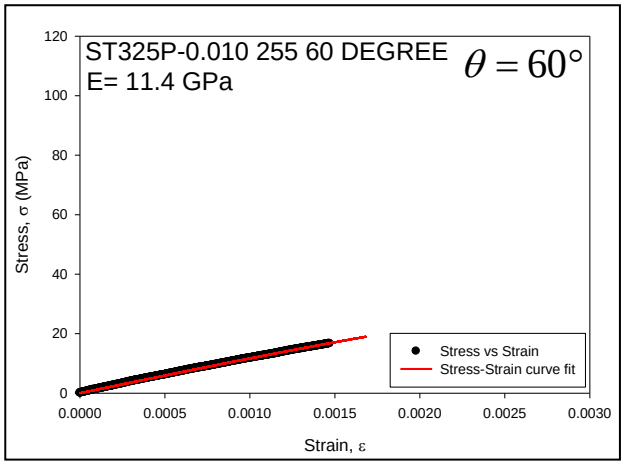

Figure 229. ST325P-0.010 255 60-Degree Elastic Modulus

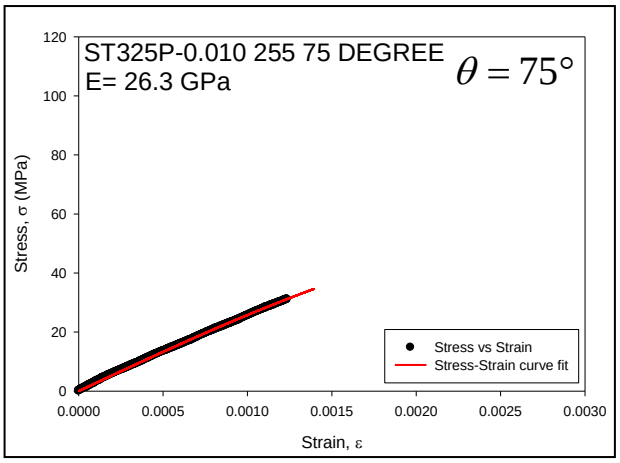

Figure 230. ST325P-0.010 255 75-Degree Elastic Modulus

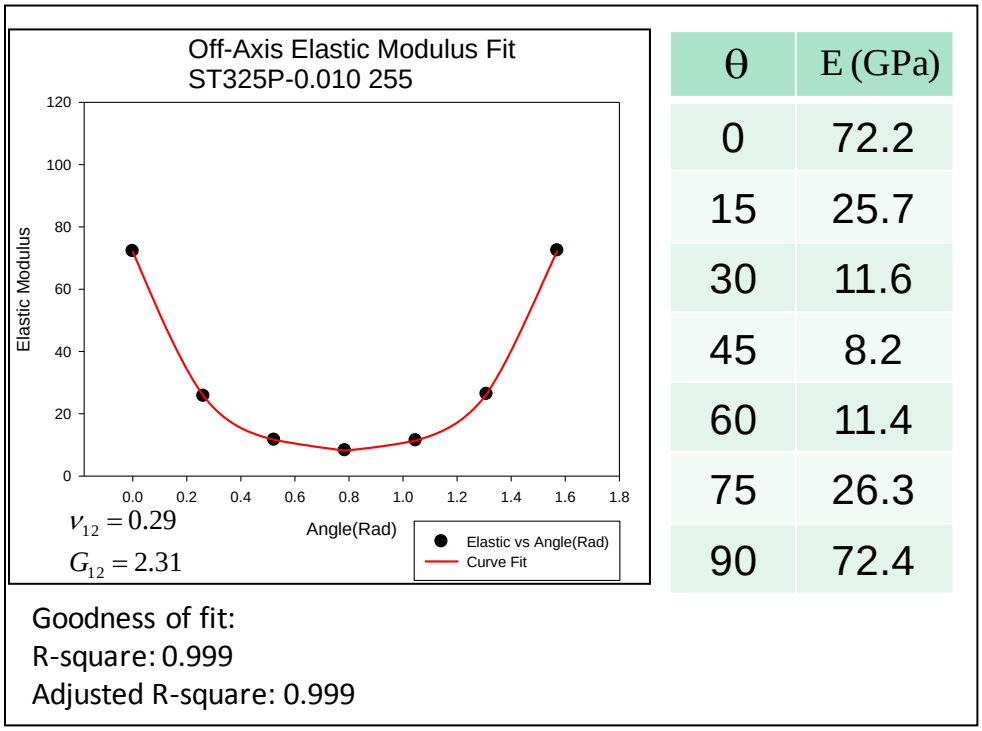

θ	E (GPa)
0	72.2
15	25.7
30	11.6
45	8.2
60	11.4
75	26.3
90	72.4

Figure 231. ST325P-0.010 255 Elastic Modulus versus Off-Axis Angle Curve Fitting Plot

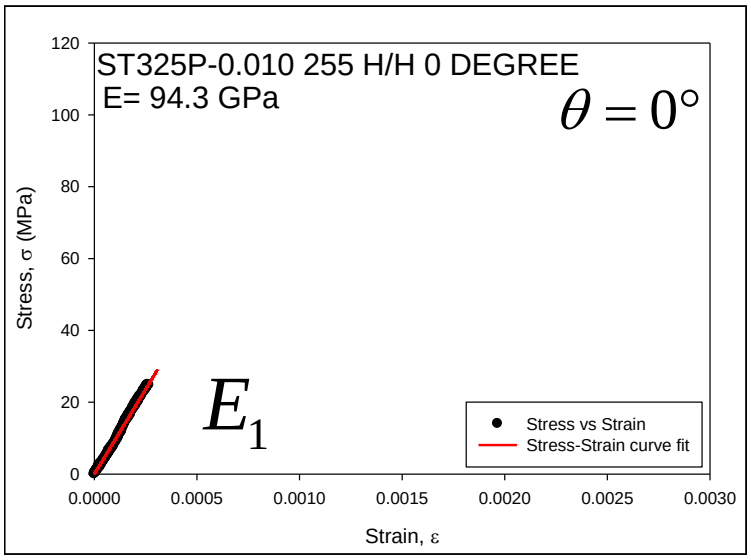

Figure 232. ST325P-0.010 255 H/H 0-Degree Elastic Modulus

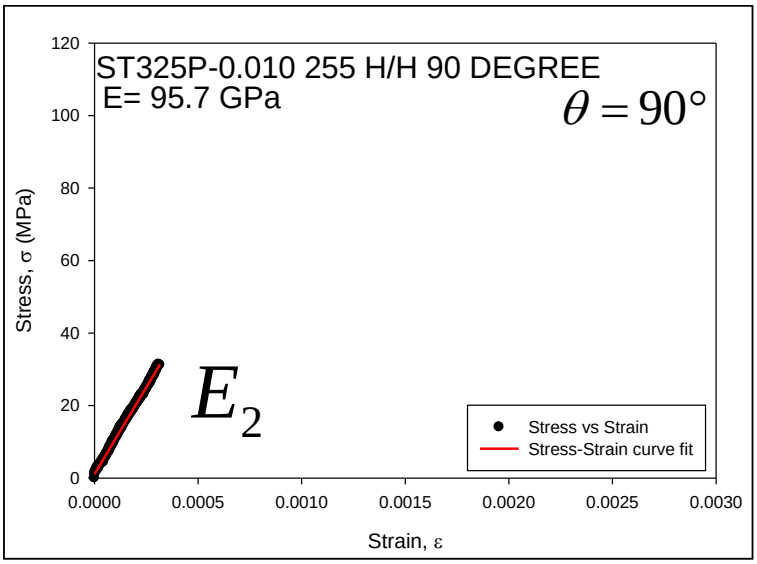

Figure 233. ST325P-0.010 255 H/H 90-Degree Elastic Modulus

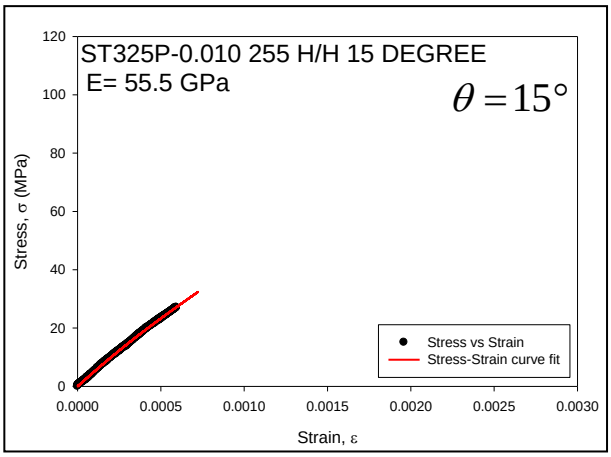

Figure 234. ST325P-0.010 255 H/H 15-Degree Elastic Modulus

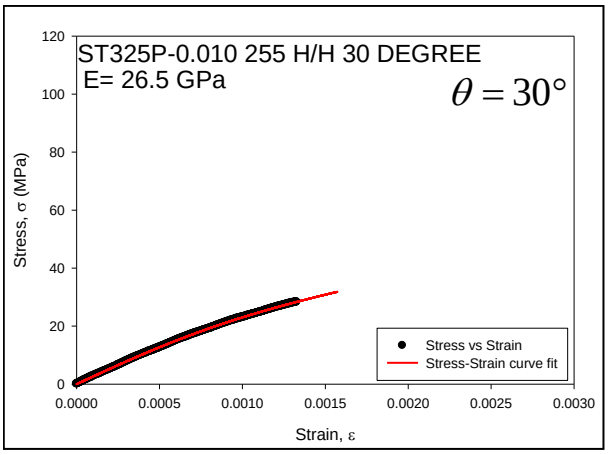

Figure 235. ST325P-0.010 255 H/H 30-Degree Elastic Modulus

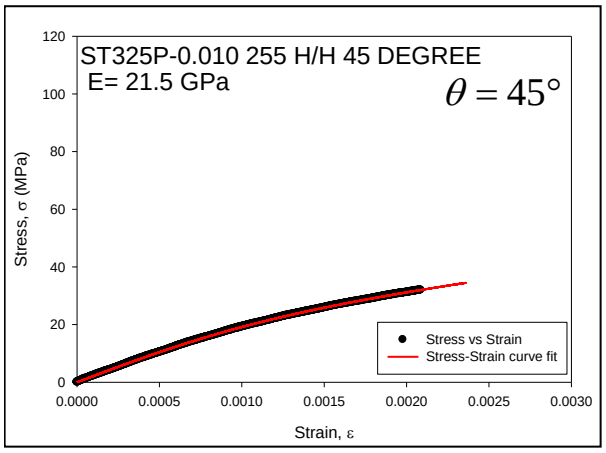

Figure 236. ST325P-0.010 255 H/H 45-Degree Elastic Modulus

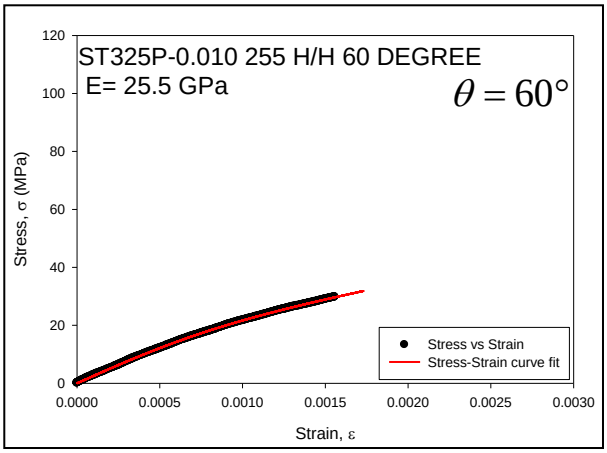

Figure 237. ST325P-0.010 255 H/H 60-Degree Elastic Modulus

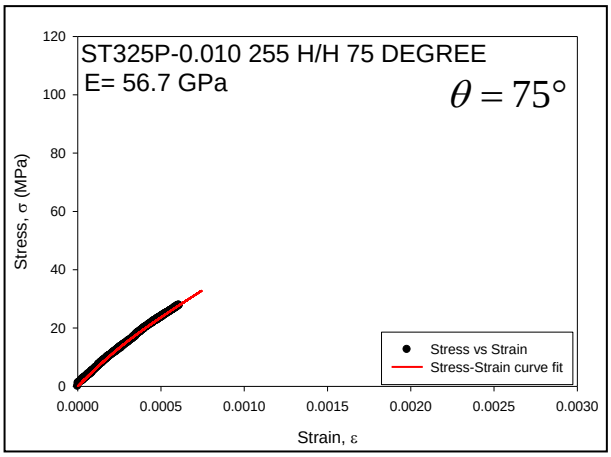

Figure 238. ST325P-0.010 255 H/H 75-Degree Elastic Modulus

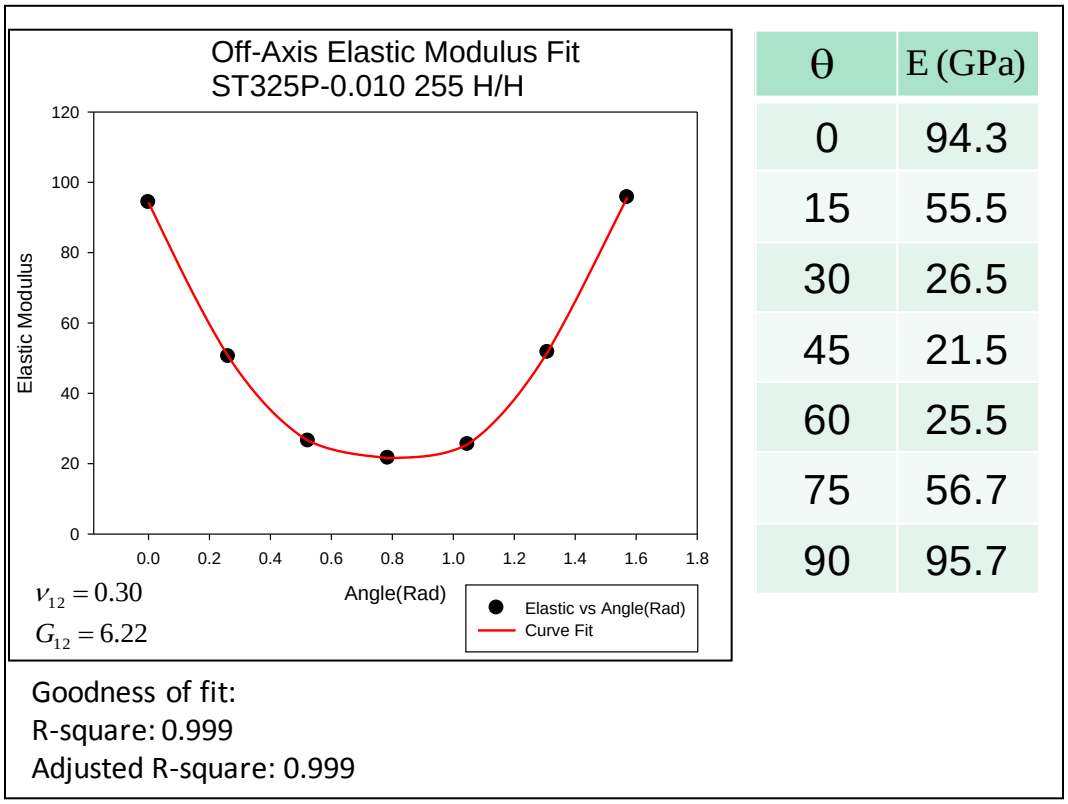

θ	E (GPa)
0	94.3
15	55.5
30	26.5
45	21.5
60	25.5
75	56.7
90	95.7

Figure 239. ST325P-0.010 255 H/H Elastic Modulus versus Off-Axis Angle Curve Fitting Plot

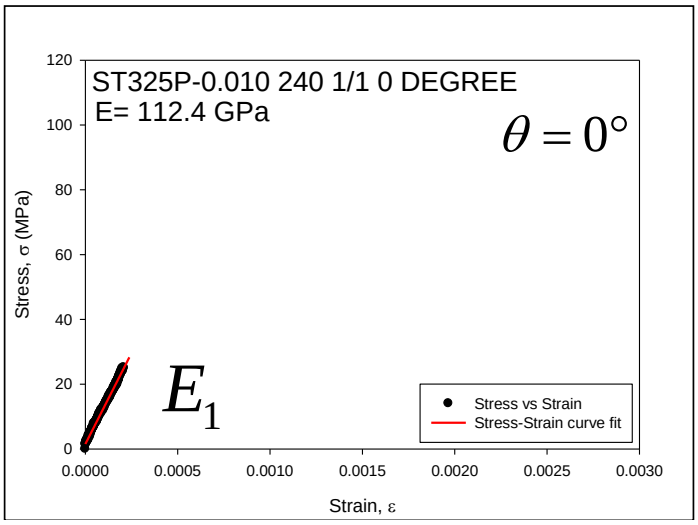

Figure 240. ST325P-0.010 240 1/1 0-Degree Elastic Modulus

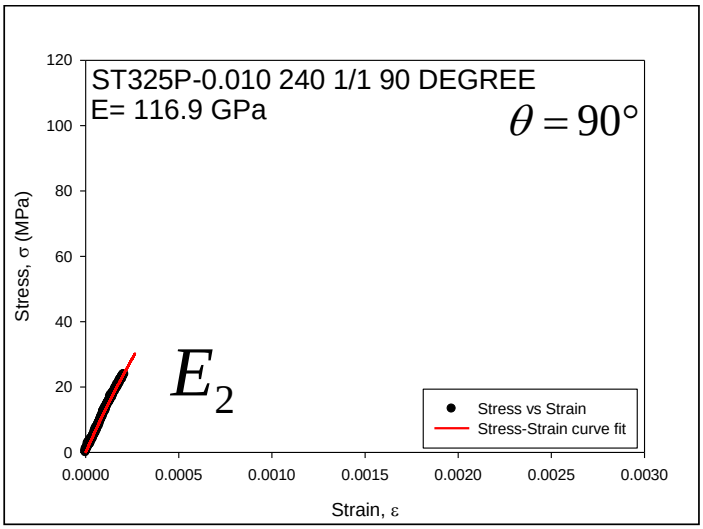

Figure 241. ST325P-0.010 240 1/1 90-Degree Elastic Modulus

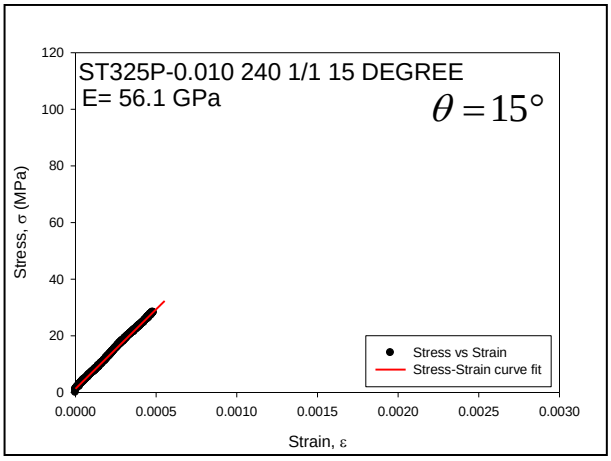

Figure 242. ST325P-0.010 240 1/1 15-Degree Elastic Modulus

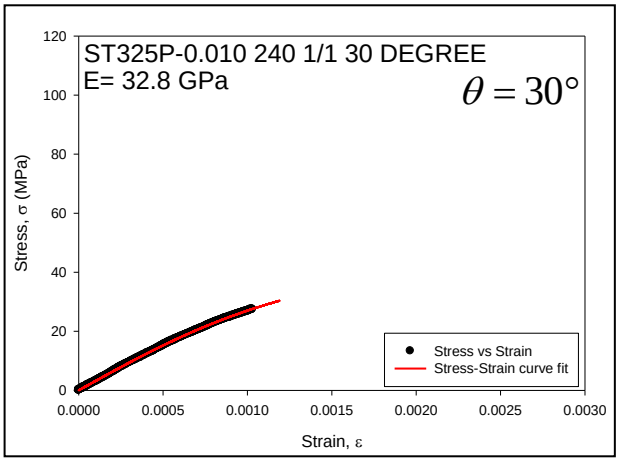

Figure 243. ST325P-0.010 240 1/1 30-Degree Elastic Modulus

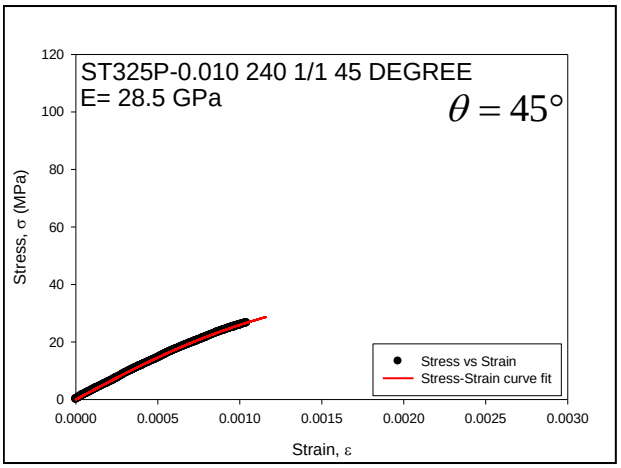

Figure 244. ST325P-0.010 240 1/1 45-Degree Elastic Modulus

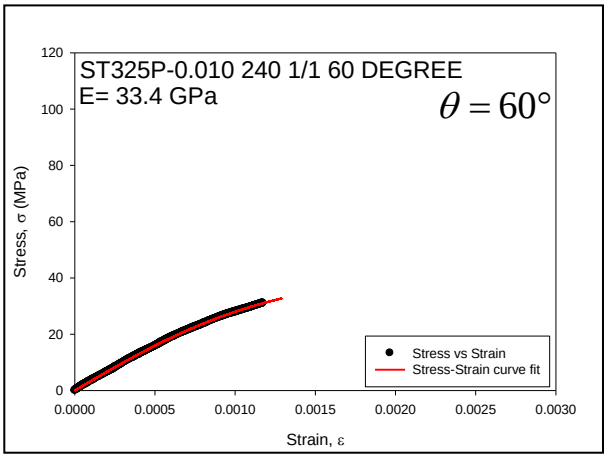

Figure 245. ST325P-0.010 240 1/1 60-Degree Elastic Modulus

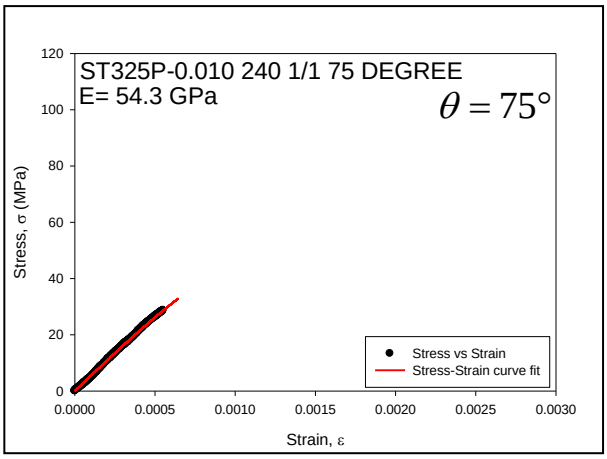

Figure 246. ST325P-0.010 240 1/1 75-Degree Elastic Modulus

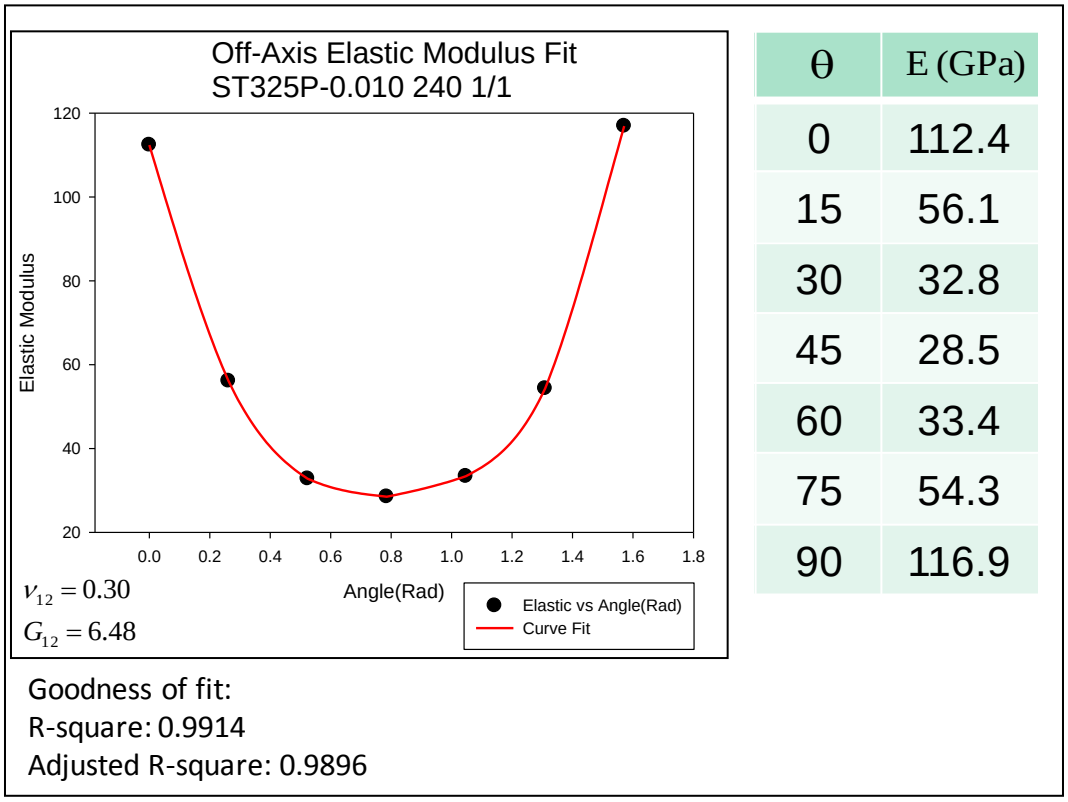

θ	E (GPa)
0	112.4
15	56.1
30	32.8
45	28.5
60	33.4
75	54.3
90	116.9

Figure 247. ST325P-0.010 240 1/1 Elastic Modulus versus Off-Axis Angle Curve Fitting Plot

APPENDIX B - MATLAB CODE

Matlab Code for Single-layer STABLCOR Model:

```
clear all; close all; clc;
%The program is able to calculate model construct with different numbers of
%layers.
%Enter E1 Elastic Moduli Grain Direction property for each layer(Top to Bottom)
E1=[12E9 77E9 12E9];
%Enter E2 Elastic Moduli perpendicular to Grain Direction property for each layer(Top to Bottom)
E2=[12E9 57.7E9 12E9];
%Enter G12 Shear Modulus property for each layer(Top to Bottom)
G12=[3.1E9 2.31E9 3.1E9];
%Enter v12 property for each layer(Top to Bottom)
V12=[0.27 0.29 0.27];
%Enter v21 property for each layer(Top to Bottom)
V21=[0.27 0.29 0.27];
%Enter Thickness property for each layer(Top to Bottom)
t=[0.1 0.0255 0.1];
%Alpha X, Alpha Y, Alpha XY
AL1=[12E-6 4.1E-6 12E-6];
AL2=[12E-6 6.04E-6 12E-6];
AL12=[0 0 0];
ALA=[AL1; AL2; AL12];
%Temperature (Delta T)
DT=25,
ALT=ALA*DT;
Q11=(E1./(1-(V12.*V21)));
Q22=(E2./(1-(V12.*V21)));
Q12=((V12.*E2)/(1-V12.*V21));
Q21=((V12.*E2)/(1-V12.*V21));
Q66=G12;
DD=0;
%Thermal Loads
for i= 1 : length(t);
Q=[Q11(:,i) Q12 0; Q12 Q22(:,i) 0; 0 0 Q66(:,i)];
D=Q*ALT(:,i)*t(:,i); %ALT
DD=DD+D;
end
A11=sum(Q11.*t);
A22=sum(Q22.*t);
A12=sum(Q12.*t);
A21=sum(Q21.*t);
A66=sum(Q66.*t);
AM=[A11 A12 0; A21 A22 0; 0 0 A66],
AI=inv(AM);
AI,
C=AI*DD;
D=C/DT;
Thermalstrain=C,
CTE=D,
```

Matlab Code For Tri-layer STABLCOR Model:

```
clear all; close all; clc;
%The program is able to calculate model construct with different numbers of
%layers.
%Enter E1 Elastic Moduli Grain Direction property for each layer(Top to Bottom)
E1=[12E9 77E9 12E9 77E9 12E9 77E9 12E9];
%Enter E2 Elastic Moduli perpendicular to Grain Direction property for each layer(Top to Bottom)
E2=[12E9 57.7E9 12E9 57.7E9 12E9 57.7E9 12E9];
%Enter G12 Shear Modulus property for each layer(Top to Bottom)
G12=[3.1E9 2.31E9 3.1E9 2.31E9 3.1E9 2.31E9 3.1E9];
%Enter v12 property for each layer(Top to Bottom)
V12=[0.27 0.29 0.27 0.29 0.27 0.29 0.27];
%Enter v21 property for each layer(Top to Bottom)
V21=[0.27 0.29 0.27 0.29 0.27 0.29 0.27];
%Enter Thickness property for each layer(Top to Bottom)
t=[0.1 0.0255 0.1 0.0255 0.1 0.0255 0.1];
%Alpha X, Alpha Y, Alpha XY
AL1=[12E-6 4.1E-6 12E-6 4.1E-6 12E-6 4.1E-6 12E-6];
AL2=[12E-6 6.04E-6 12E-6 6.04E-6 12E-6 6.04E-6 12E-6];
AL12=[0 0 0 0 0 0 0];
ALA=[AL1; AL2; AL12];
%Temperature (Delta T)
DT=25,
ALT=ALA*DT;
Q11=(E1./(1-(V12.*V21)));
Q22=(E2./(1-(V12.*V21)));
Q12=((V12.*E2)/(1-V12.*V21));
Q21=((V12.*E2)/(1-V12.*V21));
Q66=G12;
DD=0;
 %Thermal Loads
for i= 1 : length(t);
Q=[Q11(:,i) Q12 0; Q12 Q22(:,i) 0; 0 0 Q66(:,i)];
D=Q*ALT(:,i)*t(:,i); %ALT
DD=DD+D;
end
 A11=sum(Q11.*t);
A22=sum(Q22.*t);
A12=sum(Q12.*t);
A21=sum(Q21.*t);
A66=sum(Q66.*t);
 AM=[A11 A12 0; A21 A22 0; 0 0 A66],
AI=inv(AM);
AI,
C=AI*DD;
D=C/DT;
Thermalstrain=C,
CTE=D,
```